

CHARACTERIZATION OF THE MECHANICAL RESPONSE OF SILICON
CARBIDE FIBERS AND WAFERS WITH EMPHASIS ON BENDING

by

SHAWN HENRY WARD

A dissertation submitted to the

School of Graduate Studies

Rutgers, The State University of New Jersey

In partial fulfillment of the requirements

For the degree of

Doctor of Philosophy

Graduate Program in Materials Science and Engineering

written under the direction of

Adrian B. Mann

And approved by

New Brunswick, New Jersey

October, 2018

ABSTRACT OF THE DISSERTATION

Characterization of the mechanical response of silicon carbide fibers and wafers with

emphasis on bending

By SHAWN H WARD

Dissertation Advisors:

Adrian B. Mann and M. John Matthewson

Bending – the basis of the bow and arrow, leaf springs, and one of the most common modes of failure – has been studied for hundreds of years. This thesis brought mechanical characterization of micron-scale fibers and observation of the change in position of Raman peaks with stress together under the umbrella of bending. Both utilized bending to a large degree – one to determine its mechanical properties and the other to examine in-situ behavior of ceramics under stress.

Silicon carbide fibers were grown by Free Form Fibers LLC through a unique method called laser-induced CVD. This method is capable of growing fully dense fibers 30-60 microns in diameter and meters long. Characterization methods included

nanoindentation, helium-ion microscopy, Raman spectroscopy, and the development of a new large-deflection cantilever bend testing technique. The fibers consist of an inner core of crystalline SiC and an outer layer of amorphous carbon-rich silicon. Nanoindentation of the outside of the fibers and over the cross-section show that the outer layer has a reduced elastic modulus of 160 GPa and a hardness of 18 GPa, while the inner core has a reduced elastic modulus of 330 GPa and a hardness of 36 GPa. Large-deflection cantilever bend testing showed that the elastic modulus can vary between batches and that the overall elastic modulus of the fibers is 300 GPa. Fractography using the helium-ion microscope indicates that the fibers failed at ~ 2.2 GPa. These values are consistent with those obtained for third generation commercially available fibers.

Raman spectra, arising from chemical bonds, are dependent on stress in solid materials. If a material is stretched, some bonds will stretch, and if a material is compressed the bonds will likewise compress, affecting the location of different Raman peaks. This concept was applied to determine experimentally what the relation between peak shift and stress was for several materials. This was done by designing, building, and validating a four-point bend apparatus for in-situ micro-Raman testing. Single crystal silicon was used as a control material to validate the machine and the relation obtained as $C=0.0022 \text{ cm}^{-1}/\text{MPa}$, the expected value for this coefficient. Silicon carbide, quartz, YAG, and two types of feldspar were tested and all were observed to have multiple peaks shift with stress.

Acknowledgements

There are many people who helped me transform from a simple mechanical engineer into a real scientist, first and foremost among them being my advisor, Professor Mann. His guidance (and especially edits) helped make me a better researcher and communicator. I also would like to thank Professor Matthewson as my co-advisor and Professor Birnie for stepping in at the last moment. Just as critically, I would like to thank Dr. Harrison for not only being there when my PhD was in danger of becoming a Master's, but also for his enthusiasm and assistance throughout this work.

I am extremely grateful for the support provided by Dr. Harrison, Free Form Fibers, LLC, and the NSF-funded Ceramics, Composites, and Optical Materials Center for funding my work after my first two years, without which this would not be a PhD.

To my friends and fellow graduate students: thank you. You made my time here so much more enjoyable than it could have been. I would especially like to thank Ross and Bera for making the time here fun, and Sean, Riyanka, and Craig for being excellent trampolines for my ideas.

Thank you to the secretaries of the department – Nahed, Michelle, and Sheela. Without you I never would have figured any of the bureaucracy out. Y'all are awesome.

Rachel, how do I even start to thank you for being there? You tolerated my exasperated monologues and the rarer but happier "things went right!" monologues without understanding a word; you kept me from going crazy from working and gave me space when it was needed; you're amazing and I love you.

To my family, thank you for putting up with me moving 2,100+ miles for the sake of science. I have a greater appreciation of home and you.

PREFACE

This thesis is partially based on the following papers:

1. Mechanical characterization of silicon carbide fibers grown by laser-induced CVD. S.H. Ward, A.B. Mann, S. Harrison; In review: Journal of the American Ceramic Society
2. Four-point bend apparatus for *in situ* micro-Raman stress. S.H. Ward and A.B. Mann; Measurement Science and Technology 29 (2018) 065903
3. Investigation of the uniaxial relation of stress and Raman peak shifts and the application thereof in single crystal YAG fibers. S.H. Ward, S. Bera, A.B. Mann, J.A. Harrington; manuscript in preparation

The relevant chapters of this thesis contain these papers as submitted and accepted, along with additional results and discussion where necessary.

Table of Contents

ABSTRACT OF THE DISSERTATION	II
ACKNOWLEDGEMENTS	IV
PREFACE	V
TABLE OF CONTENTS	VI
LIST OF TABLES	IX
LIST OF FIGURES	XI
1 INTRODUCTION	1
2 BACKGROUND	3
2.1 CERAMIC MATRIX COMPOSITES	3
2.2 SILICON CARBIDE FIBERS FOR CMCs	4
2.2.1 EXISTING FIBERS AND PROCESSES	5
2.2.2 FFF SiC FIBERS	6
2.3 MECHANICAL TEST METHODS.....	8
2.3.1 TENSILE TESTING.....	8
2.3.2 BENDING	10
2.3.3 NANOINDENTATION	13
2.4 RAMAN	17
2.4.1 THEORY	17
2.4.2 RAMAN FOR STRESS INVESTIGATIONS	21
2.5 MATERIALS	24
2.5.1 SILICON	24
2.5.2 SILICON CARBIDE.....	26

2.5.3 YAG	31
2.5.4 FELDSPAR.....	35
2.5.5 QUARTZ	37
2.6 HELIUM ION MICROSCOPY	40
2.7 FRACTOGRAPHY	41
3 EXPERIMENTAL PROCEDURES	45
3.1 NANOINDENTATION	45
3.2 CANTILEVER BENDING	48
3.3 RAMAN	50
3.4 FRACTOGRAPHY	52
4 MECHANICAL CHARACTERIZATION OF SILICON CARBIDE FIBERS GROWN BY LASER- INDUCED CVD	53
5 SUPPORTING WORK IN CHARACTERIZATION OF SAID SiC FIBERS	77
5.1 FRACTOGRAPHY	77
5.2 RAMAN SPECTROSCOPY.....	89
6 FOUR-POINT BEND APPARATUS FOR <i>IN SITU</i> MICRO-RAMAN STRESS MEASUREMENTS	94
7 INVESTIGATION OF THE UNIAXIAL RELATION OF STRESS AND RAMAN PEAK SHIFTS AND THE APPLICATION THEREOF IN SINGLE CRYSTAL YAG FIBERS	115
8 FELDSPAR AND QUARTZ.....	126
8.1 FELDSPAR.....	126
8.2 QUARTZ	137
9 CONCLUSIONS	145
10 BROADER IMPLICATIONS AND FUTURE WORK.....	149

APPENDIX 1 – MATLAB CODE, EQUATION 8	156
REFERENCES.....	157

List of tables

Table 2.1: Basic data about selected commercial SiC fibers	5
Table 2.2: Selected mechanical properties of silicon.....	25
Table 2.3: Raman peak position of three polytypes of silicon carbide	29
Table 2.4: Selected mechanical properties of silicon carbide.....	30
Table 2.5: Raman peak positions in YAG	33
Table 2.6: Selected mechanical properties of YAG.....	34
Table 2.7: Selected mechanical properties of feldspar	35
Table 2.8: Selected mechanical properties of α -quartz.....	38
Table 2.9: Raman peak positions in α -quartz	39
Table 5.1: Analysis of mirrors on the fracture surfaces of SiC fibers	84
Table 6.1: The proportionality coefficient 'C' for silicon and silicon carbide.	97
Table 6.2: Comparison of proportionality coefficients of SiC	111
Table 7.1: Hydrostatic C of various peaks in YAG	116
Table 7.2: Experimentally determined C of selected peaks in YAG	119
Table 8.1: Hydrostatic C of the 480cm^{-1} and 290cm^{-1} peaks in albite and labradorite...	130
Table 8.2: Experimental C for various peaks in albite sample 1	132
Table 8.3: Experimental C for various peaks in albite sample 2	133

Table 8.4: Hydrostatic C of various peaks in α -quartz	138
Table 8.5: Orientation of quartz samples in experimental set-up	140
Table 8.6: Experimental C for various peaks and orientations in quartz.....	141

List of Figures

Figure 2.1: Schematic of the process used by Free Form Fibers LLC	7
Figure 2.2: Fiber Laser Printer™ concept by Free Form Fibers.....	7
Figure 2.3: Typical stress-strain cruves of brittle and typical ductile materials	9
Figure 2.4: Schematic of a static tensile test.....	9
Figure 2.5: Schematic of a three-point bend test	10
Figure 2.6: Schematic of a four-point bend test.....	11
Figure 2.7: Diagram of a clamped-free cantilever beam	12
Figure 2.8: Typical load-depth curve obtained via nanoindentation	14
Figure 2.9: Surface profile under the indenter tip during and after indentation	15
Figure 2.10: Energy change between Stokes, Rayleigh, and anti-Stokes scattering	19
Figure 2.11: Diagram of two-particle proximity vs bond energy	22
Figure 2.12: Typical Raman spectrum of single crystal silicon.....	26
Figure 2.13: Schematic of the Acheson process	27
Figure 2.14: Stacking order of the planes in four different silicon carbide polytypes.....	28
Figure 2.15: Typical Raman spectra of 3C-, 4H-, and 6H-SiC.....	29
Figure 2.16: Raman spectra of amorphous SiC at different stoichiometries	30
Figure 2.17: Schematic of the growth process of YAG single crystals via LHPG.....	31
Figure 2.18: Unit cell and chemistry of YAG.....	32
Figure 2.19: Example Raman spectrum of YAG using a 514 nm laser.....	33
Figure 2.20: Unit cell of feldspar	36
Figure 2.21: Typical Raman spectrum of albite.....	37
Figure 2.22: Typical Raman spectrum of labradorite.	37

Figure 2.23: Typical Raman spectrum of quartz	39
Figure 2.24: Schematic of helium-ion microscope beam column	41
Figure 2.25: Directions that stress intensity factors K_I , K_{II} , and K_{III} apply	43
Figure 3.1: Image of the Triboindenter™ outside components.....	46
Figure 3.2: Typical load-time load function used in this work.....	47
Figure 3.3: Typical load-depth curve for fused silica	48
Figure 3.4: Fiber set up as a clamped cantilever beam	49
Figure 3.5: Fiber exhibiting large deflection in large-deflection cantilever test.....	50
Figure 3.6: Fitting peaks to a Raman spectrum in Wire 4.2 software.	51
Figure 4.1: Single fiber adhered to a steel puck.....	57
Figure 4.2: Different upright mounting methods	58
Figure 4.3: Fiber mounted for cantilever testing	60
Figure 4.4: Fiber during large-deflection cantilever test	61
Figure 4.5: Data from nanoindents done on the outside surface of the fibers	64
Figure 4.6: Helium-ion image of a nanoindent on the outside of a fiber.....	65
Figure 4.7: Schematic of issues with early upright mounting methods of fibers	66
Figure 4.8: HIM image of the cross-section of a fiber mounted in sintered glass.....	67
Figure 4.9: Maps of the reduced modulus and hardness of the cross-section of a fiber ...	68
Figure 4.10: Fitting the large-deflection model to real data	70
Figure 4.11: Elastic modulus vs beam length of cantilever fibers.....	71

Figure 5.1: Fiber broken in bending showing mirror-mist-hackle features	78
Figure 5.2: Mirror-mist-hackle on a different fiber	79
Figure 5.3: Fiber broken in bending that shows cantilever curl	80
Figure 5.4: Secondary fracture surface	81
Figure 5.5: Secondary fracture surface on a different fiber	82
Figure 5.6: Surface cracks near primary fracture face	86
Figure 5.7: Observable change in fracture surface near cantilever curl	88
Figure 5.8: Raman spectra taken on the outside of a fiber with the 514 nm laser	90
Figure 5.9: Raman spectra taken on the outside of a fiber with the 633 nm laser	90
Figure 5.10: Raman spectra taken on the outside of a fiber with the 785 nm laser	91
Figure 5.11: Raman spectra over the cross-section of a fiber with the 633 nm laser	92
Figure 5.12: Raman spectra over the cross-section of a fiber with the 785 nm laser	92
Figure 5.13: Raman spectrum showing SiC peaks in the center of the fiber	93
Figure 6.1: Coordinate system of the developed four-point bend set-up	100
Figure 6.2: Schematic of the developed machine	101
Figure 6.3: Image of the device in-situ to the Raman microscope	101
Figure 6.4: Linear fit of the data obtained for silicon	107
Figure 6.5: Example of 4H-SiC Raman spectrum	108
Figure 6.6: Linear fit of data obtained for the 798 cm^{-1} SiC Raman peak	110
Figure 6.7: Comparison of the linear fits of two peaks in silicon carbide	110
Figure 7.1: Example Raman spectrum of YAG taken with the 514 nm laser	118

Figure 7.2: Linear relation between stress and peak shift of the 782 cm^{-1} peak.....	119
Figure 7.3: 3 mm long line map of stress on a grown YAG fiber	121
Figure 7.4: $50\text{ }\mu\text{m}$ long line map of stress on a grown YAG fiber	121
Figure 7.5: 1 mm long line map of stress on a grown YAG fiber	122
Figure 7.6: $50\text{ }\mu\text{m}$ long line map of stress on a grown YAG fiber	122
Figure 7.7: 1mm long line map of stress on a grown Nd:YAG fiber	123
Figure 7.8: 0.5 mm long line map of stress on a grown Nd:YAG fiber	123
Figure 8.1: Image of cut and polished albite and labradorite samples.....	127
Figure 8.2: Raman mode assignment for selected vibrations of atoms in albite	129
Figure 8.3: Example linear relation of the 480cm^{-1} and 510cm^{-1} peaks in labradorite...	131
Figure 8.4: Behavior of the 146 cm^{-1} peak in albite	133
Figure 8.5: Example of poor quality data	134
Figure 8.6: Behavior of the 480cm^{-1} peak in albite	135
Figure 8.7: Direction of compressibility of albite unit cell.....	136
Figure 8.8: Behavior of the 578cm^{-1} peak under hydrostatic stress.....	137
Figure 8.9: Behavior of Raman peaks of quartz under hydrostatic stress	139
Figure 8.10: Orientation of ST-cut α -quartz for this project.....	139
Figure 8.11: Orientation of samples of quartz for this project.....	140
Figure 8.12: Linera fit of the 206cm^{-1} peak in quartz	142
Figure 8.13: Linear fits of the 128cm^{-1} peak in quartz for different orientations	143

1 Introduction

This project consisted of two parts united by their mechanical test methods. The first project sought to characterize the mechanical properties of silicon carbide fibers grown by laser-induced chemical vapor deposition. A number of methods were utilized to achieve this goal, including cantilever bending, instrumented indentation (nanoindentation), helium-ion microscopy, and Raman spectroscopy. These fibers warranted such extensive testing due to their novel mode of manufacture [1] and their potential applications for high-temperature, high-stress environments, such as in nuclear fuel reactors and turbine engines [2] [3]. The methods listed were chosen for several reasons; one of the largest being that bending and nanoindentation can both be used to determine the elastic modulus of a material, independently confirming each other. Bending provides a global view of the mechanical properties of the fibers, while nanoindentation can provide very local data on both the elastic modulus and the hardness. Helium-ion microscopy was used to observe surface and fracture morphologies, the latter being related to the stress in the fiber at the time and point of fracture. Raman spectroscopy was chosen for its good spatial resolution and ability to tell chemistry, order and disorder, and phase changes apart.

The second project sought to build, validate, and use a four-point bend device for in-situ micro-Raman measurements. Four-point bending was chosen due to its ability to apply a pure bending moment throughout the center of a beam, negating factors that might affect the behavior of the material, such as a pin in the center of a three-point bending apparatus. By placing a sample in the jaws of the device and applying a force, all while

under the Raman microscope, maps may be taken across the surface of the sample that take spectra on both the tensile and compressive sides. Doing so, one can observe how individual peak positions move with stress. This movement of stress can be recorded and used as a calibration line to determine stress in manufactured materials [4] [5] [6]. This can be done for any number of materials, starting with simple semiconductors such as silicon and then being applied to silicon carbide, quartz, feldspars, and YAG, each material important in its own right.

2 Background

This section provides some of the existing knowledge which was utilized to conduct the research for this thesis. As such, it encompasses prior work in the field of ceramic matrix composites, non-oxide fibers with a focus on silicon carbide, selected mechanical testing methods for strong materials, spectroscopic and analysis techniques used, and an overview of the properties of the materials investigated.

2.1 Ceramic matrix composites

Ceramic matrix composites (CMCs) are any combination of matrix and filler in which both are a ceramic; the filler may be fibers, plates, or particles and randomly or selectively oriented. The matrix and filler do not need to be different ceramics, nor do they need to be the same ceramic. They have the advantage over metals of being much lower density (3.1g/cc for silicon carbide vs 7.5g/cc for steel [7] [8]) and capable of withstanding higher temperatures. The primary reason pure ceramics are not widely used in applications is that they are brittle and fail without warning. Use of a composite allows for practical application of ceramics as they have a higher fracture toughness than pure ceramics [9]. Reinforcement via a secondary ceramic (typically a fiber) can increase the fracture toughness by a variety of means, often by increasing the crack tortuosity [10] [11]. It is important that the reinforcing material not crack in the same plane as the primary fracture – if the bond between the matrix and filler is stronger than the filler a crack will pass through without expending energy going around the filler [10]. Because of this, the filler must be at least as strong as the matrix, in addition to not causing undue stresses from processing.

Ceramic matrix composites are most widely used or in consideration for use in high-temperature or radiological applications, such as turbine engine blades [12] and nuclear fuel reactors [12] [9]. These and other applications may be in extreme corrosive or oxidizing environments [12]; conventional and high-tech metals either cannot withstand such conditions or are prohibitively difficult and expensive to make. Various ceramics are used for such applications instead, due to their ability to resist oxidation [12], low density (and thus mass for the same part), and high strength. These ceramics include but are not limited to silicon nitride, boron nitride, boron carbide, sapphire and alumina, titanium carbide, carbon fibers, and silicon carbide [9] [12] [13] [14] [15] [16] [17] [18]. Of these, silicon carbide (SiC) exhibits innate resistance to neutron irradiation due to the low atomic numbers of both components [19] [20].

The process of CVI, chemical vapor infiltration, utilizes pre-made fibers that are surrounded with a polymer precursor which is then infiltrated with vapor phase silane [21] [3]. This is the most common process in use, other processes including liquid silicon infiltration [22] and polymer-impregnation and pyrolysis [23]. CVI is a proven method, being used by multiple companies to produce a CMC [9] [24].

2.2 Silicon carbide fibers for CMCs

Silicon carbide is a common and well-studied fiber found in CMCs [2] [3] [9] and as mentioned above, exhibits innate resistance to neutron irradiation, making it attractive for

nuclear applications. Further, it is non-reactive with molten salts [20] [25], an important aspect as some nuclear reactors utilize molten salt for heat transfer [26] [27].

2.2.1 Existing fibers and processes

There are a number of commercially available SiC fibers, each with a different stoichiometry, process, and in some cases, physical structure, all affecting the mechanical properties of the fibers. A comparison of various fibers, how they are made, and selected properties is given in Table 2.1.

Table 2.1: Selected fibers with the company that manufactured them, the base manufacturing process, elastic modulus, and hardness are given. The Tyranno SA had been tested before and after irradiation in [28] and both values are provided.

Fiber	Manufacturer	Process	Elastic modulus [GPa]	Hardness [GPa]
Nicalon	Nippon Carbon	PCS	220 [18] [29]	
Hi Nicalon	Nippon Carbon	PCS	187 [18]	23 [30]
Hi Nicalon S	Nippon Carbon	PCS	270 [18] [29]	
Tyranno Lox M	Ube Ind.	PCS	206 [18]	
Tyranno TE	Ube Ind.	PCS	420 [18]	
Tyranno SA	Ube Ind.	PCS	380 [18] [29]	15/25 [28] (non-/irradiated)
Sylramic	COI Ceramics	PCS	400 [29]	
SCS-6	Textron	C-core	350 [31]	35 [31]

The process labeled PCS is the most common process used to make SiC fibers currently. A polycarbosilane (PCS) polymer is spun-melted into fiber close to the desired diameter [32] [33]; the resulting fibers are then cured through pyrolysis and/or electron beam irradiation [32]. SCS-6 fibers, on the other hand, are produced by coating a carbon core (C-core) with silicon carbide in the gas phase [34]. In certain cases, the carbon core may be substituted for a titanium core.

2.2.2 FFF SiC fibers

Free Form Fibers, LLC developed and patented a novel method of producing SiC fibers: laser-induced chemical vapor deposition (LCVD) [35]. In this process, precursor gases are introduced to a chamber; a laser is shown through a window in the chamber and focused on either an amorphous carbon plate (if no fibers have been grown yet) or on the tip of an existing fiber. The heat of the laser at its focal point causes the precursor gases to break down and undergo a gas phase reaction that forms a solid at the focal point of the laser. As the fiber grows it may be pulled back at the same rate as the growth rate, allowing for continuous growth. Figure 2.1 provides a schematic of this process. This can be performed with any material that can be made via conventional CVD, the gases for SiC being silane and ethylene [1].

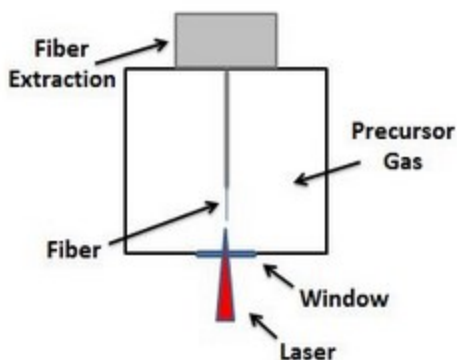


Figure 2.1: A schematic of the process used by Free Form Fibers LLC. Image from [1].

This process may be expanded by splitting the laser into multiple parallel beams, allowing for the growth of multiple fibers at the same time, the Fiber Laser Printer™ process (Figure 2.2):

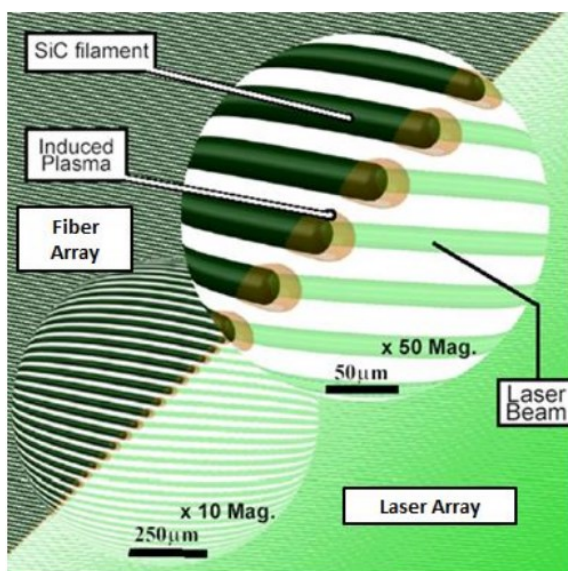


Figure 2.2: The Fiber Laser Printer™ concept by Free Form Fibers utilizes an array of lasers to grow multiple fibers at the same time and of the same composition. Image from [1].

Fibers grown via this method by Free Form Fibers were characterized in this work as part of a National Science Foundation grant to the Ceramics, Composites, and Optical Materials Center (CCOMC) of Rutgers and Clemson Universities.

2.3 Mechanical test methods

No one mechanical test method can determine all the mechanical characteristics of a material; due to this, a great variety of mechanical test methods exist to test the different properties of materials. Several can determine the same property, allowing for more variation in material size and shape as well as validating each other. Some tests provide the elastic modulus, yield point, and/or ultimate tensile strength of a material; other tests may provide hardness or resistance to impact, while yet more may obtain the same properties in a different manner. Mechanical tests of interest to this work are described below.

2.3.1 Tensile testing

One of the most common tests for obtaining the elastic modulus and ultimate tensile strength (and yield point, if applicable) of a material is the tensile test. A dog bone shaped test specimen is placed in the two jaws of the test machine and the jaws are slowly moved apart, typically at a fixed speed. As the jaws move, the load, time, and position of the moving jaw are recorded. This information allows a stress-strain curve to be developed; for most ceramics and metals, the initial slope up to the breaking point or yield point (whichever is first) is representative of the Young's modulus of the material (Figure 2.3)

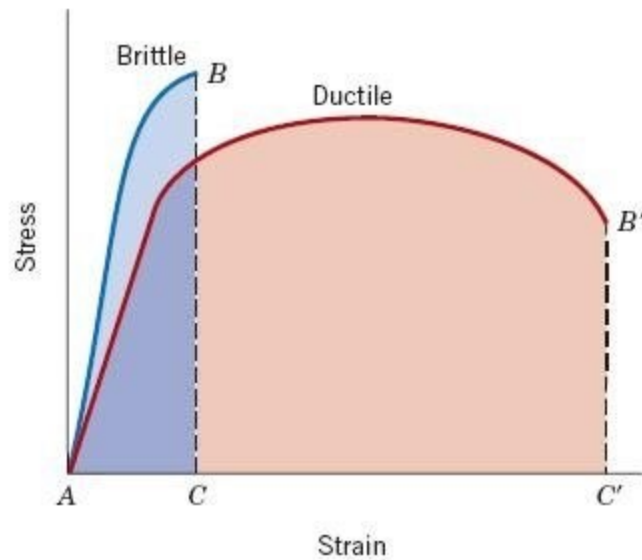


Figure 2.3: The blue curve represents a typical brittle material while the red curve represents a typical ductile material. The slope of the linear portion at the beginning of the curve is the elastic modulus. Image from [36].

The above describes a dynamic tensile test; another type of tensile test is the static tensile test. This is done by firmly fixing a length of material to a bar and attaching a weight to the end of it (Figure 2.4). This has the potential to give the ultimate strength of the material if a dynamic tensile test machine is not available.

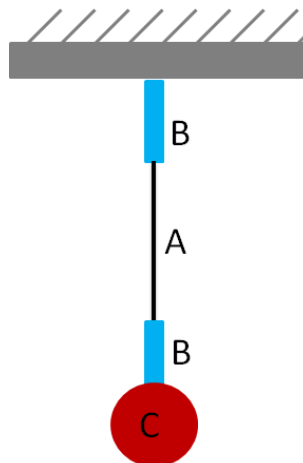


Figure 2.4: A black test specimen (A) is attached to two large strings or plates (B), and a mass (C) attached to the end provides a tensile force on the specimen. The stress on the test specimen is easily calculated from its geometry and the mass attached at the bottom.

2.3.2 Bending

Bending is traditionally used to determine the modulus of rupture of a material. The modulus of rupture (also known as the flexural strength) is calculated as

$$MoR [GPa] = \frac{Mc}{I} \quad (2.1)$$

where M is the moment the beam is under, c is the distance from the neutral axis to the outside of the beam, and I is the moment of inertia of the beam.

2.3.2.1 Three-point bending

Three-point bending is a method used to evaluate the modulus of rupture. Figure 2.5 provides a diagram of how it works.

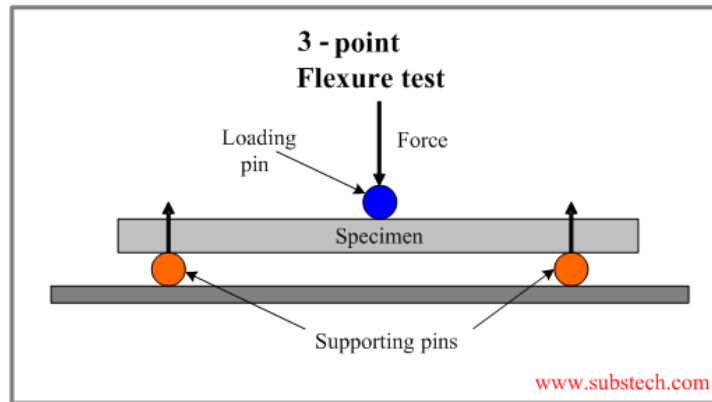


Figure 2.5: A beam undergoing a 3-point bend test is shown. The center wedge is located at half the distance between the supporting wedges and presses down at a constant rate. Image from [37].

The moment M is at a maximum right under the center wedge while the shear stress is at zero at the same location. For a centrally loaded beam, M is calculated as

$$M = \frac{L}{2} \cdot F \quad (2.2)$$

L is the length of the span between supporting pins and F is the applied force.

2.3.2.2 Four-point bending

Four-point bending is similar to three-point bending, but the volume of material under pure bending is larger and less susceptible to off-center loading effects. Figure 2.6 provides a schematic of this mechanism.

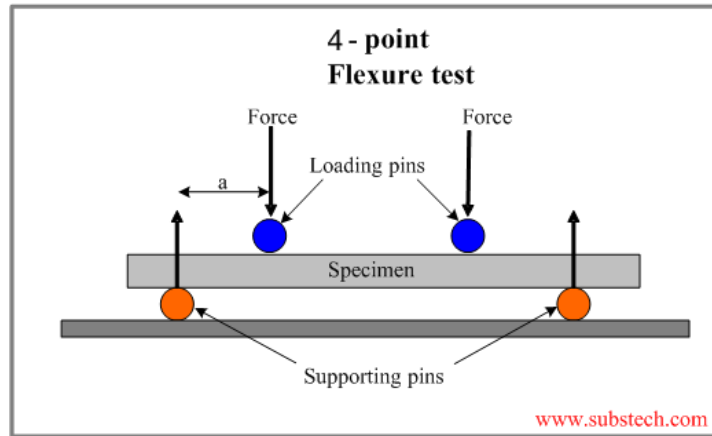


Figure 2.6: Distance ‘a’ is mirrored on both sides; it is typically 1/4 or 1/3 of the distance between the supporting pins. Image from [38].

The moment M is constant and maximum for the space between the loading pins. The loading pins are on the compressive side of the neutral axis while the supporting pins are on the tensile side of the neutral axis. M is calculated as

$$M = a \cdot \frac{F}{2} \quad (2.3)$$

for $a = L/3$ or $L/4$, depending on the chosen set-up.

2.3.2.3 Cantilever bending

Cantilever beams hold a fundamental place in science and engineering, being used everywhere from scanning probe microscopes to flag poles to structural elements in buildings and airplanes. Typically, the elastic modulus of the material in a beam is

known; however, the equations describing the deflection of a beam may be rearranged to find the elastic modulus. Classic cantilever beam theory assumes that the deflection is very small, simplifying the equation of state greatly. Typical boundary conditions are that the beam is clamped in a fixed wall and that a force is applied at the free end of the beam. The distance between the clamp and the location of the applied force is taken as the length of the beam, as deflection will be measured at that point (Figure 2.7).

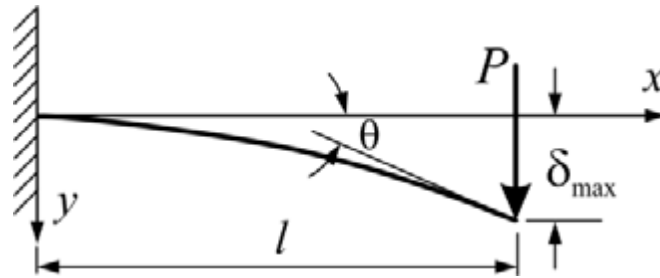


Figure 2.7: A cantilever beam with applied force P and maximum displacement δ . Image from [39].

From the boundary conditions and geometry of the beam, the equation of state is:

$$\frac{M}{EI} = \frac{d^2y}{dx^2} \quad (2.4)$$

where M is the bending moment, EI is the combined elastic modulus and moment of inertia, and the second derivative of y with respect to x is the shape of the deflected beam [40]. This can be solved and rearranged (still for small deflections) as

$$EI = \frac{F \cdot L^3}{3 \cdot h} \quad (2.5)$$

where h is the vertical displacement of the beam under the applied load; h is the same as δ in Figure 2.7. EI is kept as its own variable for most of this work as I can change with geometry.

A cantilever beam with the same clamped-end boundary conditions that undergoes a large deflection cannot be described with Equation 2.5, although Equation 2.4 does still

describe it. Two sources in particular (Belendez et al [41] and Bisshopp et al [42]) took Equation 4 and derived equations of position for a beam of known material properties. The x- and y-positions of any point on a cantilever beam can be described with the following equations:

$$x = \left(\sqrt{2 \cdot \frac{EI}{F}} \right) \cdot (\sqrt{\sin(\varphi_0)} - \sqrt{\sin(\varphi_0) - \sin(\varphi)}) \quad (2.6)$$

$$y = \sqrt{\left(\frac{EI}{F}\right)/2} \cdot \int_0^{\varphi_0} \frac{\sin(\varphi)}{\sqrt{\sin(\varphi_0) - \sin(\varphi)}} d\varphi \quad (2.7)$$

$$q = \int_0^{\varphi_0} \frac{\sin(\varphi)}{\sqrt{\sin(\varphi_0) - \sin(\varphi)}} d\varphi \quad (2.8)$$

where EI is the elastic modulus times the moment of inertia, φ_0 is the angle of the fiber where the beam is loaded, φ is the angle of the beam at a distance s from the clamp (0) to the end of the beam (φ_0), and q is the integral shown in Equation 2.8. The value q is an elliptic integral that was solved numerically in MATLAB; the code is in [Appendix 1](#).

2.3.3 Nanoindentation

Nanoindentation is a type of instrumented indentation on a very small scale. During an indent, unlike typical indentation machines, the machine records the displacement of the tip, the force applied, and the time simultaneously. These combined give a load-depth curve (Figure 2.8).

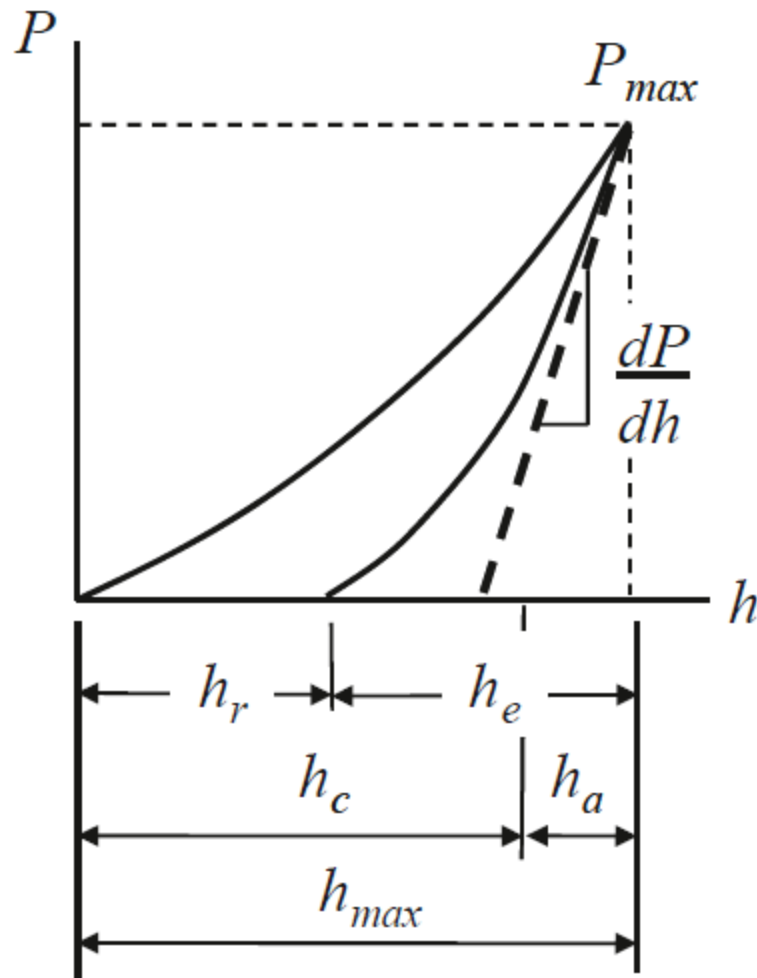


Figure 2.8: A typical load-depth curve obtained from indenting the calibration material is presented. Various important parts are labeled, most notably the contact depth (h_c), final depth (h_r), and the unloading slope (dP/dh). Image from [43].

The final depth (h_r or h_f) is the point at which the indenter stopped registering a load during the unloading portion of its task; this is the residual imprint that would be analyzed during a traditional indentation test. A cross-sectional view of the surface at various points during indentation would resemble Figure 2.9:

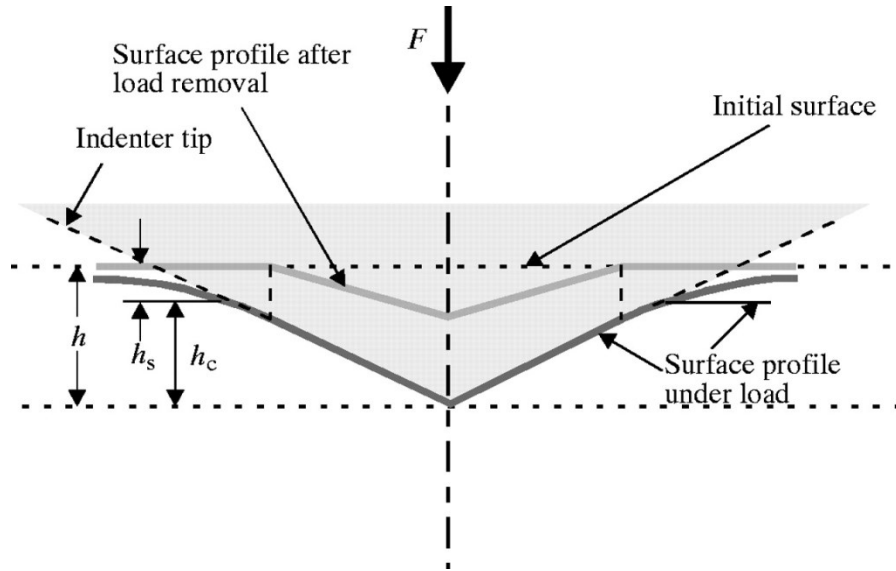


Figure 2.9: At the maximum load, the indenter tip and surface appear as designated by “Surface profile under load”. As the tip moves up during unloading, the material elastically rebounds until it reaches the extent to which it was plastically deformed, as shown by the “Surface profile after load removal”. Image from [44].

A Berkovich tip is a three-sided pyramid with a cone angle equivalent to that of a Vickers tip, the angle being 70.3° [43]. This allows for a direct comparison of the hardness between nanoindentation and regular indentation.

The Oliver-Pharr method of instrumented indentation analysis is widely used in the world of nanoindentation. To calculate the elastic modulus and hardness with this method, it is necessary to know the exact area under the indenter tip. This is done by performing a tip area function (TAF) calibration. The ideal Berkovich indenter has an area that is proportional to h_c^2 [43] [45]. This is not always the case in the experimental setting, due to both the tip having some radius on the very end, and damage and wear to the tip which cause the shape to become non-ideal. Multiple indents to a range of loads are performed on a fused silica standard; the resultant curves are analyzed with the software and

subsequently processed to find the TAF. By plotting the contact depth against the contact area, a depth-to-area equation can be fitted. The equation is

$$A_c = C_0 \cdot h_c^2 + C_1 \cdot h_c + C_2 \cdot h_c^{\frac{1}{2}} + C_3 \cdot h_c^{\frac{1}{4}} + C_4 \cdot h_c^{\frac{1}{8}} + C_5 \cdot h_c^{\frac{1}{16}} \quad (2.9)$$

where $C_0 = 24.5$ (ideal Berkovich), and C_1 - C_5 are fitted to match the real data from the fused silica [46].

From Figure 2.8, the slope of the unloading curve can be readily determined (dP/dh). This slope is used in conjunction with the TAF to determine the reduced elastic modulus of the material being indented. This is found through the equation

$$E_r = S \cdot \left(\frac{4 \cdot A}{\pi} \right)^{-0.5} \quad (2.10)$$

where A is the area as determined by the TAF (A_c) and the contact depth, E_r is the reduced elastic modulus, and S is the stiffness dP/dh [45] [47].

The hardness is determined from the equation

$$H = \frac{P_{max}}{A} \quad (2.11)$$

where P_{max} is the maximum load applied, A is the same as determined by the TAF, and H is the hardness [45] [47]. When a load/unload curve is analyzed in the program, E_r , H , h_c , h_{max} , x -, y -, and other values or constants are all provided in the data readout. Unless otherwise noted, the Oliver and Pharr method of analysis (which is built in to the Hysitron program) is utilized throughout this work.

The particular indenter used in this work was a Hysitron™ Triboindenter with a “high” load (30mN) transducer (SN:5-0243-079). A diamond Berkovich tip from MicroStarTechnologies with tip radius $\sim 20\text{nm}$ was used in conjunction with this transducer [48].

Prior to actual indentation on each sample in this work, a tip-optic calibration was performed. This procedure informs the machine of the x-, y-, z- coordinates of the diamond tip relative to the built-in optics. The accuracy in positioning with this procedure is $\pm 2\text{ }\mu\text{m}$.

2.4 Raman

Raman spectroscopy was first developed in 1928 by Chandrasekhara Raman during his experiments with the inelastic scattering of sunlight [49]. This technique was further improved with the use of monochromatic light, as not all materials have the same Raman shift at different wavelengths. Raman active materials give a measurable photon wavelength shift due to inelastic reflection or transmission of an incident beam (laser). The Raman shift occurs due to an inelastic interaction between the photons of the laser and the vibrational modes of the atoms or molecules in a material (gas, liquid, or solid) [50].

2.4.1 Theory

Raman scattering begins with an incident beam of light, typically a laser, shining on the sample with energy

$$E = E_0 \cdot \cos(2\pi\nu_0 t) \quad (2.12)$$

where E_0 is the maximum energy, ν_0 is the frequency of the laser, and t is time [51].

When the light interacts with a dipole, it can induce a dipole moment

$$\mu = \alpha E \quad (2.13)$$

where μ is the dipole moment, α is the polarizability, and E is the forcing electric field defined above [51]. The polarizability, α , is defined as

$$\alpha = \alpha_0 + \left(\frac{\partial\alpha}{\partial q}\right) \cdot q_0 \quad (2.14)$$

where α_0 is the equilibrium polarizability, q_0 is defined as the amplitude of nuclear displacement due to vibration, and $\frac{\partial\alpha}{\partial q}$ is the change in polarization with respect to change in displacement [51]. The variable q is defined as

$$q = q_0 \cdot \cos(2\pi\nu_m t) \quad (2.15)$$

where q_0 is the equilibrium vibration (no external forcing electric field), ν_m is the frequency of oscillation of the polarization, and t is time [51]. Following this, the definitions of α , q , and E can be substituted into the equation for an induced dipole Equation (13), and expanded:

$$\mu = \alpha \cdot E_0 \cdot \cos(2\pi\nu_0 t) \quad (2.16)$$

$$\mu = \alpha_0 \cdot E_0 \cdot \cos(2\pi\nu_0 t) + \left(\frac{\partial\alpha}{\partial q}\right)_0 \cdot q \cdot E_0 \cdot \cos(2\pi\nu_0 t) \quad (2.17)$$

$$\mu = \alpha_0 \cdot E_0 \cdot \cos(2\pi\nu_0 t) + \frac{1}{2} \cdot \left(\frac{\partial\alpha}{\partial q}\right)_0 \cdot q \cdot E_0 \cdot [\cos(2\pi(\nu_0 + \nu_m)t) + \cos(2\pi(\nu_0 - \nu_m)t)] \quad (2.18)$$

The first term, $\cos(2\pi\nu_0 t)$, is the Rayleigh scattering of the sample. The second term, $\cos(2\pi(\nu_0 + \nu_m)t)$, is the Stokes scattering, and the third term, $\cos(2\pi(\nu_0 - \nu_m)t)$, is the anti-Stokes scattering.

The two types of Raman shift are, respectively, Stokes and anti-Stokes scattering with both being very weak compared to the elastic process of Rayleigh scattering. A micro-Raman system filters out the Rayleigh scattered light so only Raman scattered photons are detected. A diagram showing the relative energy shifts between Rayleigh, Stokes, and anti-Stokes scattering is provided in Figure 2.10.

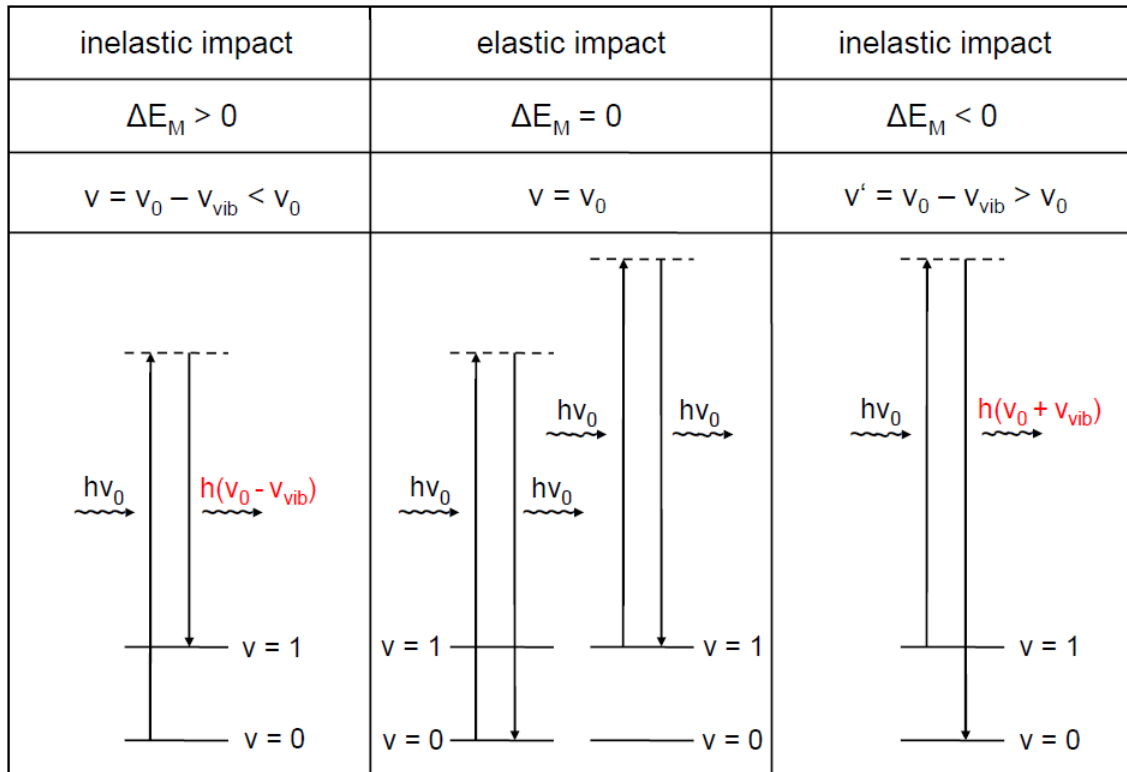


Figure 2.10: Rayleigh scattering (middle) returns light at the same wavelength that it impinged on the material with; Stokes (left) and anti-Stokes (right) return it at different wavelengths. The change in wavelength is what is measured in Raman spectroscopy. Image from [50].

The vibrational energy states shown are the positions of electrons within the material. Because most electrons are found at the lowest possible energy state, the anti-Stokes shift is much rarer as it requires that the excited electron already be at an elevated energy relative to E_0 , rather than being excited from its ground state.

A Renishaw™ inVia microRaman spectrometer was used throughout this work. This particular machine measures the Stokes shift only. It is equipped with three lasers: 514nm Ar, 633nm HeNe, and 785nm solid state. The 514nm and 633nm lasers are circular with a Gaussian power spread, whereas the 785nm laser is by default a line laser with the same power distribution along the length of the beam. Filters can be placed in front of each laser to change it to either a line or circular beam, respectively [52]. Once the laser has gone through focusing and edge filtering and impinged on the sample, it is directed through a monochromator (1200 l/mm for 633nm and 785nm lasers, 1800 l/mm for the 514nm laser) which spreads the beam based on wavelength. The beam then hits a charge-coupled device (CCD). The intensity of the beam in intervals of $\sim 1.5 \text{ cm}^{-1}$ wavelength is plotted on screen for further analysis.

The built-in software and its upgraded version (WiRE 3.4 and 4.2, respectively) are capable of analyzing single peaks or multiple peaks at the same time. Once a fitting procedure has been established and saved, it can be used to analyze maps of data – it will fit the desired peaks for large data sets automatically and a sub-map may be generated for any individual peak's position, height, width, etc. The process to accomplish this is outlined in Chapter 3.3.

Penetration depth is useful for knowing the volume of the sample being probed and is very important if one is attempting to probe small volumes and surface-specific phenomena, such as residual stress [4]. The equation for penetration depth is:

$$D_p \cong \frac{\lambda_{exc}}{4\pi nk} = \frac{1}{\alpha(\lambda)} \quad (2.19)$$

where D_p is penetration depth, λ_{exc} is the excitation wavelength, n is the index of refraction, k is the extinction coefficient, and α is coefficient of absorption for a particular lambda wavelength [53] [54].

2.4.2 Raman for stress investigations

Due to the nature of Raman shift – that an electric field interacts with the bonds of a molecule inelastically, it naturally follows that a change in the bond will affect the Raman shift. The change in the bond could be the difference between a single-bond or shorter double-bond, a stretching of the bond due to internal defects (dislocations, interstitials), or an external stress on the material that causes strain [55]. This work focused on the latter – the effects of an external force on the Raman spectrum of a material.

The effects of stress on the Raman spectrum of a material starts with the assumption that the bond between two atoms acts as a harmonic oscillator with a restoring force

$$F = -k \cdot \frac{\Delta l}{l_0} \quad (2.20)$$

where F is the restoring force, k is the bond stiffness, l_0 is the original separation of the atoms, and is Δl the change in bond length [55]. The resulting potential energy well of a harmonic oscillator is

$$V = \frac{1}{2} \cdot k \cdot (\Delta l)^2 \quad (2.21)$$

where V is the potential energy and k and Δl are the same as above. For small deviations from a stress-free state, this is a valid approximation; however, as the bond is separated further the model begins to fail leading to the introduction of the anharmonic oscillator which can have its potential energy described as:

$$V = \frac{1}{2} \cdot k \cdot (\Delta l)^2 + k' \cdot (\Delta l)^3 \quad (2.22)$$

where V , k , and Δl are the same as above, and k' is the anharmonic restoring force [55]. It must further be noted that not only are real atomic bonds anharmonic, but they are in discrete energy levels:

$$E_n = h\nu \cdot (n + \frac{1}{2}) \quad (2.23)$$

where E_n is the energy, $h\nu$ is Planck's constant multiplied by the fundamental vibration frequency, and n is the energy level (0, 1, 2, ...) [56]. The factors can be shown graphically as in Figure 2.11.

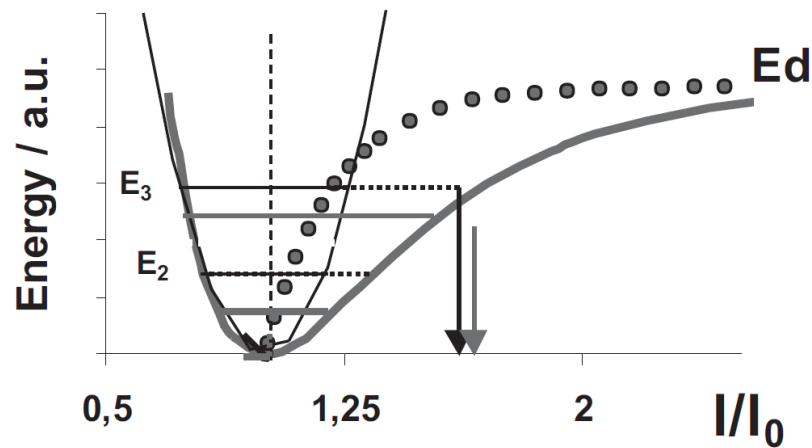


Figure 2.11: The energy of a bond is plotted against the change in bond length. The parabola is the harmonic oscillator model, while the solid gray line is the anharmonic oscillator model. Discrete energy levels are shown as well. Image from [55].

Under an external strain that forces a change in bond length, the anharmonicity affects the Raman wavenumber shift as

$$\Delta\omega = S^\epsilon \times \Delta\epsilon \quad (2.24)$$

where $\Delta\omega$ is the change in wavenumber, $\Delta\epsilon$ is the strain, and S^ϵ is the elastic constants of the material [55]. This can be re-written in terms of stress through derivation as:

$$\Delta\omega = S^\epsilon \times \Delta\epsilon = S^\epsilon \times \frac{\Delta\sigma}{100 \times E} = S^\sigma \times \Delta\sigma \quad (2.25)$$

where $\Delta\omega$, $\Delta\epsilon$, S^ϵ are the same as above, E is the constant obtained by Hooke's law that relates stress to strain, and S^σ is elastic constants of the material with respect to stress while $\Delta\sigma$ is the stress [55].

The two kinds of external stress a material can experience are hydrostatic and deviatoric; hydrostatic being a stress applied from every direction on a material – an example is the pressure of water at the bottom of the ocean and may be replicated via diamond anvil cells in a lab. Deviatoric stress is a directional stress applied to a material; it may be uniaxial, biaxial, tri-axial, and observed as a shear stress. Given an arbitrary state of stress characterized by a matrix:

$$\sigma_{overall} = \begin{bmatrix} \sigma_1 & \sigma_4 & \sigma_5 \\ \sigma_4 & \sigma_2 & \sigma_6 \\ \sigma_5 & \sigma_6 & \sigma_3 \end{bmatrix} \quad (2.26)$$

The average of the matrix times an identity matrix is the hydrostatic stress [57]:

$$\sigma_{hydro} = \frac{\sigma_1 + \sigma_2 + \sigma_3}{3} \quad (2.27)$$

Under pure hydrostatic stress, a material will experience only volume change and no shape change [58]. The associated change in Raman spectrum of a material will reflect that all bonds have shrunk or expanded by the same amount.

The deviatoric stress is the stress given in the matrix above minus the hydrostatic stress:

$$\sigma_{overall} = \begin{bmatrix} \sigma_1 - \sigma_h & \sigma_4 & \sigma_5 \\ \sigma_4 & \sigma_2 - \sigma_h & \sigma_6 \\ \sigma_5 & \sigma_6 & \sigma_3 - \sigma_h \end{bmatrix} \quad (2.28)$$

As deviatoric stress causes a change in the bond length in a specific direction in a material, the subsequent change in the Raman spectrum will not be the same as the change with respect to hydrostatic stress [59].

Due to the large variety of crystal symmetries, the change in a Raman spectrum may be different with change in either the orientation of the laser (along specific axes) or with change in the primary direction of stress along a specific axis [60] [6] [59]. For each crystal symmetry, the change in Raman spectrum with stress must be either calculated or measured for both hydrostatic stresses and uniaxial/deviatoric stresses.

2.5 Materials

A varied selection of materials were studied in this work, notably including semiconductors and structural ceramics. Selected mechanical and optical properties are given for each material studied, as well as any significant notes or deviations. When possible, the elastic constants of a material are given, as well as the Young's modulus (E), hardness (H), and flexural or tensile strength.

2.5.1 Silicon

Silicon is one of the most widely studied semiconductors, being used in almost every electronic device in the world today. Single crystal Si is typically grown via the Czochralski method [61], where a seed crystal is used to slowly grow a larger crystal of silicon from a melt. The resulting boule is then cut along desired crystallographic planes,

polished, and sold. Silicon has a diamond-cubic crystal structure and a bandgap of 1.1eV [62]. Selected mechanical properties of single crystal Si are given in Table 2.2.

Table 2.2: Selected mechanical properties relevant to this work are presented.

Property	Value
C11	166 GPa [63]
C12	64.0 GPa [63]
C44	74.6 GPa [63]
Poisson's ratio	0.28 [63]
Hardness	13 GPa [64]
Young's modulus	190±15 GPa [64]
Flexural strength	190 MPa [65]

As this work examined the Raman spectrum of silicon, pertinent information regarding such is given. The coefficient of absorption for Si at room temperature depends on wavelength, being $3.27 \times 10^3 \text{ cm}^{-1}$ at 633 nm [66] [67]. A sample Raman spectrum of silicon is given in Figure 2.12.

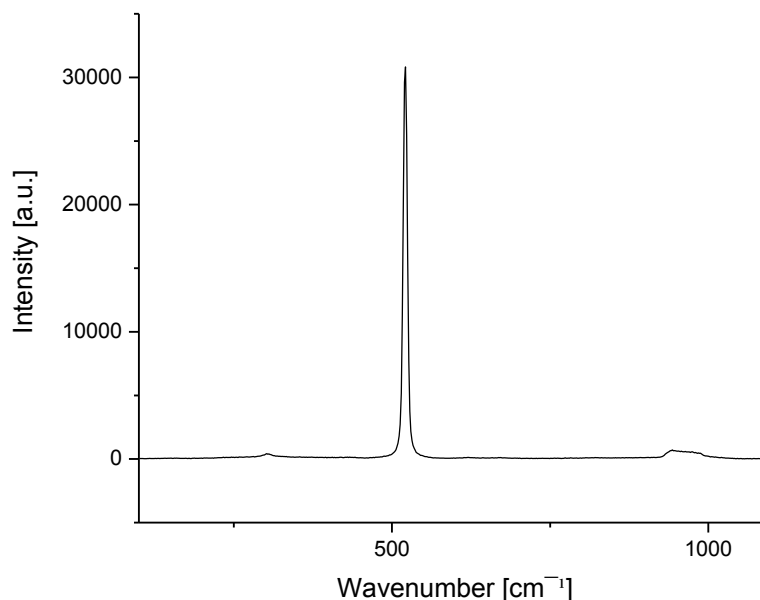


Figure 2.12: A typical Raman spectrum of single crystal Si from 100 cm^{-1} to 1100 cm^{-1} . This range encompasses the large peak at 520.6 cm^{-1} and a small set of secondary peaks near 900 cm^{-1} .

The exact location of the sharp peak is in debate [68] [69] [5] and generally agreed upon as between 520 cm^{-1} and 521 cm^{-1} ; a location of 520.60 cm^{-1} was used throughout this work.

2.5.2 Silicon Carbide

Silicon carbide is one of the hardest materials behind diamond and is extremely important in both physical metallurgy (added to steel melts to increase the temperature) and armor ceramics. Silicon carbide occurs naturally as moissanite, but is more typically mass produced by the Acheson process or chemical vapor deposition [70]. The Acheson process is used primarily for the creation of SiC powder for later processing and sintering, whereas CVD is used to make high-purity SiC for semiconductor applications [71]. The Acheson process takes a carbon source and heats it with silica until the silica

decomposes and a series of reactions take place ending with the formation of silicon carbide solids and carbon monoxide gas (Figure 2.13) [70].

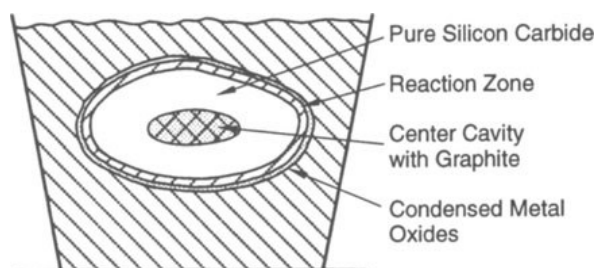


Figure 2.13: A schematic of the cross-section of a crucible that is used to make SiC via the Acheson process. The entire crucible is heated by direct resistance heating to cause the reaction to take place. Temperature varies between 1800K and 2200K. Image from [70].

CVD SiC can be grown via the Lely process where a thermal gradient drives vaporized SiC to deposit and grow single crystals on a porous carbon substrate or on other SiC single crystals [72] [73]. Crystals grown this way can be sectioned and used as semiconductor devices.

This leads directly to the importance of the crystal structure of silicon carbide: at the same stoichiometry, SiC can have many different polytypes [74]. Silicon carbide is composed of a Si atom surrounded by four C atoms in a tetrahedral shape. The stacking of the tetrahedra causes different polytypes to form. The most common polytypes are 3C, 4H, and 6H. These designations refer to the stacking order of the planes in silicon and carbon tetrahedra; Figure 2.14 shows the difference between selected polytypes.

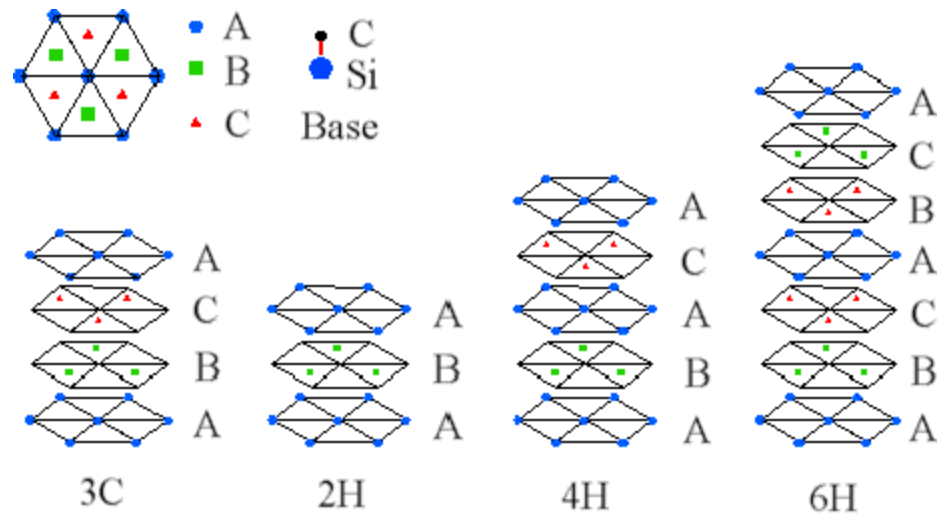


Figure 2.14: By alternating the order of Si and C tetrahedra, different polytypes can be formed. Image from [75].

There is no significant difference in the bulk mechanical properties of the different polytypes of SiC, but there is a significant difference in the Raman spectrum of each one, shown in Figure 2.15 and Table 2.3.

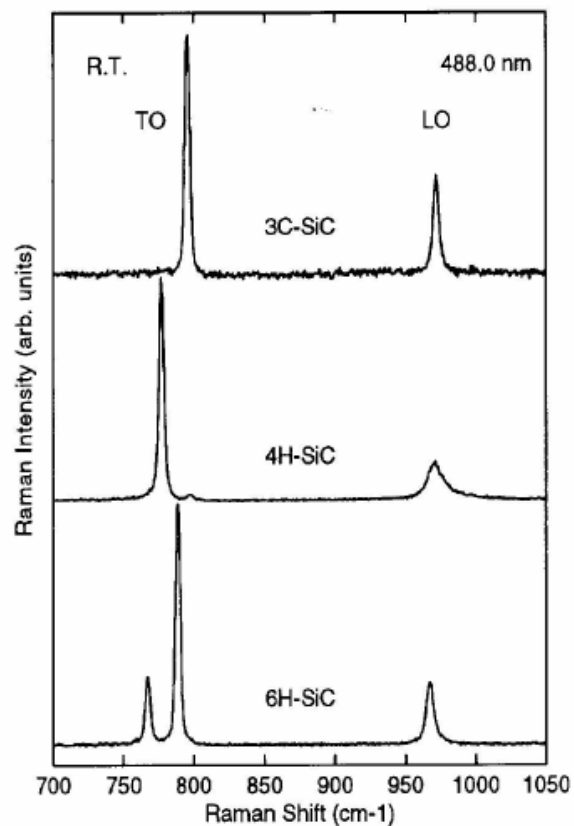


Figure 2.15: Example Raman spectra of 3C, 4H, and 6H SiC are shown. The peak locations are given in Table 2.3. Image from [76].

Table 2.3: A comparison of the primary peaks seen of three polytypes of SiC in a back-scattered configuration Raman spectrometer. A significant difference between peaks is not just location, but also intensity, as seen in Figure 2.15.

Polytype	Peak1	Peak 2	Peak 3
3C	796 cm ⁻¹	970 cm ⁻¹	
4H	777 cm ⁻¹	796 cm ⁻¹	970 cm ⁻¹
6H	776 cm ⁻¹	789 cm ⁻¹	964 cm ⁻¹

Amorphous silicon carbide can have a Raman spectrum similar to that shown in Figure 2.16.

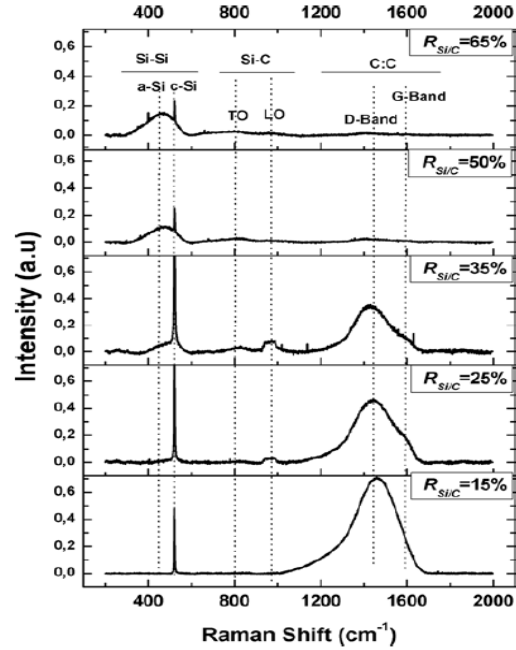


Figure 2.16: At different stoichiometries, the Raman signal of SiC can vary significantly. Image from [77].

The coefficients of absorption for 3C-SiC and 4H-SiC at 633 nm incident light are 150 cm^{-1} and 54325 cm^{-1} [78] [79].

Selected mechanical properties of silicon carbide are given in Table 2.4. Young's modulus is E and hardness is H ; elastic constants are C_{ij} .

Table 2.4: Selected mechanical properties of two polytypes of silicon carbide are given.

Property	3C	4H	All
C11	290 GPa [80]	501 GPa [81]	
C12	235 GPa [80]	111 GPa [81]	
C13		52 GPa [81]	
C33		553 GPa [81]	
C44	55 GPa [80]	163 GPa [81]	

E			390-700 GPa [82]
H			25-36 GPa [83]
Poisson's ratio			0.18-0.19 [84]
Flexural strength			186 MPa [84]

2.5.3 YAG

Yttrium aluminum garnet (YAG) is a crystalline material that lases in the IR range; it has been shown that it can be grown into a single crystal fiber, replacing glass fiber lasers in that wavelength range [85]. A well-tested growth method utilizes a laser-heated growth pedestal [85] to melt a source bar of YAG, slowly pulling a single crystal fiber from the melt. This single crystal is started with an oriented seed crystal and is typically 1/3 the size of the source. Figure 2.17 provides a schematic of this set up.

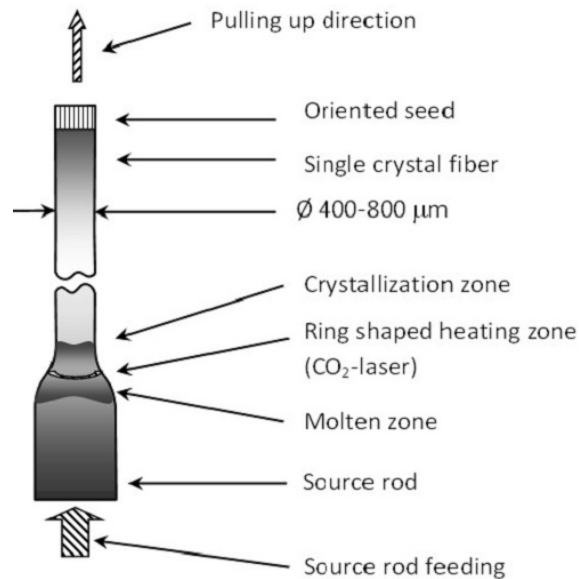


Figure 2.17: An oriented seed is attached to a motor that pulls it vertically up from the melt, drawing a single crystal fiber with it. Image from [86].

These crystals can be doped before growth during either the initial boule forming stage or by covering a grown crystal in a doped sol-gel and regrowing the crystal, introducing the dopant to the fiber [87]. Doping YAG with rare-earth (RE) ions such as Nd, Ho, and Er allows the YAG to become an active rather than passive lasing material. The reason to choose a RE:YAG fiber over a rod or disk is that the fiber has a much higher surface area to volume ratio, allowing for better cooling under high power operations [88].

The unit cell of YAG is very complex, being cubic and comprising of 8 units of $\text{Y}_3\text{Al}_5\text{O}_{12}$ (Figure 2.18).

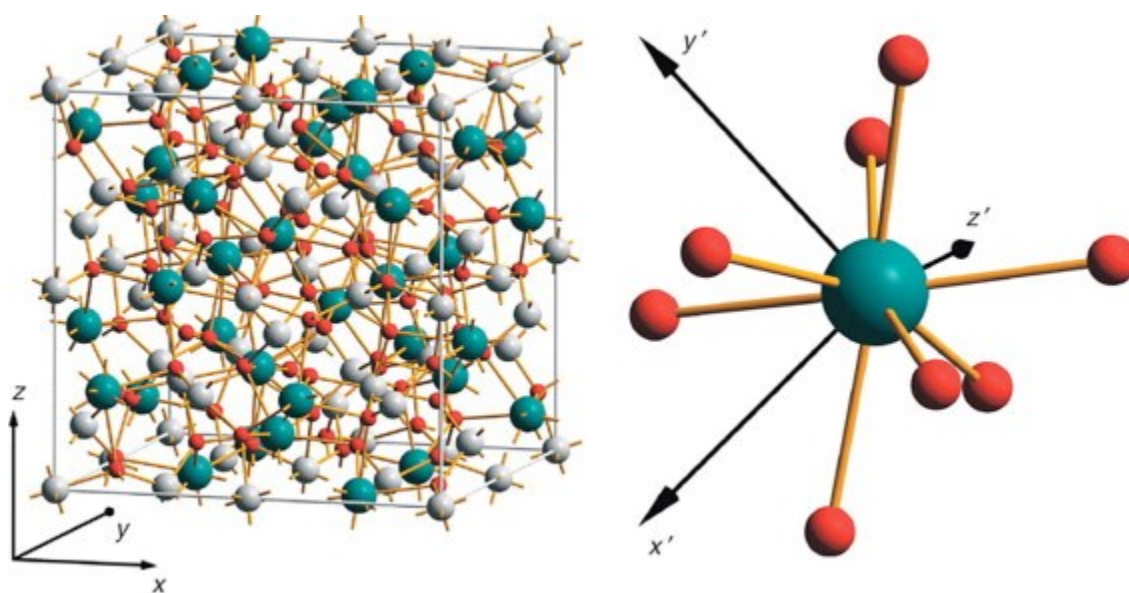


Figure 2.18: The unit cell of YAG is shown; green is yttrium, white is aluminum, and red is oxygen. Rare earth ions substitute in place of yttrium when doped. Figure from [89].

The Raman spectrum from undoped YAG shows peaks arising from distinct bonds within this structure (Figure 2.19 and Table 2.5):

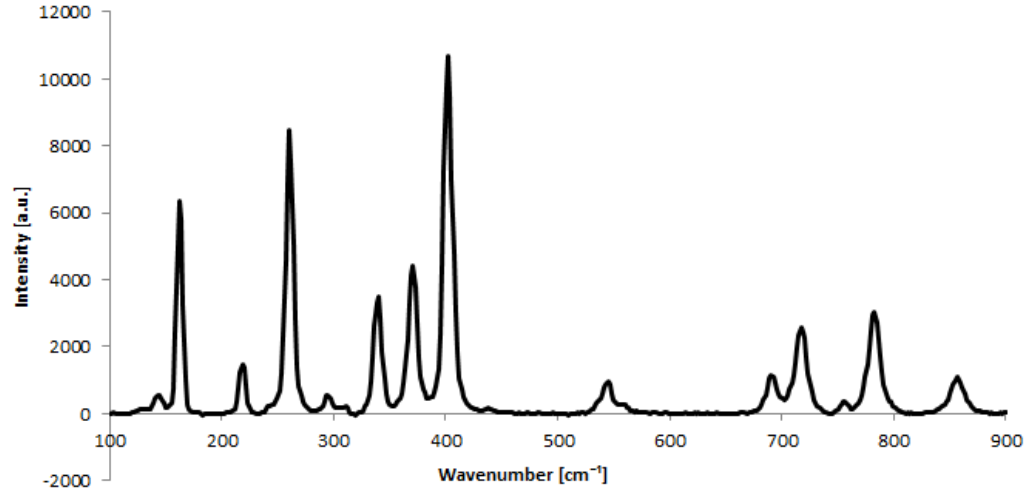


Figure 2.19: An example Raman spectrum from an undoped single crystal YAG source bar is shown.

Table 2.5: Experimental and literature peaks (HiP) were given peak assignments.

Peak (cm ⁻¹) (Exp/HiP [90])	Symmetry	Origin
143/145	T _{2g}	
162/163	E _g	Y translation
218/220	T _{2g}	Y translation
251		
263/263	T _{2g}	Translation, rotation, and v3 of AlO ₄
294/295	T _{2g}	Translation, rotation, and v3 of AlO ₄
339/340	E _g	Translation, rotation, and v3 of AlO ₄
370/370	A _{1g}	Translation, rotation,

		and v3 of AlO ₄
402/402	T _{2g}	Translation, rotation, and v3 of AlO ₄
543	T _{2g}	v2 of AlO ₄
559/559	A _{1g}	v2 of AlO ₄
691/691	T _{2g}	v1 and v4 of AlO ₄
717/718	T _{2g}	
755/754	E _g	
782/783	A _{1g}	v1 and v4 of AlO ₄
856/857	T _{2g}	v1 and v4 of AlO ₄

Selected mechanical properties of single crystal YAG are given in Table 2.6:

Table 2.6: Selected mechanical properties of yttrium aluminum garnet are given.

Property	Value
C11	339 GPa [91]
C12	114 GPa [91]
C44	116 GPa [91]
E	280±7 GPa [92]
H	13.5 GPa [93]
Poisson's ratio	0.23±0.02 [92]
Tensile strength	280 MPa [92]

2.5.4 Feldspar

Feldspars are used throughout the entire ceramics industry, in everything from fine china to coffee mugs to toilet porcelains. It is a common and essential material in the modern world; further, because it is found across the globe, it is important to geologists as a mineral. Rather than a single material, feldspar is an entire class of materials with the same base chemistry. Feldspar can be $\text{Na}_x\text{Ca}_{1-x}\text{AlSi}_3\text{O}_8$; for $0.9 \leq x \leq 1$ the feldspar is albite, for $0.4 \leq x \leq 0.6$ the feldspar is labradorite, and for $0 \leq x \leq 0.1$ the feldspar is anorthite [94] [95] [96]. Feldspar may have potassium as an end-member instead: KAlSi_3O_8 , being orthoclase if that is the case [97].

The flexural modulus of all feldspars varies between 8.9 MPa and 38 MPa [98] with a typical value of ~ 16 MPa [99]. Selected elastic constants for albite and labradorite are given in Table 2.7. Very few studies have been done on the elastic modulus or flexural modulus of these materials on their own – more has been done on composites of these materials in such forms as granite.

Table 2.7: The bulk modulus (K), shear modulus (μ), and calculated elastic modulus (E) are given for albite and labradorite.

Property	Albite	Labradorite
K	60 GPa [100]	75 GPa [100]
μ	35 GPa [100]	37 GPa [100]
E	88 GPa	95 GPa

Feldspars are tectosilicate structures comprised of tetrahedral rings of TO_4 , where T is Si or Al. An example of the unit cell for microcline is given in Figure 2.20.

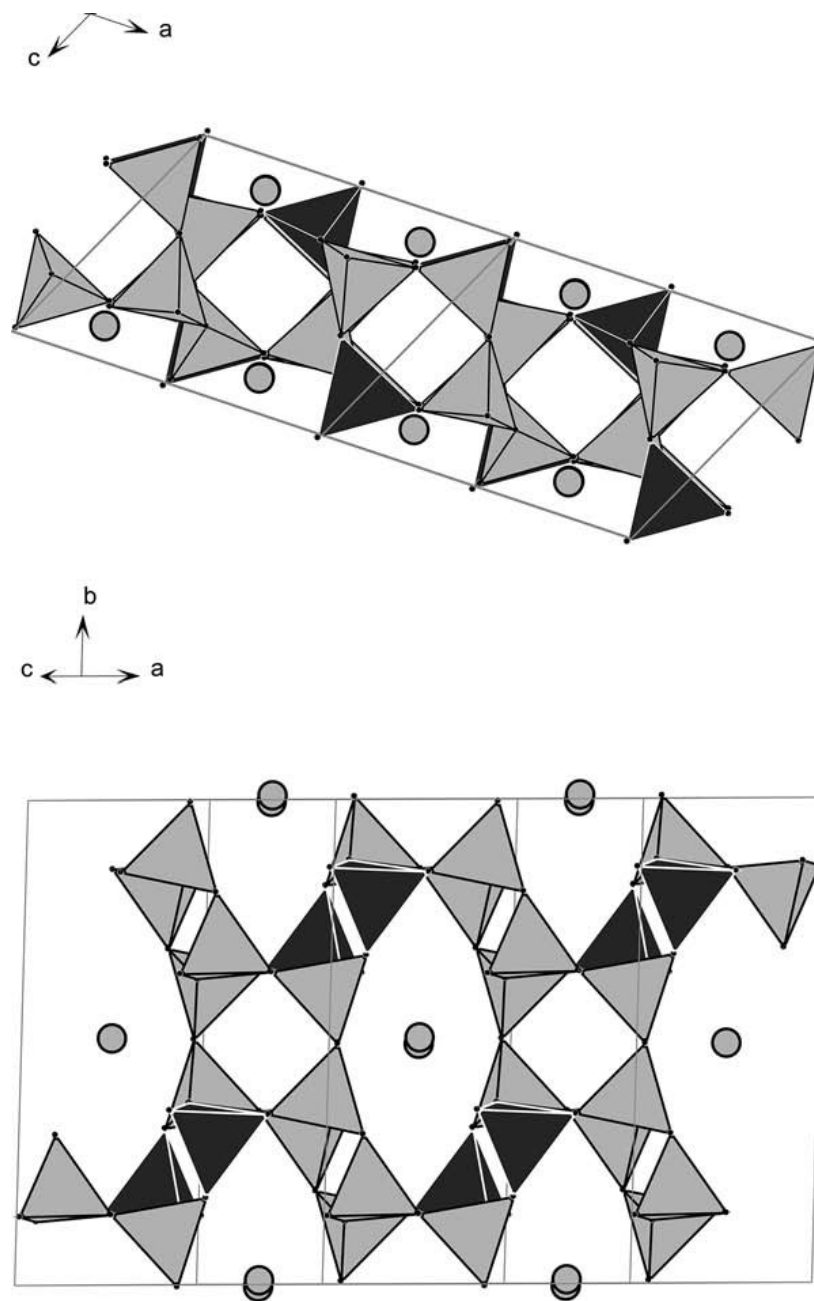


Figure 2.20: Two views of the same unit cell are given; the light gray tetrahedra are silicon-bearing tetrahedra and the dark gray tetrahedra are aluminum bearing. The end-member ions are gray circles. Figure from [101].

Example Raman spectra of albite and labradorite are given in Figure 2.21 and Figure 2.22.

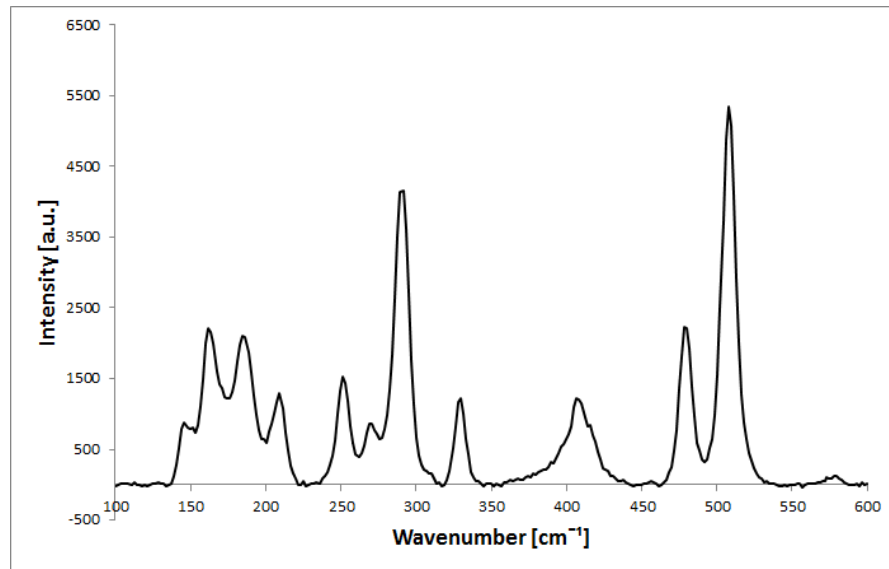


Figure 2.21: An example of the Raman spectrum obtained from albite.

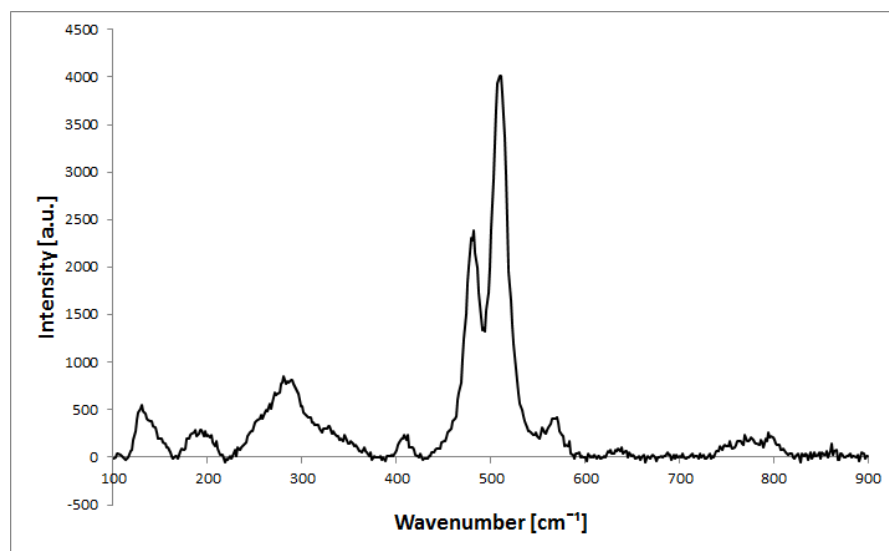


Figure 2.22: An example of the Raman spectrum obtained from labradorite.

2.5.5 Quartz

Quartz (silicon dioxide, silica) is important in both the semiconductor world as an insulator and in the armor world as a window transparent over a large range of wavelengths. It is often used in an amorphous state in semiconductors as it is formed by reacting oxygen with the silicon surface, but used in crystalline form as a substrate.

Further, it is found in the form of crystalline quartz throughout the world, making it useful to both ceramicists and geologists as a mineral.

Quartz can have many polymorphs (such as coesite, moganite, and chalcedony) but only “pure” quartz is considered in this work. Selected elastic constants of quartz are given in Table 2.8.

Table 2.8: Selected mechanical properties are presented.

Property	Value
C11	87.17 GPa [102]
C33	105.8 GPa [102]
C44	58.27 GPa [102]
C66	40.28 GPa [102]
E11	78.01 GPa [102]
E33	102.7 GPa [102]
Flexural Modulus	45 MPa [103] [104]

The Raman spectrum of single crystal silica is given in Figure 2.23 and the origin of each peak is given in Table 2.9.

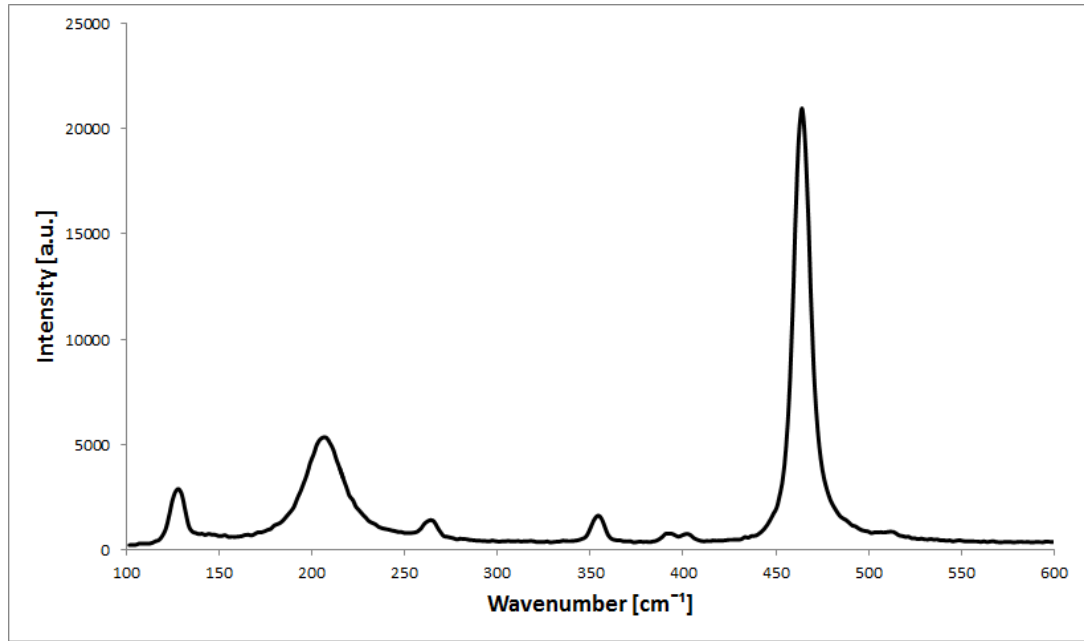


Figure 2.23: An example Raman spectrum of quartz is given. Intensities of peaks vary with orientation with respect to the incident laser, but all peaks are visible regardless of orientation.

Table 2.9: Selected peaks and their symmetry origins are presented.

Peak	Origin [105]
128 cm ⁻¹	E _(TO+LO)
206 cm ⁻¹	A ₁
265 cm ⁻¹	E _(TO+LO)
355 cm ⁻¹	A ₁
394 cm ⁻¹	E _(TO)
401 cm ⁻¹	E _(LO)
464 cm ⁻¹	A ₁
511 cm ⁻¹	E _(LO)

2.6 Helium Ion Microscopy

Scanning Electron Microscopes work by sending a beam of electrons through a column and hitting a sample with those electrons; the energy of the electrons cause secondary electrons to be ejected from the sample [106]. The secondary electrons are gathered by a detector specific to electrons (rather than X-Rays) and an image is formed based on the angle and energy the electrons hit the detector with.

Similar to a Scanning Electron Microscope (SEM), a Helium Ion Microscope (HIM) shoots a beam of charged particles at a sample and utilizes the backscattered electrons to form an image. The primary difference between the two is that the HIM has a sharpened, cooled needle with a high positive voltage over which helium atoms flow; as they flow they lose an electron and become charged as well [107]. The tip is sharpened to three atoms and one of these is chosen as the emitter, creating a very small spot size [108]. These are then sent through electrostatic lenses before impinging on the sample. Secondary electrons are captured and used to form an image of the sample. A schematic of the working column is shown in Figure 2.24.

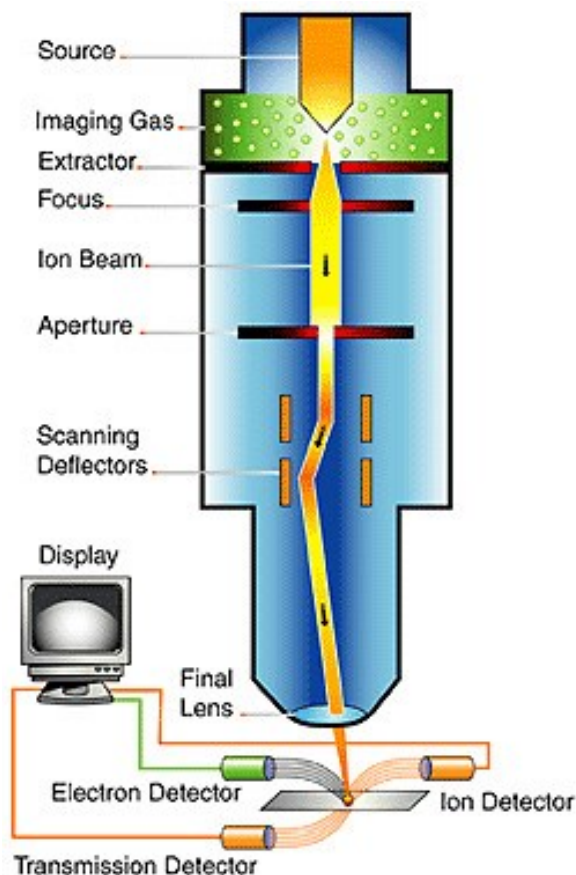


Figure 2.24: A schematic of the beam column with various components is given. The electron detector was used in this work to detect secondary electrons. Image from [109].

Insulating samples can be examined without a gold or carbon coating by flooding the sample with a secondary beam comprised of electrons [107]. Due to both the small spot size (0.25 nm) and the smaller deBroglie wavelength of the He ions ($\sim 1/10$ that of electrons), the resolution of a HIM is far greater than that of an SEM [107].

2.7 Fractography

Fractography is the study of how a fracture surface can indicate what happened at failure. This work concentrates on the fracture of brittle materials; as such, significant discussion of yielding and plasticity will be left out.

Assuming a part has been designed properly, the material chosen appropriately, and corrosion is not a factor, there are four primary factors that will influence the fracture of a material: temperature, thermal shock, speed of loading, and if there is a stress concentrator present [110]. The work performed in this study kept the temperature stable and did not investigate the effects of thermal shock on the materials in question. At cryogenic and elevated temperatures, the speed of loading matters a great deal, as (especially at elevated temperatures) creep can play a large role in how the ceramic behaves prior to failure [111]. Speed of loading is also important during very small scale testing where the pressure can be high enough to cause phase transformations, such as during nanoindentation [112]. At room temperature and the tests performed in this work, the speed of loading will not play a significant role in the testing of these fibers. Stress concentrators have the effect of locally multiplying the overall stress on a part. Stress concentrators can be cracks (Griffith flaw theory [113]), scratches from polishing, geometry (sharp angles in a part or holes drilled through it), or surface morphology (inherently smooth or rough surfaces, pitting from corrosion) [114]. The most common of these is the observation of a crack as a flaw, often related as the stress intensity factor K_I , K_{II} , or K_{III} , related to the type of material, crack shape, and crack size [111]. These factors relate the stress intensity in tension (K_I), in-plane shear (K_{II}), and out-of-plane shear (K_{III}) (Figure 2.25) [111].

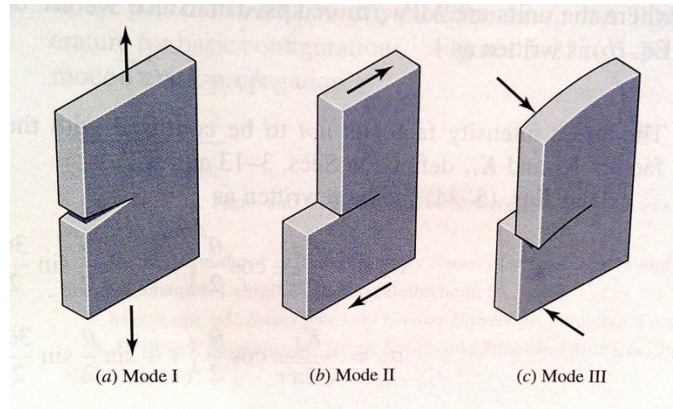


Figure 2.25: The stress intensity is related to the direction of the forces acting to open a crack. Image from [115].

Flaws are (unless induced by machining or processing) randomly located throughout a ceramic material. In polycrystalline ceramics, flaws may often be the join between crystals, but can also be inclusions or voids. The stochastic nature of flaws leads to the randomized nature of ceramic fracture – ceramics do not always fail at the exact same stress. The strength of ceramic materials can be described by their Weibull modulus. The Weibull modulus is a measure of the distribution of flaws that affect the strength of the material [116] and provides a statistical measure of the strength of a given material [117].

Brittle materials most often fail with no warning because unlike ductile materials that deform plastically before complete failure, the ultimate strength of brittle materials is extremely close to or even below their yield strength [110] [111] [114]. This is due in part to the type of bonding in ceramic materials. The effect of having both negative and positive charges present means that when crystal planes slip, they must move two atoms in distance to maintain charge symmetry and reduce local charging. This leads to an increase in the Peierls stress (the stress needed to move a plane of atoms [118]), which is a limiting factor in determining which slip system will glide [111]. If there are fewer than

five slip systems in the material under a specified temperature, hydrostatic pressure, and geometry, ductility will not occur [111] [119]. There are few slip systems available to SiC, indicating that it will not undergo plastic deformation prior to failure [119].

3 Experimental Procedures

The following sections show how much of this work was performed, including the process for using the TriboIndenter, how small- and large-deflection cantilever bending was carried out and analyzed, how the Renishaw micro-Raman system works, and how fractography can be applied. Missing from this section is any discussion regarding the use of the four-point bend set-up, as the experimental procedure for using it is detailed in the paper containing its development and use.

3.1 Nanoindentation

Nanoindentation must be performed on samples that are stable, flat, have low surface roughness, and have a surface nearly parallel with the stage. Samples for this study were always adhered to 2.5mm thick steel puck that was polished on both sides to 600 grit (10.6 μm particle size, to ensure flatness). A thin layer of cyanoacrylate glue was used for this. If the sample was only a fiber, the fiber was cleaned with acetone and ethanol before being placed on the thin layer of glue. Samples that required polishing were polished with progressively finer grades of diamond lapping pad, ending with a diamond pad with 1 μm particle size. Prior to being placed in the Triboindenter chamber, all samples were wiped down with ethanol.

The proper tip for nanoindentation was selected – in this case a Berkovich tip with nominal tip radius of 15 nm – and installed following instructions provided in the manual. The entire system was then turned on (Figure 3.1) and allowed to come to steady state.



Figure 3.1: The Triboindenter system is shown; it is turned on in the numbered order. The large white “egg” is the chamber in which the tip and sample are located.

A tip-optic calibration with a single indent at any load is then performed on an aluminum standard; this effectively tells the machine what the length of the tip is, as this can vary between manufacturers and types of tip. Following this, a tip area function calibration is performed on a fused silica standard. The tip area function is performed to obtain an accurate area-depth curve for the depths that will be probed on the actual sample.

The safety limits (location of the sample), positions (locations within the safety limits where indents are to be performed), pattern (often grid of indents), and load functions are chosen for the sample. An example of a typical load function used in this study is presented in Figure 3.2.

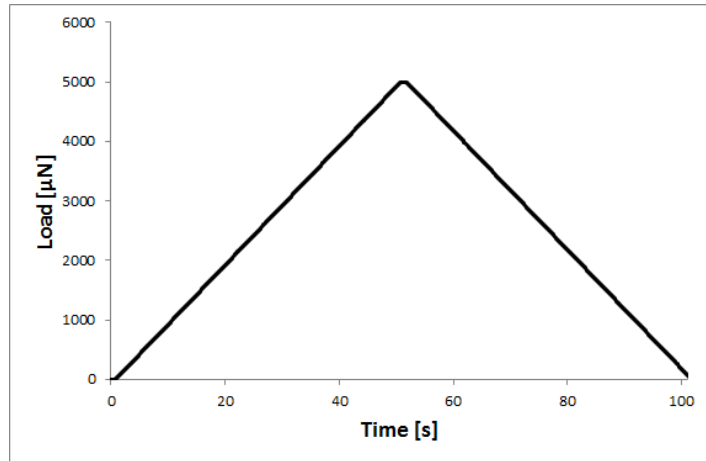


Figure 3.2: This particular load function goes to a maximum load of 5mN over 50s, holds that load for 1s, and then unloads at the same rate.

Immediately before starting the method that will execute a series of indents on the sample, a second tip-optic calibration was always performed; this kept the error associated with position low.

The load-depth curves (Figure 3.3) were analyzed in-software in batches. The analysis outputs a table containing the name of each nanoindent, the various depths described in section 2.3.3, the maximum load, and most importantly, the reduced elastic modulus and hardness calculated via the Oliver-Pharr method, and x- and y-positions of each indent. This data was then used to generate maps of the modulus and hardness and for other relevant plots.

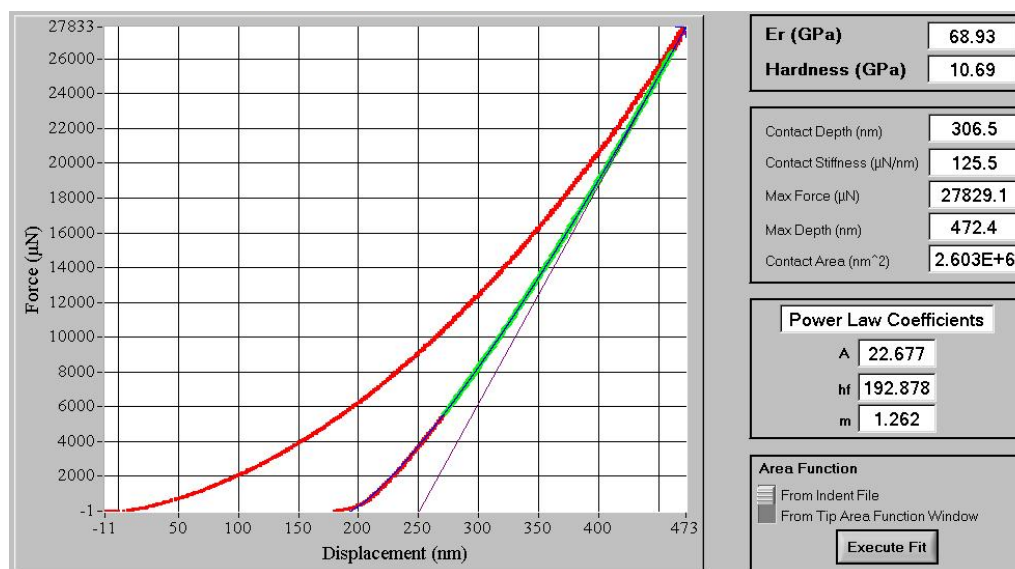


Figure 3.3: An example load-depth curve for fused silica is given along with a readout of the calculated reduced modulus and hardness.

3.2 Cantilever bending

As with nanoindentation, 2.5mm thick steel pucks polished to 600 grit were used to adhere fibers for cantilever bend testing. The pucks were typically 13mm wide and 16mm long. A plastic coverslip was cut into pieces roughly 10mm wide by 20mm long. A two-part epoxy adhesive (JB-Weld™) was mixed and thinly applied to the steel puck. A single fiber up to 70mm long was carefully placed on the adhesive, with ~8mm of fiber in contact with the adhesive. Adhesive was thinly applied to one side of a piece of coverslip and this was then sandwiched on top of the fiber (Figure 3.4). The whole assembly was allowed to cure 24 hours before testing began.

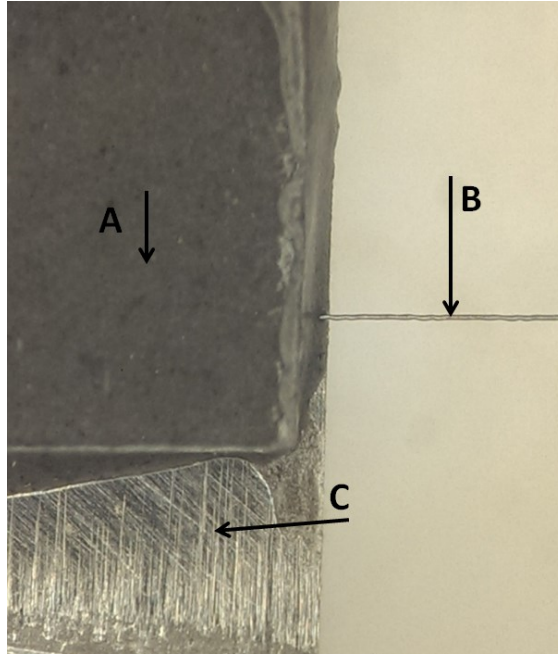


Figure 3.4: An example of a fiber (B) protruding from the sandwiched steel (C), adhesive, and coverslip (A).

Small-deflection cantilever bending was done with the Triboindenter, resulting in load-depth curves from which the maximum depth and load could be extracted. The position of the indenter tip relative to the base of the beam was recorded during the process. These variables could then all be utilized in Equation 2.5 to determine the elastic modulus, E .

Large-deflection cantilever bending was done by weighing out masses of dental wax, dividing each one in two, and sandwiching the free end of the fiber between the masses. The steel base was then elevated and placed in front of a grid of known size (Figure 3.5). A picture was taken and the mass noted. This was repeated for different masses and distances along the fiber.

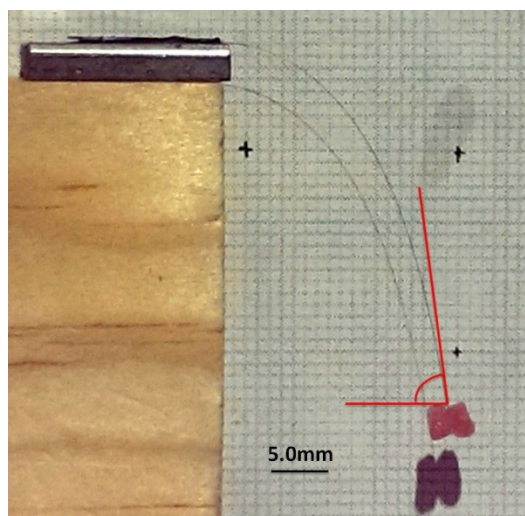


Figure 3.5: An example of a fiber with dental wax attached to the free end. The dental wax is clearly sandwiched around the fiber; there was no torsion of the fiber observed.

The image was digitized using WebPlot Digitizer [120]; Microsoft Excel was used to determine the angle of the fiber at the mass. Guessed values of the elastic modulus were input into Excel until a model curve matched with the real curves obtained via the digitization process.

3.3 Raman

A Renishaw inVia™ Raman microscope with Wire 3.4 was used throughout the entirety of this work. Three laser wavelengths are available with this setup: 514nm, 633nm, and 785nm. All may be turned on the same time and simply chosen through the program itself. Three magnifications are available: 5x, 20x, and 50x. These are selected by manually changing the objective lens and setting the software to the chosen objective. The laser(s) that were used during the experiment were consistently turned on at least an hour before actual testing began to allow sufficient time to come to a steady-state operating power (warming up). The laser(s) used was then focused on a piece of polished

single crystal silicon; the laser spot was moved via “manual beamsteer” to the center of the crosshairs. A single scan from 100-1100 cm^{-1} was made on the silicon. This was analyzed with Wire 3.4 and any offset needed was applied to the peak location. The peak location of silicon was consistently set to 520.6 cm^{-1} .

Analysis of a spectrum was done by first removing the background noise and then selecting the ‘Curve Fit’ option. Each peak of interest was selected and the fitting procedure begun. Once this was done, the resulting fitted curves were visually examined to see if they made sense; occasionally a curve would fit poorly and the process repeated. An example of well fitted curves and the data obtained is shown in Figure 3.6. The fit can be saved and applied to maps that have been made.

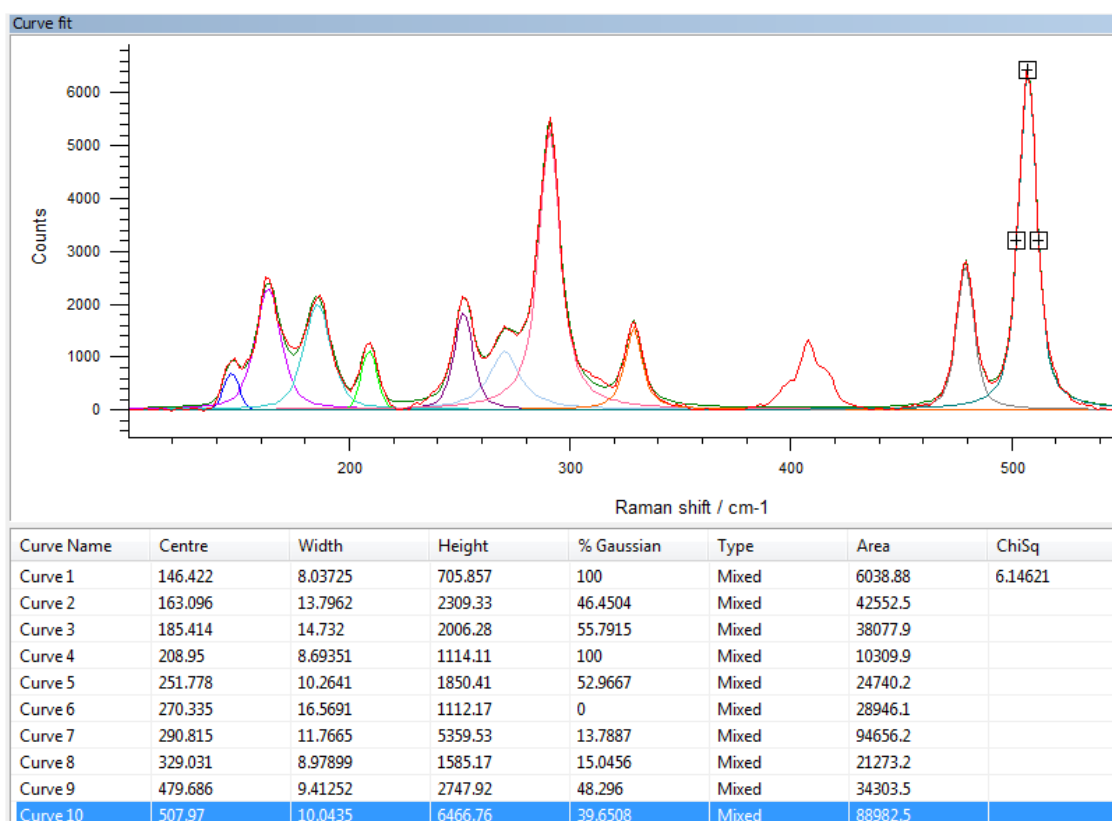


Figure 3.6: An example of 10 peaks that have been fitted with Wire 4.2 software.

Maps can be made over the surface of a sample – a Raman spectrum can be taken every 0.1 microns, although the spot size is significantly larger than this. Once a map has been made, it can be analyzed using the fitted curve from above. From the fitted map, specific maps may be made. These must be of a single peak, but may be the peak width, height, position, etc. So, the peak position of multiple peaks may be obtained from a single map and utilized to determine if there is residual stress in a material.

3.4 Fractography

For investigation of the fracture mechanics of the silicon carbide fibers in question, no loads were applied that would cause creep or plastic deformation. The exception is nanoindentation on the material, as discussed above. During nanoindentation plastic flow of the carbon-rich amorphous silicon on the outside layer of the fiber was observed. The methods in which the fibers were fractured for examination of the fracture faces, however, were not broken in such a way so as to induce plastic flow, being broken in tension or bending. For analysis of fracture faces, fibers were carefully placed on a piece of carbon tape; the tape then had the backing removed and was folded, the fibers being on the tensile side of the bend that was formed. The tape was able to bend sufficiently to fracture the fibers and in some cases, retain both resulting fracture faces. Several fibers were received from Free Form Fibers LLC that had been fractured as the result of tensile testing; these were also examined. A helium-ion microscope was used to perform most of the imaging.

4 Mechanical characterization of silicon carbide fibers grown by laser-induced CVD

The following paper is based on work in collaboration with Free Form Fibers, LLC.

Shawn Ward¹, Adrian Mann¹, Shay Harrison²

¹Department of Materials Science and Engineering, Rutgers University, New Brunswick, New Jersey 08854

²Free Form Fibers LLC, Saratoga Springs, New York 12866

Funding information

National Science Foundation, Grant No. IIP 1540027

Abstract

The mechanical properties of silicon carbide fibers are difficult to quantify, especially as their diameter is reduced. Using a number of different methods SiC fibers made by laser-induced chemical vapor deposition were characterized on the nano- and meso- length scales. Nanoindentation of the outer layer of the fibers confirmed a change in properties relative to the inner core. Creation of a glass matrix-fiber ceramic-matrix-composite reduced nanoindentation compliance issues found when fibers were mounted by other methods. Fibers were also mounted as cantilever beams and tested both within the linear-elastic deflection regime and the non-linear elastic deflection regime. The non-linear elastic deflection was examined with multiple methods to obtain average values of the

elastic modulus. The results from these varied methods generally agree well with each other, the overall elastic modulus of high quality fibers being 300 GPa with the core's elastic modulus being 330 GPa. Nanoindentation showed the core's hardness to be 36 GPa with the outer regions being around 20 GPa.

1 | INTRODUCTION

The properties of silicon carbide fibers offer attractive benefits when used in ceramic matrix composites (CMCs) and metal composites, especially in the aerospace and nuclear energy industries¹⁻⁴. The relatively high strength and high temperature resistance (>1400 °C) of silicon carbide are the most important properties⁵. The high strength of the fibers can offer improved fracture resistance in a CMC by bridging gaps and increasing the crack tortuosity^{6,7}. This is especially advantageous when a CMC is machined as this process causes residual stress at both the surface and the interior of the part, which increases the risk of fracture⁸. The quest to obtain a low-cost and effective method of producing such fibers is ongoing, as is the development of mechanical test methods for such fibers.

SiC fibers can be grown by laser-induced chemical vapor deposition (L-CVD) and this process is used by Free Form Fibers, LLC. In this production method, a laser is focused on a particular spot in the reaction chamber, inducing the precursor gases to form a plasma; the solid product resulting from the chemical reaction of the heated gas precursors then deposits on a surface and the surface is moved away from the deposition

region at the same rate as the deposition, creating a continuous fiber⁹. Conventional SiC fiber growth utilizes organometallic processing^{10,11} or silicon and carbon vapor deposition on a carbon fiber or other core¹²⁻¹⁴. Such fibers include the commercial products Tyranno SA™, Sylramic™, Hi Nicalon™, SCS-6, and Sigma SM1140+. Characterization of the mechanical properties of ceramic fibers is often carried out on bundles, or tows, of fibers^{6,14-16} rather than individual fibers; the current study focused on developing methods of testing the mechanical properties of individual L-CVD fibers.

2 | EXPERIMENTAL

2.1 | Materials

The fibers being examined are silicon rich (overall Si:C ratio of 71:29), typically 40 μm in diameter and 5-40 cm in length. Fibers were cleaved with a hardened steel wedge to obtain the desired lengths. An adhesive-backed paper was occasionally used to hold the fiber down while lengths were cleaved off the end of it, allowing for the user to prevent the sample from flying off during the cleaving process. Individual fibers, rather than tows were examined. The samples were cleaned with acetone and then ethanol before every experiment and no extra coating was applied to the surface of the samples. A tensile strength test method has previously been used to examine the fibers and this is under review as an ASTM standard, thus, it is not discussed here¹⁷.

2.2 | Nanoindentation

Nanoindentation was performed with a TriboIndenter™ (Hysitron Inc., Minneapolis, MN) with a Berkovich tip (Micro Star Technologies, Huntsville, TX). Fibers were indented with various loads, loading rates, and orientation. Analysis of the curves was performed with the widely used “Oliver-Pharr” method, where the reduced elastic modulus is calculated from the slope of the top of the unloading curve and hardness is calculated from the depth of the indent^{18,19}. The reduced elastic modulus is calculated as:

$$E_r = S \cdot \left(\frac{4 \cdot A}{\pi} \right)^{-0.5} \quad (1)$$

where E_r is the reduced elastic modulus (which takes into account the elastic modulus and Poisson’s ratio of both the sample and of the indenter tip), S is the slope of the top of the unloading curve, and A is the area of the indenter in contact with the sample. A is determined by calibrating the shape of the tip with a fused silica standard, a procedure known as the tip area function calibration. This accounts for deviation from the ideal tip shape due to blunting of the tip with use. Hardness is calculated as:

$$H = \frac{P_{max}}{A} \quad (2)$$

where H is the hardness, P_{max} is the maximum load, and A is the contact area on the sample under the indenter tip at maximum load, calculated as before for the reduced elastic modulus. Compliance of the machine is taken care of automatically, but compliance of the sample, adhesion (if any), and substrate effects (if any) are not accounted for by the analysis software.

Steel pucks were polished to 600 grit ($\approx 30 \mu\text{m}$ particle size) and then a drop of cyanoacrylate super glue was delivered to the surface. Excess adhesive was scraped off

with another piece of steel and then sample fibers were placed onto the surface. The fibers were lightly pressed down on with tweezers, care being taken not to damage the regions that were to be tested and not to roll the fibers. The glue was then allowed to cure for 24 hours before indentation began (Figure 4.1).

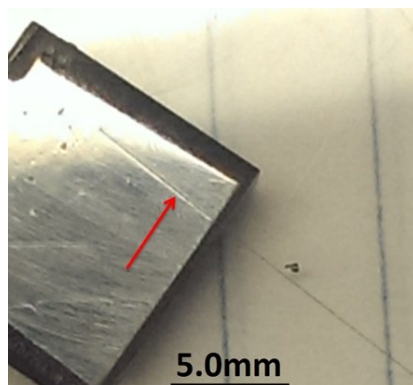


Figure 4.1: The arrow points at a single fiber adhered to the steel puck.

Two methods were used for mounting the fibers vertically (parallel to their long axis) for indentation of the cross-section: adhering the fibers to the inside of a 0.5 mm inside diameter glass tube (to maintain a constant orientation); sintering the fibers in a glass ceramic. Mounting fibers in a glass tube (Figure 4.2) was achieved by simply laying the tube in the valley of a folded piece of paper, carefully placing fibers inside the tube, and then applying a drop of cyanoacrylate adhesive to one end of the tube. The adhesive was brought into the tube by capillary action; repeat applications of adhesive were made until the tube was filled with adhesive. The tube was then mounted in a cold-set epoxy for handling and polishing purposes. Mounting the fibers in a glass ceramic was similarly simple in concept; several fibers were placed on a glass ceramic powder with a larger piece of silicon (to provide the ability to find the orientation of the fibers after sintering). After pressing and sintering, the ceramic disk was cut perpendicular to the fiber orientation and mounted in cold-set epoxy for handling and polishing purposes.

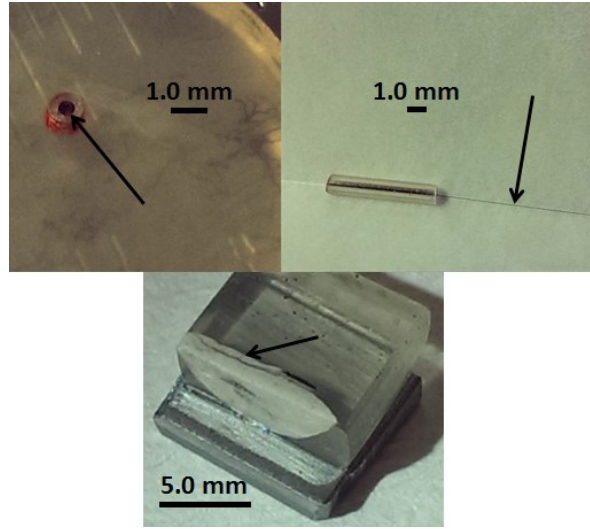


Figure 4.2: An example of a fiber set in a glass tube (top right) before the adhesive was applied. The glass tube mounted upright in a cold-set epoxy is shown on the top left. The sintered glass puck was mounted in cold-set epoxy and then attached to a piece of steel (bottom). Arrows in each part show the location of the fiber(s).

2.3 | Cantilever bending

Cantilever bending is a very old concept, the principles of which are very well known.

The fundamental equation describing a fixed-free cantilever beam is:

$$\frac{M}{EI} = \frac{d^2y}{dx^2} \quad (3)$$

where M is the bending moment, EI is the combined elastic modulus and moment of inertia, and the second derivative of y with respect to x gives the shape of the deflected beam^{20,21}. The moment of inertia for a round beam is:

$$I = r^4 \cdot \frac{\pi}{4} \quad (4)$$

where r is the radius of the beam^{20,21}. The two categories of deflection are linear elastic and non-linear elastic. Linear elasticity makes the assumption that the deflection of the

free end is small so the sine of the angle of deflection is approximately the same as the angle of deflection (φ). In non-linear elasticity, the angle of deflection, φ , is great enough that $\sin(\varphi)$ is not approximately φ . This second category is referred to as large-deflection cantilever bending in this work.

2.3.1 | Nanocantilever

Fibers were adhered to a steel plate with 6-12 mm of fiber extending from the plate, with a plastic coverslip placed on top to prevent the fiber from deflecting in the clamp. Figure 4.3 shows an example of a fiber extending from the steel plate. The TriboIndenter™ was then used to deflect the beam at a known distance from the clamped end. The resulting maximum load and displacement are used in conjunction with the distance from the clamp to determine EI . Equation 3 can be solved and written to reflect the values that are known and unknown in the case of a fiber of unknown elastic modulus:

$$EI = \frac{F \cdot L^3}{3 \cdot h} \quad (5)$$

where F is the measured force, L is the length of the beam, and h is the displacement of the indenter tip. This new equation allows for the determination of the combined variable EI , from which E is easily calculable knowing the moment of inertia as given by Equation 4.

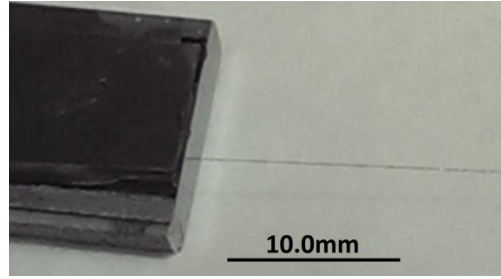


Figure 4.3: A fiber mounted for cantilever testing is shown. The plastic coverslip acts as a clamp on the fiber, preventing it from lifting off the metal substrate.

The Triboindenter was configured to have an open-loop load function (no feedback) for testing, starting with a 600 μN load and increasing with proximity to the clamp. For the instrument this particular load function is used for performing an air indent calibration with a displacement of 4 μm , which is close to the maximum displacement the transducer can produce. When this load function is used to push on a fiber the resulting discrepancy in force between the air indent and one with the fiber can be utilized as a measure of the force, P_{real} , necessary to deflect the fiber (Equation 6). The displacement is an independently measured variable within the transducer.

$$P_{real} = P_{indent} - P_{air}(max) \quad (6)$$

2.3.2 | Large-deflection cantilever

A single fiber was mounted in the same manner as for the nano-cantilever bend testing, but with a length between 6 mm and 70 mm. This length allows the fiber to bend through a large angle, increasing the measurability of the deflection and decreasing the error in position measurement. Masses made of dental wax were weighed out; dental wax was

chosen due to its ability to be easily applied and removed from the fiber. Figure 4.4 shows an example of a mass attached to a straight fiber.

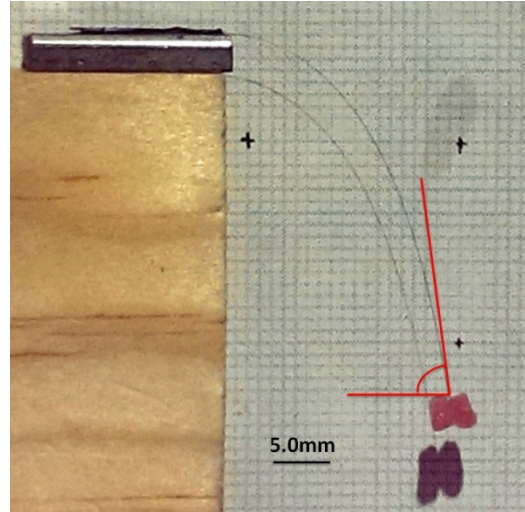


Figure 4.4: Wax masses were cut in half and adhered to the free end of the fiber symmetrically. The backdrop is a grid with 1mm spacing. The red lines indicate the angle φ_0 .

The images were processed utilizing WebPlotDigitizer²². This program allows individual x,y points to be placed on an image, resulting in a text file that gives the x - and y - positions for many points along the fiber.

Belendez et al²³ and Bisshopp et al²⁴ independently derived a method of examining the large deflection of cantilever beams. This method gives the equations of position for individual points along a fiber undergoing large deflection. The variables considered in this method include: the mass at the end of the fiber, the moment of inertia (I), the elastic modulus (E), and the angle of deflection at the end of the fiber where the mass is located (φ_0). The full derivations to the equations shown below are in the work of

Belendez et al²³, the results of which are used here; a less complete derivation of the equations and their use is presented in the work of Bisshopp et al²⁴.

The equations used for the large-deflection method to determine the x - and y -position of a point on the bent beam are:

$$x = \left(\sqrt{2 \cdot \frac{EI}{F}} \right) \cdot (\sqrt{\sin(\varphi_0)} - \sqrt{\sin(\varphi_0) - \sin(\varphi)}) \quad (7)$$

$$y = \sqrt{\left(\frac{EI}{F}\right)/2} \cdot \int_0^{\varphi_0} \frac{\sin(\varphi)}{\sqrt{\sin(\varphi_0) - \sin(\varphi)}} d\varphi \quad (8)$$

$$\int_0^{\varphi_0} \frac{\sin(\varphi)}{\sqrt{\sin(\varphi_0) - \sin(\varphi)}} d\varphi = q \quad (9)$$

where EI is the elastic modulus times the moment of inertia of a rod, φ_0 is the angle of the fiber at the mass, and φ is the angle of the fiber at any point relative to the base ($x=0$, $y=0$). The integral in Equation 8 is elliptical and it was set as variable, q (Equation 9), and solved numerically via MATLAB.

The resultant x - and y -values are then plotted against the experimental results utilizing a guessed EI . The value EI is iteratively found by varying it until the model curves match the experimental curves.

This method is carried out for different lengths and masses, giving an improved accuracy of the deduced elastic modulus. Once a fiber is long enough for the free end to be asymptotically vertical, a second method of analysis is also possible as well that was developed by Scott and Robbins²⁵. Scott and Robbins attached equal masses to two ends

of a long fiber and hung the fiber over a small rod. They derived a relationship utilizing the mass and the x -distance between the vertical arms of the fiber, and found the following equation that can be used determine EI :

$$\frac{T}{EI} = \frac{8}{D^2} \quad (10)$$

where T is the tensile force applied by the mass which is simply the mass times gravity, and D is the x -distance between the two vertical arms of the hanging fiber. This can be rewritten for a cantilever beam of sufficient length as:

$$(9.81 \cdot m) \cdot \left(\frac{(2 \cdot x_{mass})^2}{8}\right) = EI \quad (11)$$

where m is the mass of the wax in kilograms and x_{mass} is the x -position of the mass from the base of the cantilever in meters.

3 | RESULTS

3.1 | Nanoindentation on the outside surface

Data taken across a variety of loads and load rates on samples adhered to a steel puck show consistency in both reduced elastic modulus and hardness. The reduced elastic modulus was affected more by how well the fiber was adhered than hardness. This is because any deflection of the fiber into the adhesive will alter the unloading slope and depth, on which reduced elastic modulus depends, whereas the hardness is only affected by depth (Figure 4.5). Subsequent imaging of indents on the outside of the fiber show plastic flow in the material (Figure 4.6).

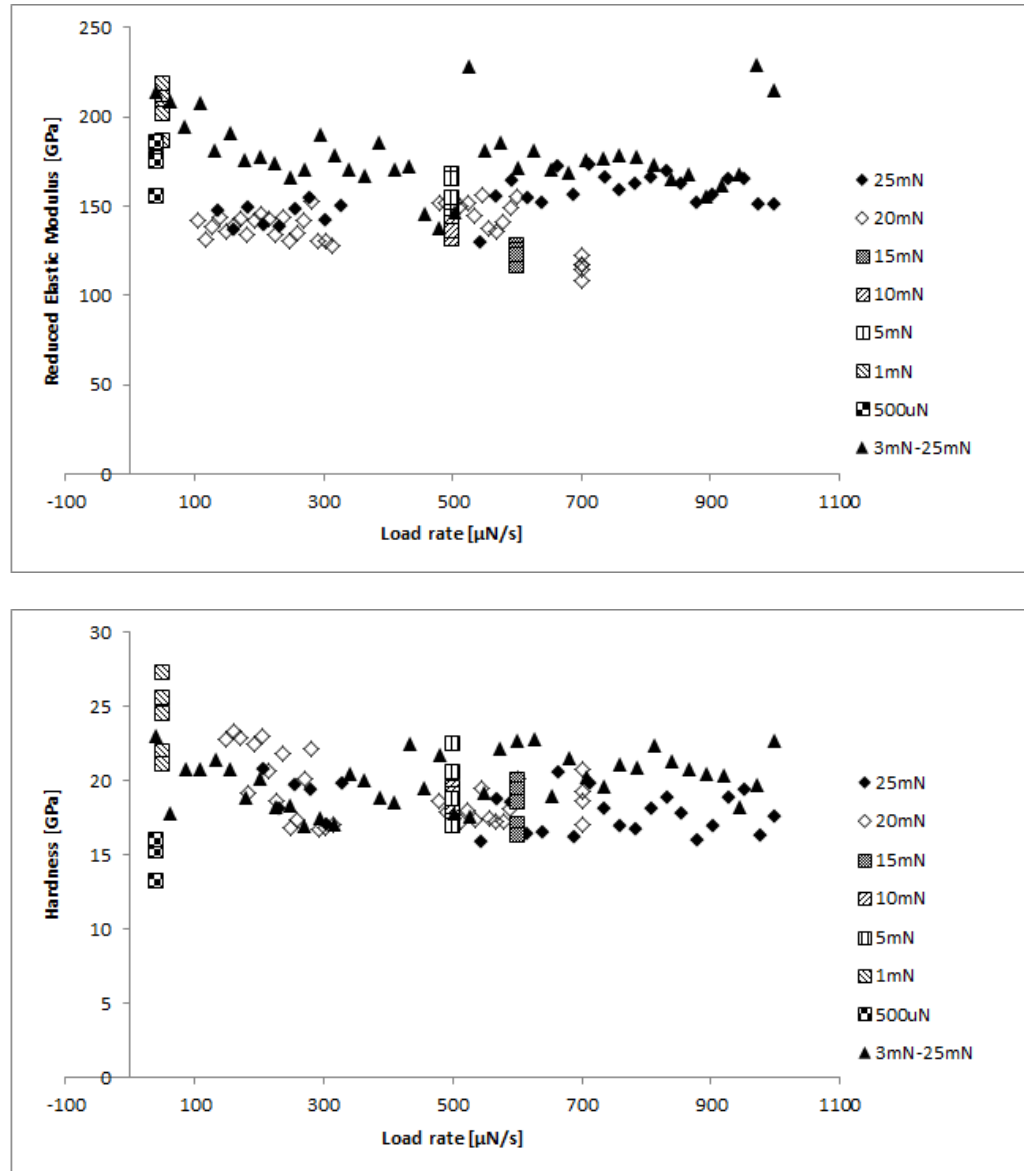


Figure 4.5: Indents performed on the outside of the fiber at a range of load rates and loads show consistent reduced elastic modulus and hardness. Each symbol represents the peak load chosen for the load function.

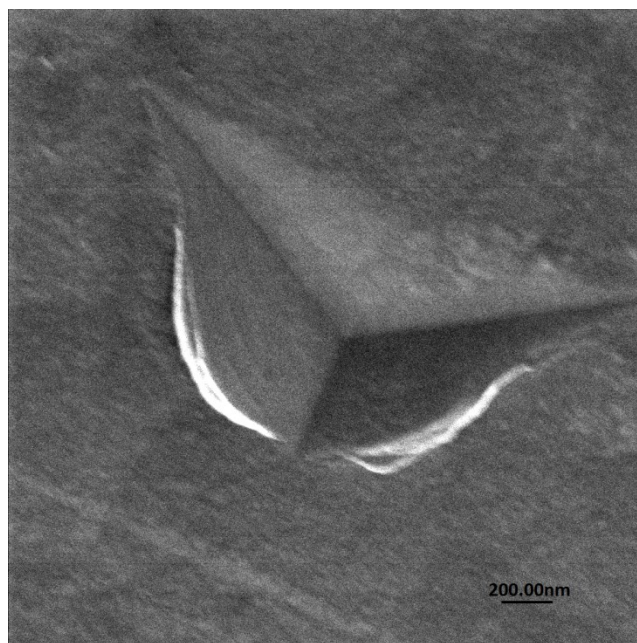


Figure 4.6: Pile-up or extrusion is visible on the lower two edges of the indent. The load applied was 25mN. The image was taken with a helium-ion microscope, HIM (Orion, Zeiss, Germany).

The amorphous nature of the outside of the fiber allows the carbon-rich silicon to flow under pressure (Figure 4.6), similar to the pressure-induced phase transformation of crystalline silicon²⁶. The maximum depth under the 25mN load was 260nm; most indents performed had depths much lower than this.

3.2 | Cross-sectional indentation

It was found that no matter the exact technique used, the polymer/adhesive mounting methods share the same common flaw once the fibers have been mounted: that in the process of polishing the fibers there is preferential removal of the adhesive used to mount the fiber, leaving the fiber to be more exposed than the surrounding area (shown schematically by Figure 4.7). In addition, the adhesive is quite compliant in shear,

resulting in unusable load-depth curves for some nanoindents. These issues are mitigated by utilizing a sintered glass pellet with a fiber embedded in it; the helium-ion microscope (HIM) image shows a smooth interface on the well-bonded side of the fiber as shown by Figure 4.8.

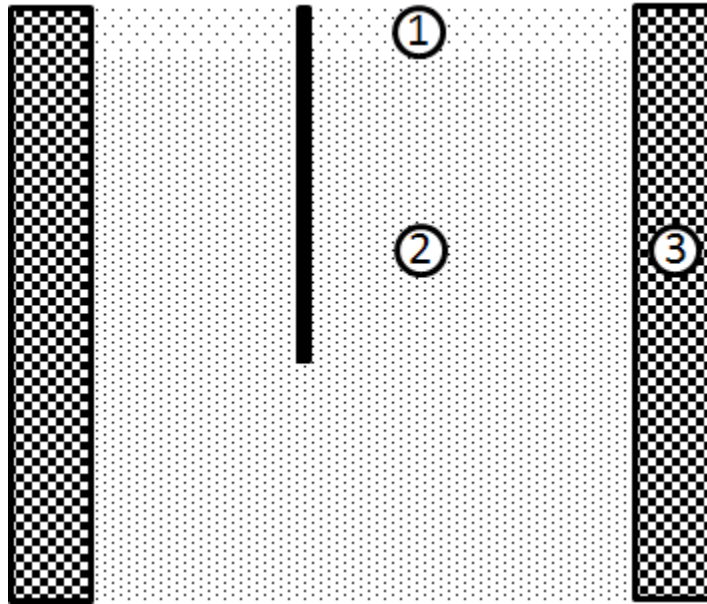


Figure 4.7: Schematic showing a fiber as the black rod, the close dots as adhesive (2), the further-spaced dots (1) as adhesive that was removed during polishing, and the checkered “walls” (3) as the glass tube in which the fiber was mounted (image not to scale). As well as standing above the mounting adhesive, the fiber can elastically shear at the adhesive interface under the vertical force of the indenter.

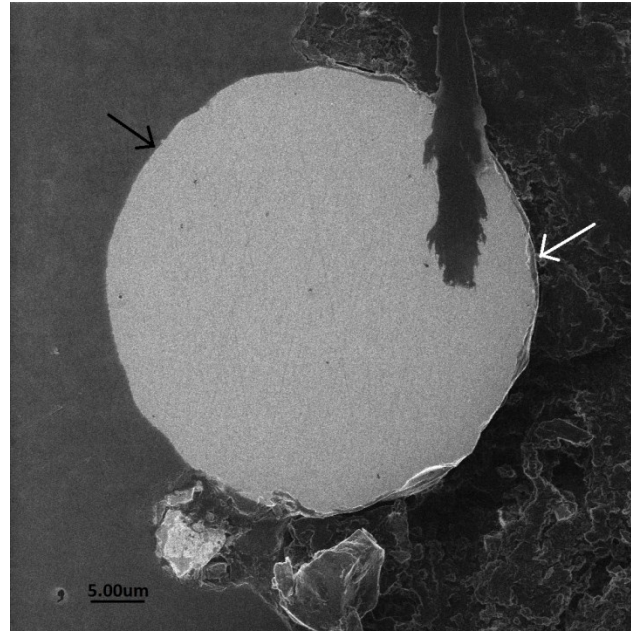


Figure 4.8: A Helium-Ion Microscope image of the fiber embedded in sintered glass shows good bonding on one half of the fiber and poor bonding on the other half. Arrows indicate the location of good (black) and poor (white) bonding with the sintered glass. The left half was examined with a grid pattern of indents.

Indenting fibers mounted in sintered glass rather than polymer/adhesive resulted in more consistent load-depth curves. A clear relationship between the mechanical properties and position within the fiber was evident. This is shown by maps of the cross-section of a fiber mounted in sintered glass and polished with a 1 μm diamond lapping pad (see Figure 4.9).

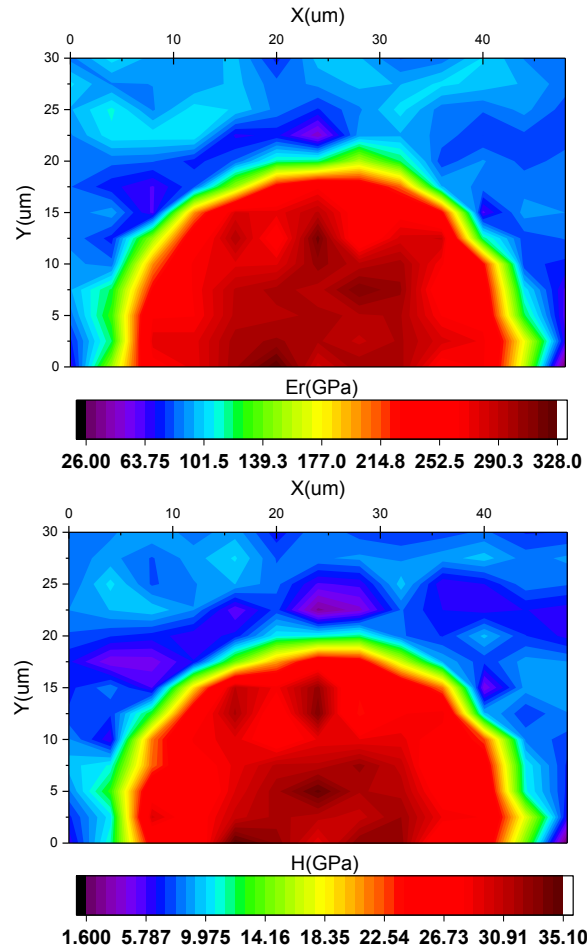


Figure 4.9: A map over the cross-section of a fiber embedded in sintered glass shows generally higher reduced elastic modulus and hardness near the center of the fiber, decreasing slightly with radial distance. Indents were performed 3 microns apart with a maximum load of 4mN.

Peak values of 330 GPa and 36 GPa, respectively, for the reduced elastic modulus and hardness are seen, and these large values are spread out across the center of the sample. As the radial distance increases, the reduced elastic modulus and hardness drop off slowly until the external layer of carbon-rich amorphous silicon is reached. The values obtained in this region match reasonably well to the values obtained via nanoindentation of the outside of the fiber.

3.3 | Cantilever

The nanocantilever and large-deflection cantilever results are considered together as each can be plotted with respect to the beam length. Any individual fiber had a constant diameter; however, across a batch and between batches, the diameter varies. Typical diameters varied between 36 μm and 46 μm . This was reflected in the moment of inertia calculations and was typically the largest source of error.

An example of the process to obtain a model curve via the large deflection method is shown in Figure 4.10. The results of two different attached dental wax masses (loads) are shown; one being 196 μN and the other 504 μN . The steel to which the fiber is attached was flipped upside down from (a) to (b) to verify the mass was not loaded off-center. This was repeated for multiple masses at different lengths for each fiber.

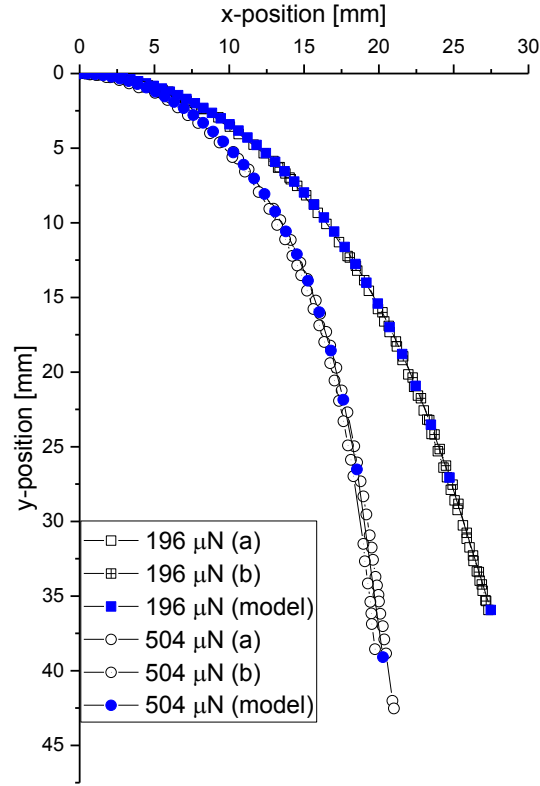


Figure 4.10: The model curves (filled points) line up well with the real curves (open points). As discussed in the main text, EI was guessed and iterated until the model curve fell on top of the real curves.

The results for several experiments of both the nanocantilever and large deflection kind are shown in Figure 4.11. Within the large deflection techniques, the calculated elastic modulus is consistent for any given fiber.

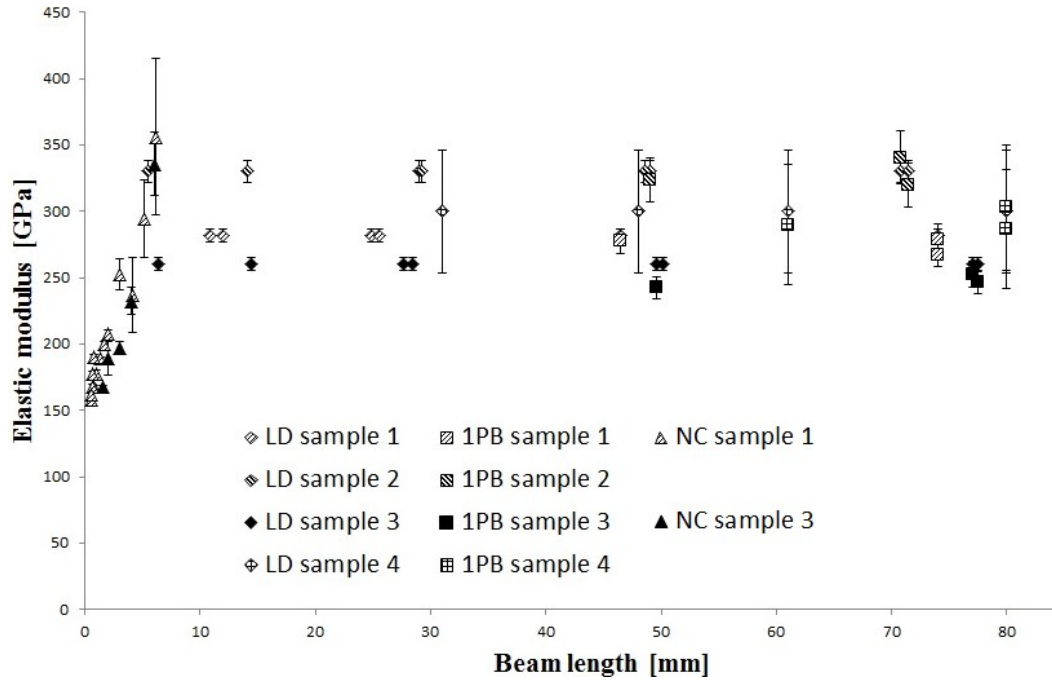


Figure 4.11: Multiple techniques and fibers are presented above. The large deflection (LD) method is represented by the diamonds, one-point bend (1PB) analysis by squares, and nanocantilever (NC) results by triangles. Different samples are denoted by different patterns chosen to represent them.

The calculated elastic modulus is in close agreement between the large-deflection analysis and the hanging fiber analysis methods, the average discrepancy being 14 GPa. The nanocantilever data increases in elastic modulus from 150 GPa to 350 GPa with increasing distance from the clamp. There is little error in the measurement of the length L ($\pm 10 \mu\text{m}$) which has the second largest impact on elastic modulus after the diameter of the fiber. The displacement and force are both accurately measured by the machine; however, the boundary conditions at the clamp ($\varphi=0$, $\Delta y=0$) may not be ideal, resulting in the error seen above. The closer the tip is to the clamp, the more the fiber may deflect into the substrate, where even several hundred nanometers of displacement will drastically alter the determined elastic modulus. A method of decoupling the displacement into the adhesive from the bending of the fiber is not available at this time.

Displacement into the adhesive effectively changes the length, making it greater than the measureable length. As the calculated elastic modulus is dependent on L^3 , if the effective length is only +5% greater than the measured length, the calculated modulus will be decreased by 13.6%.

The results of the large deflection method show this method to be highly repeatable. The primary source of error in the large deflection methods is the measurement of the diameter of the fibers. Using electron microscopy to more accurately measure the fiber diameter reduces this error to $\pm 0.1 \mu\text{m}$, compared to the $\pm 1 \mu\text{m}$ obtained using micrometers. With an accurate diameter, the error in calculation of the elastic modulus is less than 3%.

4 | CONCLUSIONS

Combining nanoindentation with cantilever beam measurements has provided a spectrum of length scales to probe with the fibers in question. Nanoindentation shows that on the very small scale, the cross-section of the fibers has a reduced elastic modulus of 270 ± 31 GPa with peak values of 330 GPa while the outer, amorphous layer has a reduced elastic modulus of 158 ± 20 GPa. The hardness likewise differed, the cross-section holding a hardness of 28 ± 4 GPa with peak values of 36 GPa while the outer layer has a hardness of 20 ± 3 GPa. The values observed within the core of these fibers closely compare with other SiC fibers such as SCS-6²⁷ and Sylramic²⁸. Indentation of the outer amorphous layer reached a maximum depth of 260 nm; depending on the exact fiber examined, there

may have been substrate effects from the crystalline SiC, as this depth is greater than 1/10th the thickness of the amorphous layer. Indents to lower loads however still exhibit high values of reduced modulus and hardness, indicating that the stiff core did not significantly impact the results of indentation on the outside of the fiber. The outer amorphous layer exhibits plastic flow at the edge of the indenter tip contact. This ductility may act as a toughening mechanism during actual use of the fibers. Mounting the fibers using a non-reactive ceramic-matrix composite (CMC) of sintered glass around a fiber resulted in more consistent nanoindentation results than could be obtained by mounting the fiber in a polymer.

Successful large-deflection cantilever bend tests were performed on a variety of fibers. These tests allow for the determination of the average elastic modulus of the fibers over their length and diameter. Results vary by batch, with the best fibers exhibiting an elastic modulus of 300 ± 8 GPa via the Belendez et al²³ and Bisshopp et al²⁴ methods of analysis and 330 ± 14 GPa via the Scott and Robbins²⁵ method. Use of instrumented indentation to perform cantilever testing on such large fibers proved to be inconsistent, with a significant change in calculated elastic modulus with proximity to the clamp. Likely reasons for this method failing are that unlike in other nanocantilever tests^{29,30}, the beam is not a continuous part of the substrate, implying that the assumed boundary conditions are not valid at this scale (that the beam is rigidly clamped and there is no deflection of the beam into the substrate).

Further investigation into the properties of the fibers, such as examining residual stresses from the processing⁸ and induced stresses from forming a CMC³¹ would be very interesting. Additionally, in-situ tests of micro-Raman and instrumented indentation³² may give insight into the mechanics and processes going on when the outside of the fiber is indented and plastic flow of the carbon-rich amorphous silicon is observed.

ACKNOWLEDGEMENTS

The author would like to thank Mengjun Li and Dr. Slava Manichev of the Rutgers Physics department for their help with imaging with the helium ion microscope, especially on the insulating substrates. The author would also like to thank the NSF support for the Ceramic, Composite, and Optical Materials Center (CCOMC). This material is based upon work supported by the National Science Foundation under Grant No. IIP 1540027.

References

- [1] Morscher GN. Advanced woven SiC/SiC Composites for High Temperature Applications. NASA Technical Reports Server, Cleveland, OH, 2007.
- [2] Yajima S, Hayashi J, Omori M, Okamura K. Development of a silicon carbide fibre with high tensile strength. *Nature* 1976; 261:683-685.
- [3] Uesaka Y. Business: SiC fibers see increasing use in high-temperature applications. *Nikkei Asian Review* [Online]; 2017 [cited 2018 May 25]. Available: <https://asia.nikkei.com/Tech-Science/Tech/SiC-fibers-see-increasing-use-in-high-temperature-applications>.
- [4] Katoh Y, Wilson DF, Forsberg CW. Assessment of Silicon Carbide Composites for Advanced Salt-Cooled Reactors. Oak Ridge National Laboratory, Oak Ridge, TN, 2007.
- [5] Bunsell AR, Piant A. A review of the development of three generations of small diameter silicon carbide fibres. *J. Mat. Sci.* 2006;41:823-839.

- [6] Hinoki T, Lara-Curzio E, Snead LL. Mechanical Properties of high purity SiC fiber-reinforced CVI-SiC matrix composites. *Fusion Sci. Tech.* 2003;44
- [7] Jones CR, Henajer CHJ, Jones RH. Crack bridging by SiC fibers during slow crack growth and the resultant fracture toughness of SiC/SiCf composites. *Scripta Metall Mater* 1995;33(12):2067-2072.
- [8] Groth BP, Langan SM, Haber RA, Mann AB. Relating residual stresses to machining and finishing in silicon carbide. *Ceramics Int.* 2016;42:799-807.
- [9] Free Form Fibers, LLC. Process [Online]; 2018 [cited 2018 May 10] Available: <https://fffibers.com/process/>.
- [10] Idesaki A, M. Narisawa M, Okamura K, et al. Fine SiC fiber synthesized from organosilicon polymers: relationship between spinning temperature and melt viscosity of precursor polymers. *J. Mat. Sci.* 2001;36(23):5565-5569.
- [11] Yajima S, Okamura K, Hayashi J, Omori M. Synthesis of continuous SiC fibers with high tensile strength. *J. Am. Ceram. Soc.* 1976;59(7-8):324-327.
- [12] Specialty Materials, Inc. SCS Silicon Carbide Fiber Technical Presentation. [Online]; 2018 [cited 2018 May 18] Available: <https://www.specmaterials.com/pdfs/SCSFibersTechnicalPresentation.pdf>.
- [13] Ward Y, Young R. A microstructural study of silicon carbide fibres through the use of Raman microscopy. *J. Mat. Sci.* 2001;36:55-66.
- [14] Garcia-Leiva MC, Ocana I, Martin-Meizoso A, Martinez-Esnaola JM. Fracture Mechanics of Sigma SM1140+ fibre. *Eng Fract Mech.* 2002;69:1007-1013.
- [15] Youngblood GE, Lewinsohn C, Jones RH, Kohyama A. Tensile strength and fracture surface characterization of Hi-Nicalon SiC fibers. *J. Nucl Mater.* 2001;289:1-9.
- [16] Leslie CJ, Boakye EE, Keller KA, Cinibulk MK. Development and Characterization of Continuous SiC Fiber-Reinforced HfB₂-Based UHTC Matrix Composites Using Polymer Impregnation and Slurry Infiltration Techniques. *Int J Appl Ceram Tec.* 2015;12(1):235-244.
- [17] Pegna J, Goduguchinta R, Harrison S. Tensile Test for High Modulus Monofilament Fiber, 2018.
- [18] Oliver WC, Pharr GM. An improved technique for determining the hardness and elastic modulus using load and displacement sensing indentation experiments. *J. Mater. Res.* 1992;7(6).
- [19] Hysitron Inc., Hysitron TriboIndenter Users Manual, Minneapolis, MN: Hysitron, 2001.
- [20] Clements GR, Wilson LT. Properties of Materials. In *Manual of Mathematics and Mechanics*. New York and London; McGraw-Hill Book Co. Inc.; 1937:257.
- [21] Avallone EA, Baumeister T. Mechanics of Materials. In *Mark's Standard Handbook for Mechanical Engineers*, Tenth Edition. New York; McGraw-Hill; 1976:5-22.
- [22] Rohatji A. WebPlotDigitizer - Web Based Plot Digitizer. [Online] 2010-2017 [cited 2018 May 05] Available: <https://automeris.io/WebPlotDigitizer>.
- [23] Belendez T, Neipp C, Belendez A. Large and small deflections of a cantilever beam. *Eur. J. Phys.* 2002;23(3):371-379.

- [24] Bisshopp KE, Drucker DC. Large deflection of cantilever beams. *Q Appl Math.* 1945;III(3):272-275.
- [25] Scott GV, Robbins CR. Stiffness of human hair fibers. *J. Soc. Cosmet. Chem.* 1978;28:469-485.
- [26] Juliano T, Gogotsi Y, Domnich V. Effect of indentation conditions on phase transformation induced events in silicon. *J Mater Res.* 2003;18(5):1192-1201.
- [27] Mann AB, Balooch M, Kinney JH, Weihs TP. Radial variations in modulus and hardness in SCS-6 silicon carbide fibers. *J Am Ceram Soc.* 1999;82(1):111-116.
- [28] Sola F, Bhatt R. Mapping the local modulus of Sylramic silicon carbide fibers by nanoindentation. *Mater Lett.* 2015;159:398-398.
- [29] Hsu C, Tsuo C, Fang W. Measuring thin film elastic modulus using a micromachined cantilever bending test by nanoindenter. *J Micro Nanolithogr MEMS MOEMS.* 2007;6(3).
- [30] Weihs TP, Hong S, Bravman JC, Nix WD. Mechanical deflection of cantilever microbeams: A new technique for testing the mechanical properties of thin films. *J Mater Res.* 1988;3(5):931-942.
- [31] Ward SH, Mann AB. Four-point bend apparatus for in situ micro-Raman stress measurements. *Meas Sci Tech.* 2018;29.
- [32] Jochum T, Reimanis IE. In situ Raman indentation of B-Eucryptite: Characterization of the pressure-induced phase transformation. *J Am Ceram Soc.* 2009;92(4):857-863.

5 Supporting work in characterization of said SiC fibers

Mechanical tests were not the only observations to be made on the fibers grown by Free Form Fibers. Fractographic analysis of broken fibers and Raman spectroscopy of the fibers were performed, providing additional insight into the mechanical and chemical properties of the fibers.

5.1 Fractography

Fractography of materials can be a very useful technique for determining how a part failed in the field and is essential during investigations of failures where lives were lost.

Of the imaged fibers that were broken in bending, about half show the mirror-mist-hackle feature and cantilever curl typical of ceramics broken in bending. Examples of these fibers are shown in Figure 5.1, Figure 5.2, and Figure 5.3. It should be noted that the outer carbon-rich amorphous silicon layer is visible in these images as a darker band going around the entire fiber. Figure 5.3 exhibits a change in fracture pattern where the crystalline SiC comes in contact with the a-Si. This will be investigated in further detail later in this chapter.

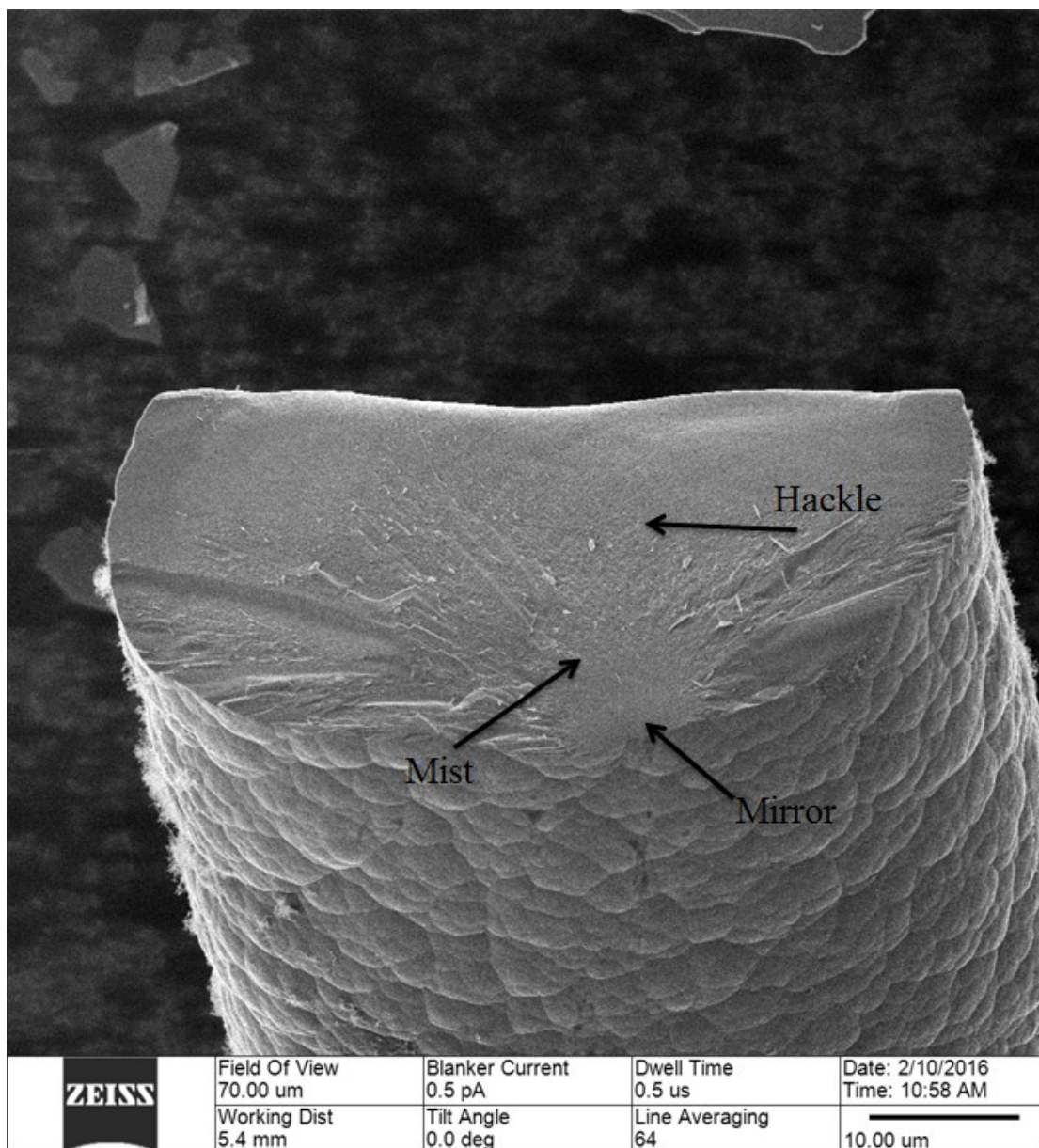


Figure 5.1: A very clear mirror, mist, and hackle region exist on this fiber. The origin of the fracture was near the bottom right and it propagated up from there.

The fiber shown in Figure 5.1 will be referenced later in this work as fiber-1.

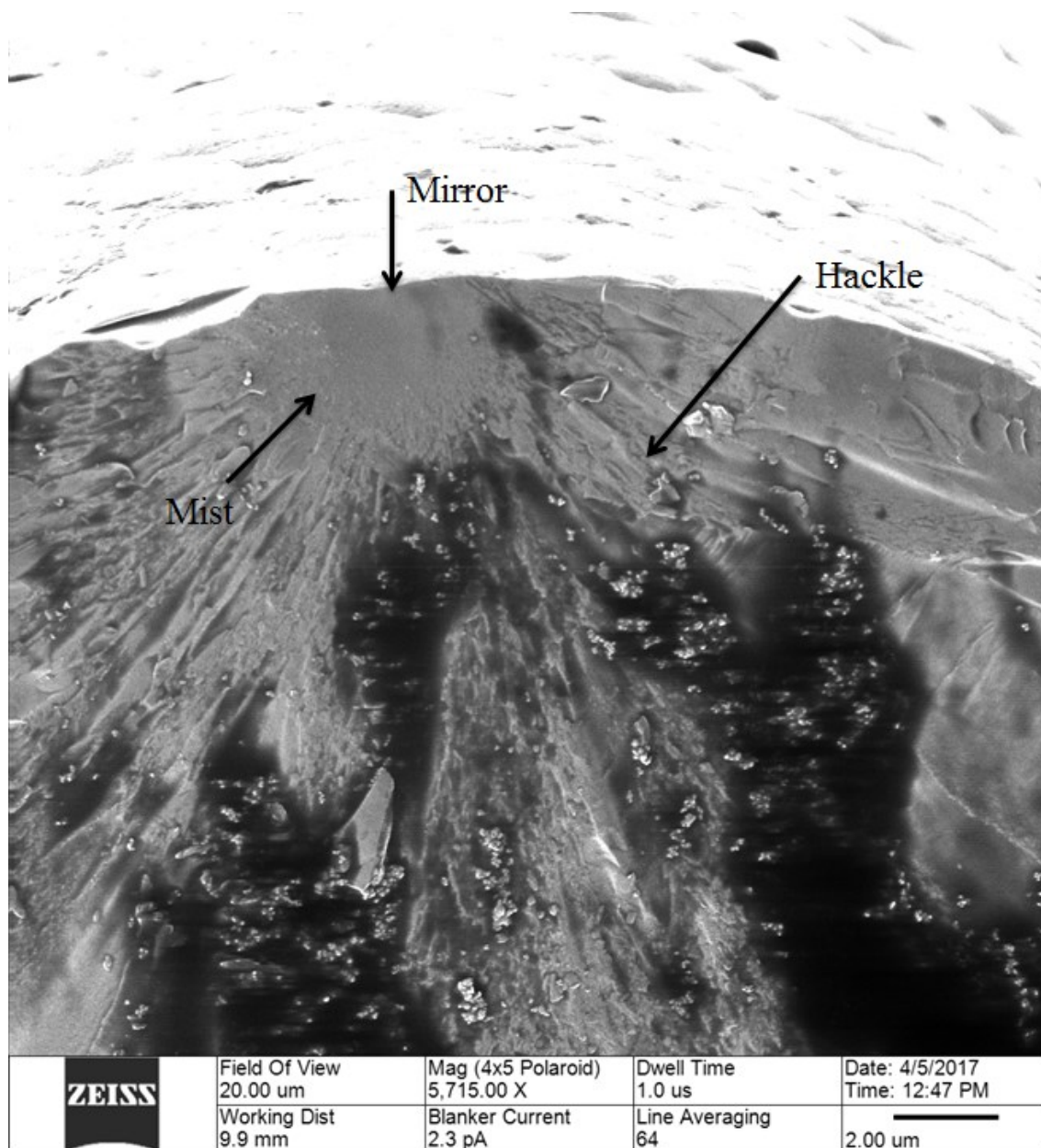


Figure 5.2: The mirror is visible at the top of this fiber; the fracture propagated down and out from that location with a small mist visible.

Dark spots are due to organic matter being on the fiber. As these were broken in air prior to being placed in the HIM, oils and particulates had the opportunity to adhere to the freshly broken surface.

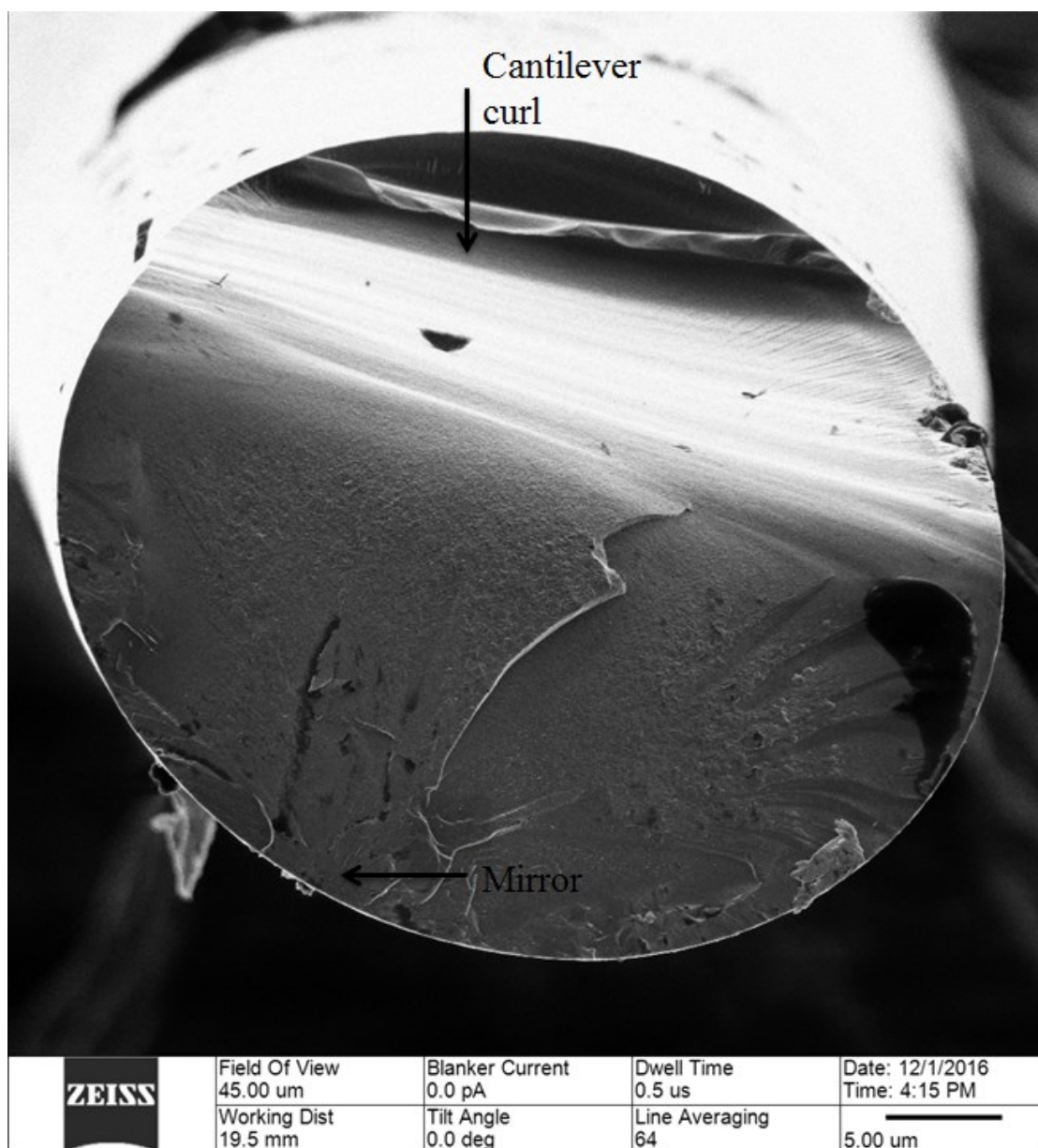


Figure 5.3: The cantilever curl typical of a brittle material broken in bending is clearly visible in this image. A very small mirror is visible on the lower left side; this is examined later.

Other fibers examined did not exhibit mirror-mist-hackle features, some exhibiting only a mirror or no clear initiation point (Figure 5.4 and Figure 5.5).

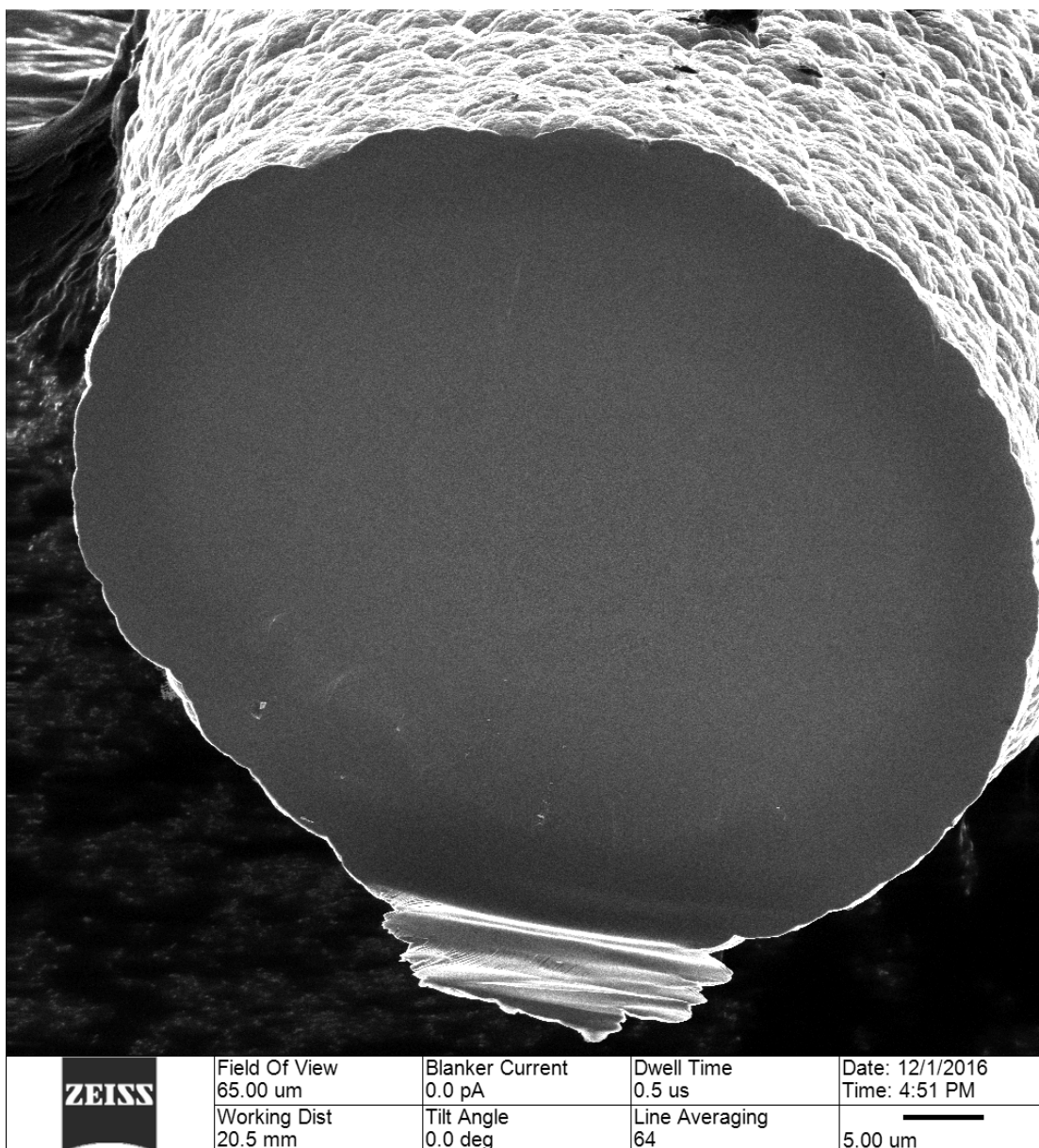


Figure 5.4: The entire surface except for the cantilever curl seen at the bottom is completely smooth – investigation with extremely high magnification with the HIM shows no surface variation.

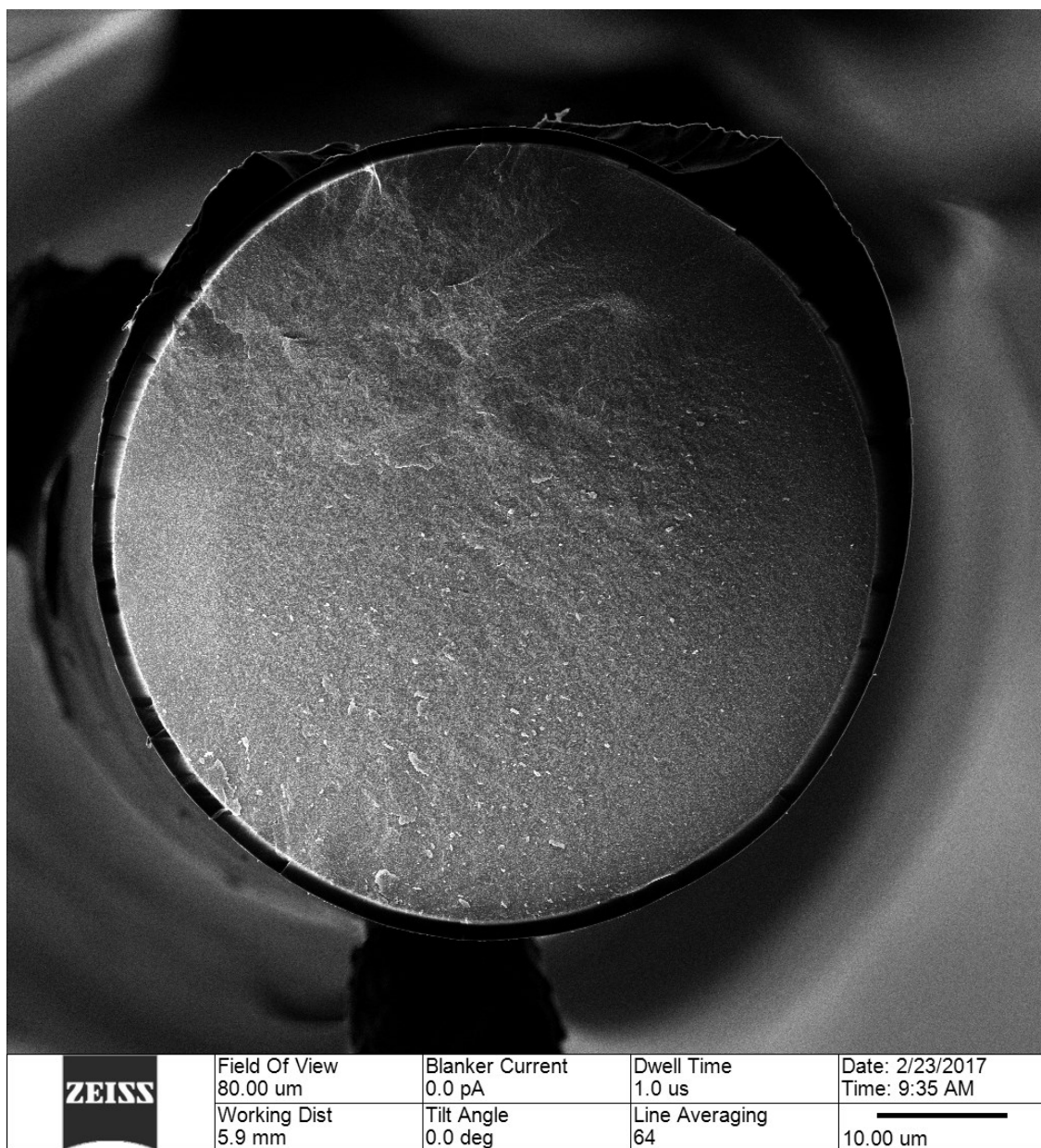


Figure 5.5: This fiber shows no clear initiation site nor fracture direction. It is also missing the tell-tale cantilever curl that indicates fracture in bending.

The lack of features, fracture direction, and initiation sites point to the possibility that these fracture faces are in fact from secondary fractures rather than primary fractures. This is indicative of a very hard material, as the primary fracture had to have enough energy to cause a spontaneous secondary fracture to occur either at the termination of the

shock wave from the first fracture or simultaneously as the shock wave traveled back [114]. Figure 5.4 may be a mirror that is nearly the size of the entire fiber, which would indicate that this particular point on this particular fiber was quite weak. This is unlikely considering the other available data, but cannot be dismissed. The actual primary fracture face is missing.

Since there is a mirror, mist, and hackle present in several fibers, it is possible to determine the approximate amount of stress the fiber was under when it failed. In order to do this, the mirror constant for the particular material in question must be known. The mirror constants for bulk sintered silicon carbide are 10.7-11.5 MPa $\sqrt{\text{m}}$ [121] [122] [123]. However, these are not necessarily the correct mirror constants as changing the process by which a material is made (and altering the chemical composition) will change how the material fractures, and thus the mirror constant. A more appropriate mirror constant for silicon carbide fibers can be found from experiments done to determine the mirror constants of Tyranno™ and Nicalon™; the mirror constants for these materials are 2-2.5 MPa $\sqrt{\text{m}}$ [124] [125] [126], 2.5 MPa $\sqrt{\text{m}}$ is used in this work. The equation that relates the size of the mirror to the fracture stress is

$$\sigma\sqrt{R} = A \quad (5.1)$$

where σ is the tensile stress at the origin at the time of fracture, R is the radius of the mirror, and A is the above mentioned mirror constant [114]. This equation can be readily rearranged to estimate the stress at the origin at the time of fracture

$$\sigma = \frac{A}{\sqrt{R}} \quad (5.2)$$

The average radius from multiple measurements at different orientations on a fiber can be used as R [114]. The following table provides the image, average radius, and estimated stress at the point of failure.

Table 5.1: The image number, brief description of the image, average radius of the mirror, the estimated stress at failure, and fiber diameter are provided. The description indicates the mode of failure and if the fiber is the same but with a different magnification or angle (simply same fiber).

Image	Description	R [μm]	σ [MPa]	Fiber diameter [μm]
1	Broken in bending	4.25	1213	58
2	Broken in bending	0.435	3791	36
3	Broken in tension	2.48	1588	60
4a	Broken in bending	1.56	2001	48
4b	Same fiber as above	1.36	2144	48
5a	Broken in bending	1.38	2128	49
5b	Same fiber as above	1.11	2373	49
6a	Broken in tension	7.95	887	51
6b	Same fiber as above	7.5	912	51

Fibers 4 and 5 were broken on carbon tape as described above and the fracture faces observed are matching with the exception of the spur-type cantilever curl, which likely broke off during the breaking process. Taking the average calculated stress over both mirrors, the stress at the origin of fracture for this fiber was 2.16 ± 0.13 GPa. Commercially available SiC fibers such as NLM, Hi-Nicalon, Hi-Nicalon type S, SA, and Sylramic all have tensile strengths around 2.8 GPa [127] [128]. The values obtained for

the fibers produced by Free Form Fibers are on a similar scale as other commercially available fibers. A different group produced an amorphous boron-modified SiC fiber [129] which although smaller diameter, had lower tensile strength (1.36 GPa) and large, obvious flaws at the origin of fracture.

Returning to fiber-1 (Figure 5.1), the careful observer may notice secondary fracture lines below the primary fracture surface. These were further examined in the HIM and shown in detail in Figure 5.6.

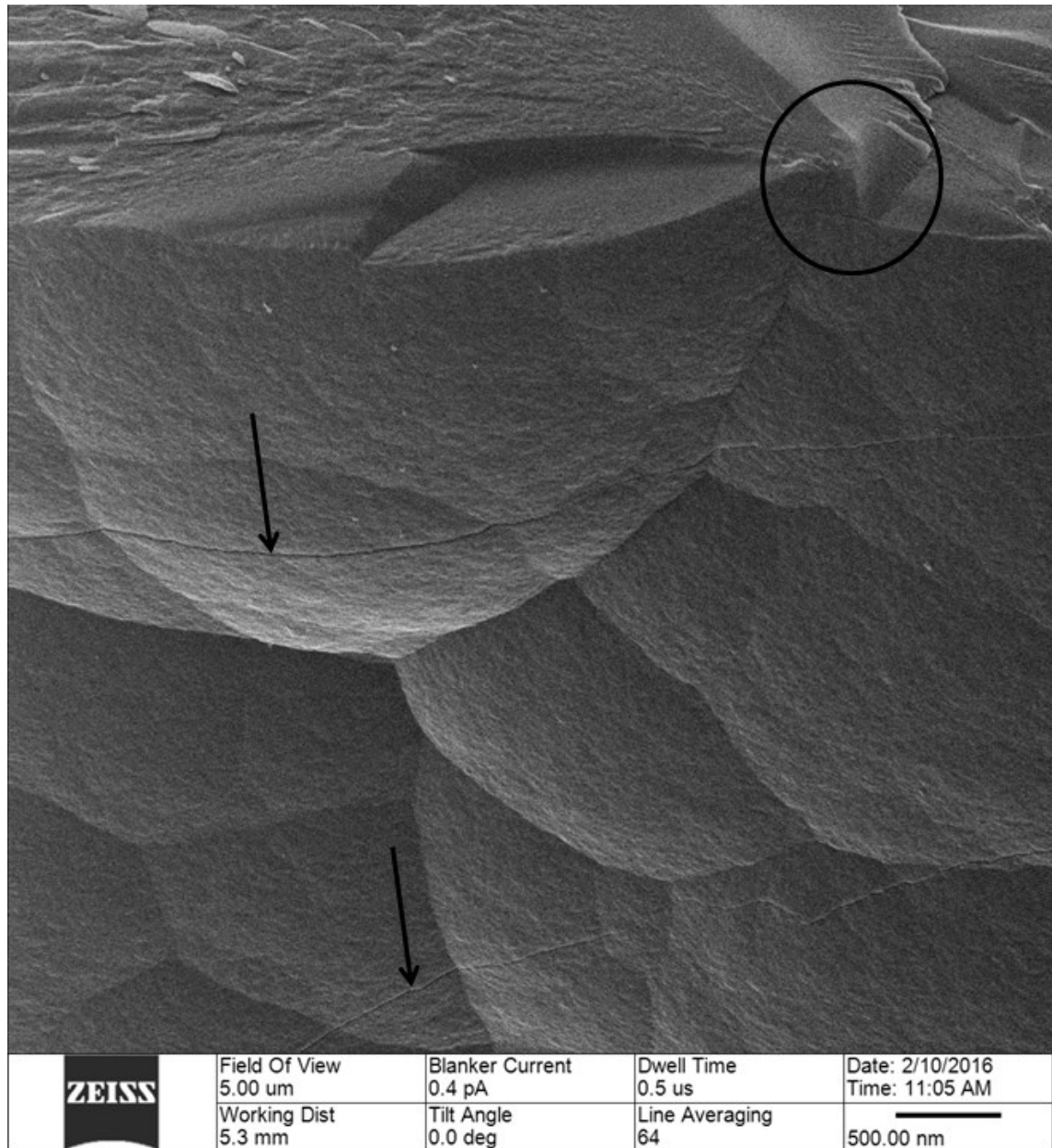


Figure 5.6: The primary fracture face is observable at the top of the image, while arrows indicate the locations of surface cracks on the outside of the fiber below the primary face. The probable origin is circled.

It is probable that the fiber began to crack in multiple locations during bending (indicated by arrows) before one location grew in size until fast fracture could occur. This ended up being the primary fracture face and is supported by the relatively large mirror size on this fiber. It is also possible that these cracks were the beginnings of secondary fractures that

occurred after the fiber had broken – during the period when the fiber is violently vibrating. The opposite side was not able to be imaged, but examination for surface cracks would indicate whether or not the cracks are from secondary fracture. If the cracks were from secondary fracture, they would be seen on all sides of the fiber, rather than only on the tensile side, which would indicate stress relief as the fiber was being bent. The fracture mirror has a radius of $4.25\text{ }\mu\text{m}$ while the fiber radius is only $58\text{ }\mu\text{m}$. Other fibers examined have smaller mirrors and no observable secondary initiation sites visible. The probable origin is circled; it is likely that the origin is at the meeting of two of the bumps visible on the surface of the fiber.

Returning to the fiber shown in Figure 5.3, images were taken away from the initiation point and near the cantilever curl. Observation of the fracture surface in this region shows a very obvious and distinct change in how the fracture propagated through the material (Figure 5.7).

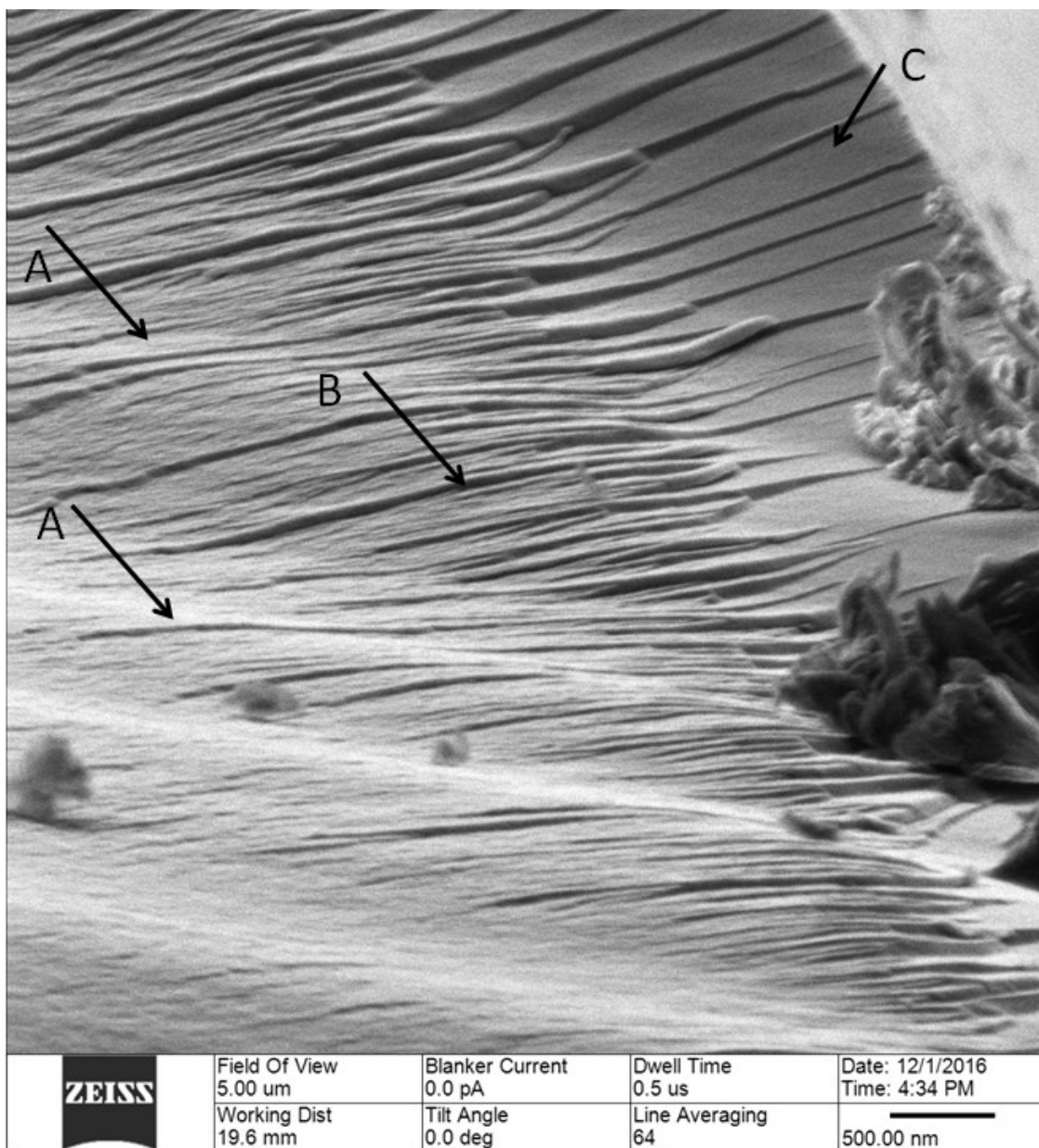


Figure 5.7: Not only is there a subtle waviness in the fracture surface (A), but the local variations due to the polycrystalline nature of the fiber (B) show a marked change from the inside of the fiber to near the border with the amorphous Si region to the a-Si region (C) that shows a very distinct difference due to its crystal structure (or lack thereof).

The a-Si region is 1.5 microns thick on this fiber. The twist hackle pointed out by 'B' shows a sharp change in morphology when it comes into contact with the a-Si layer from

the crystalline SiC interior. The twist hackle shows how the crack propagated outwards from the center as well as across the fiber in bending.

5.2 Raman spectroscopy

Micro-Raman spectroscopy was performed on various fibers provided by Free Form Fibers LLC. Three lasers were utilized: the 514nm green, 633nm red, and 785nm near-IR laser. Each one has a different depth of penetration and thus different sampling volume in silicon carbide and silicon. From section 2.4 and 2.5, the depth of penetration in 3C-SiC is 6.6 μm , 7.6 μm , and 6 μm respectively. From the same sections, the depth of penetration in crystalline Si is 0.1 μm , 0.29 μm , and 0.76 μm respectively. The depth of penetration is then combined with spot size of the laser, that being $\sim 2 \mu\text{m}$ for both the 514nm and 633nm lasers. The 785nm laser being a line laser, the effective spot area is $\sim 2 \mu\text{m} \times 10 \mu\text{m}$. Of these, it is clear that the sample volume increases with increasing laser wavelength (and spot size in the case of the 785nm laser).

Spectra were taken on both the outside a-Si surface of the fibers as well as on polished cross-sections of fibers. Sample spectra taken from the outside of the fibers are shown in Figure 5.8, Figure 5.9, and Figure 5.10. Sample spectra taken from the cross-section of the fibers are shown in Figure 5.11, Figure 5.12, and Figure 5.13.

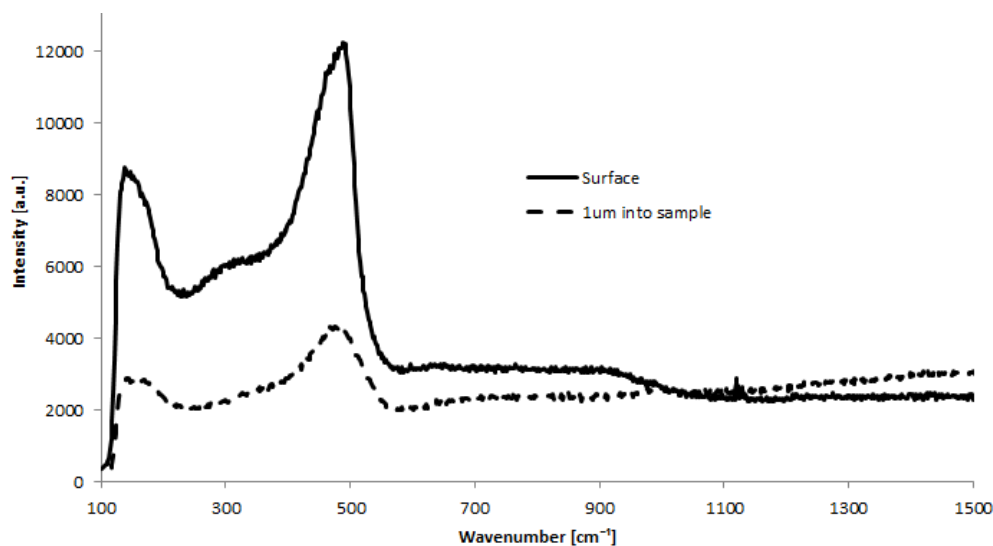


Figure 5.8: Spectra taken with the 514nm laser on the outside surface of fibers at two focal depths – one focused on the surface of the fiber and the other focused 1 micron into the surface. There is a sharp change in intensity, but the amorphous silicon peaks show quite well. There is some order within the a-Si, as seen by the sharpness of the peak at 480 cm^{-1} .

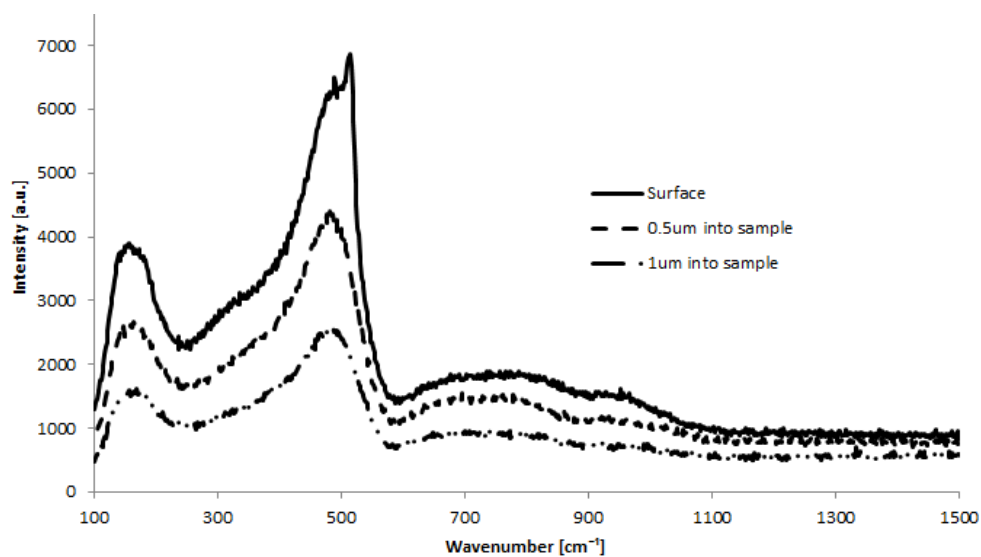


Figure 5.9: Spectra were taken at three focal depths with the 633nm laser: at the surface, $0.5\mu\text{m}$ into the sample, and $1\mu\text{m}$ into the sample. There is some crystallinity present at the surface of the a-Si, likely due to this being the most silicon-rich region of the fiber. Also visible are broad humps in the $600\text{--}1000\text{cm}^{-1}$ range; these are likely due to the small amount of C bonding with the a-Si, forming a-SiC.

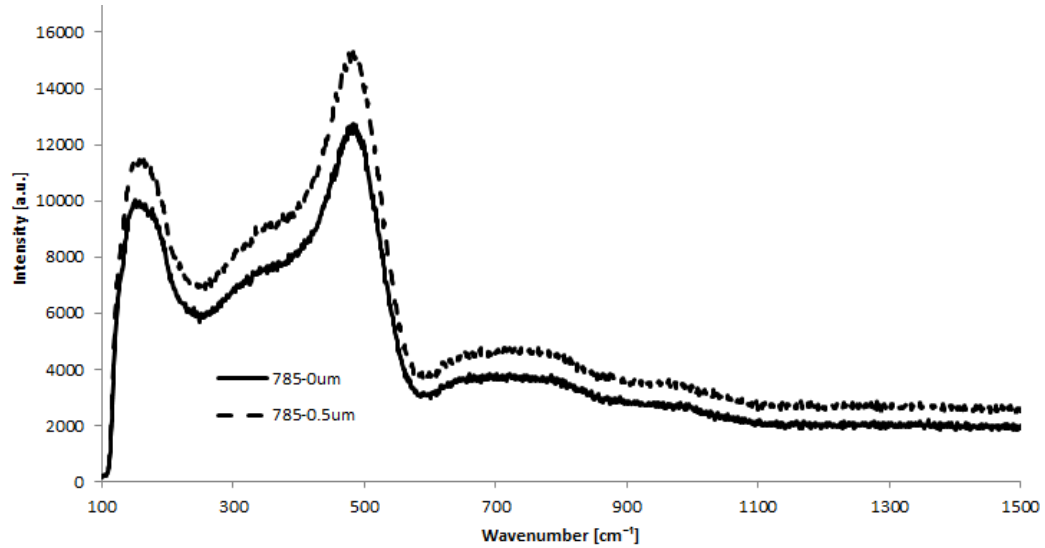


Figure 5.10: Spectra were taken at two focal depths (surface level and 0.5 μm into the sample) with the 785nm laser. The a-Si continues to show here, as does the a-SiC band seen with the 633nm laser.

The spectra obtained have great similarity to published work regarding a-SiC composed of various ratios of Si:C [130]. In particular, it closely matches the spectra seen for the ratios of 0.69:0.31 and 0.8:0.2. Further examination of the cross-section of the fibers show the transition from a-Si on the outside layer of the fiber to crystalline SiC inside the fiber (Figure 5.11 and Figure 5.12).

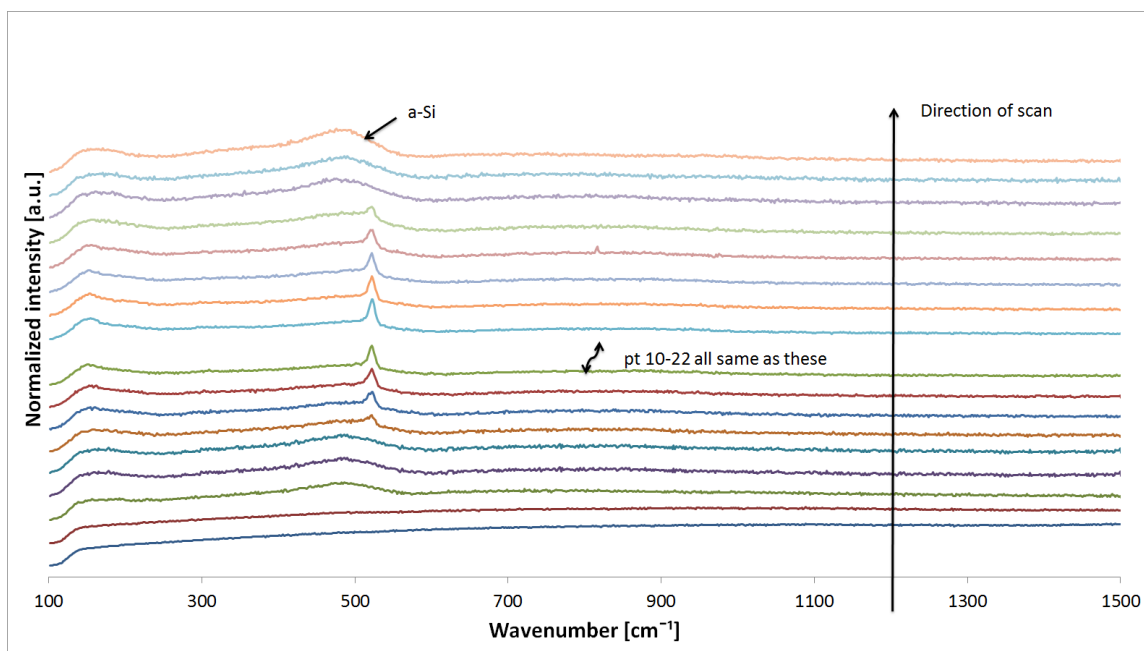


Figure 5.11: A line of spectra was taken across the cross-section of a fiber with the 633nm laser. Each point was 2 μm from the previous. It is clear that on this particular fiber, the a-Si region is $\sim 5 \mu\text{m}$ thick, with a small transitional region in the crystalline-SiC where a-Si still shows up some. This particular scan was performed across the entire width of a fiber with the two bottom spectra being taken off the fiber. The a-Si is visible on both sides of the fiber for the same number of spectra.

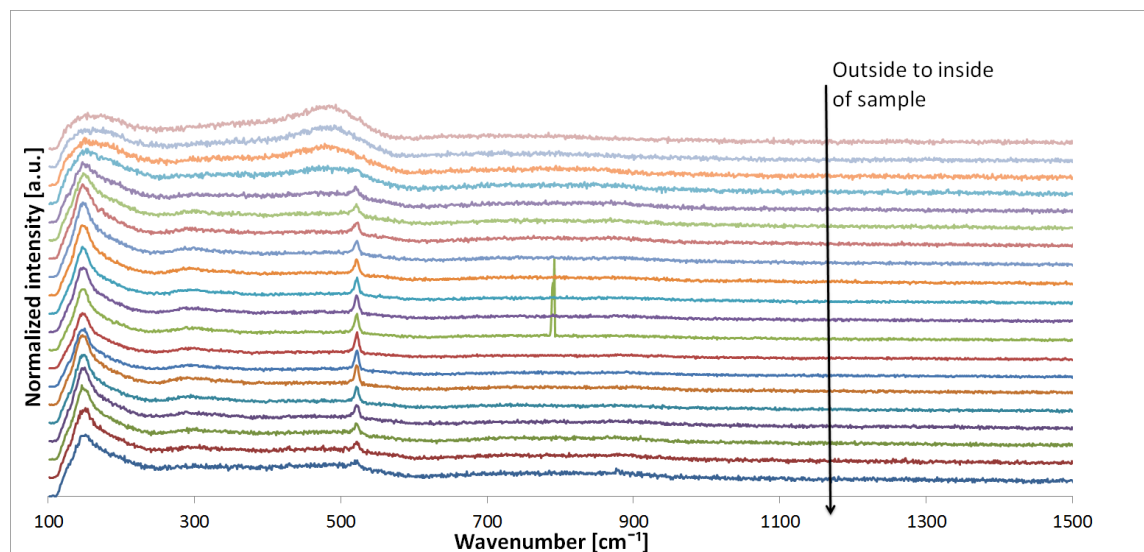


Figure 5.12: A map similar to the one shown above was made with the 785nm laser but was not allowed to extend past the edge of the fiber as the substrate it was mounted to would burn. This laser reveals the same characteristic a-Si to crystalline-SiC transition. Additionally, there is a clear doublet halfway through the map;

this is likely due to an unusually large crystal of SiC being caught by the larger sample volume of the 785nm laser.

Last, spectra were taken within a very small window of wavenumbers, as the a-Si and c-Si both overwhelm the intensity of most SiC peaks. These are shown in Figure 5.13.

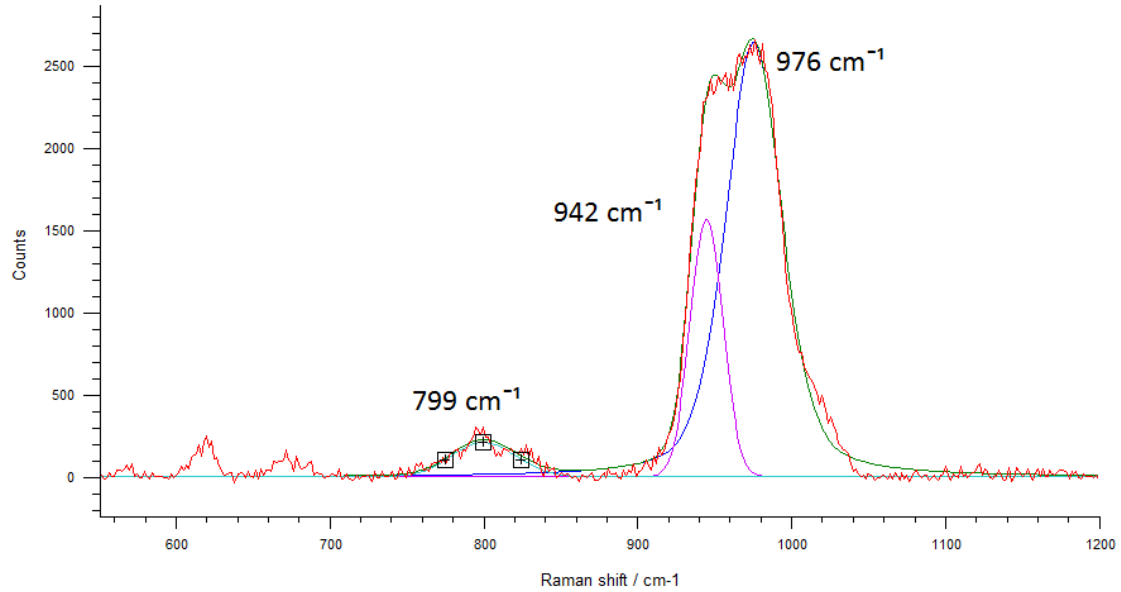


Figure 5.13: A sample spectrum taken with the 633nm laser in the center of a polished cross-section of a fiber. Three peaks have been fitted with the Wire 4.2 software: 796/799 cm⁻¹ LO peak, 942 cm⁻¹ unknown peak, and 976 cm⁻¹ TO peak.

The peaks seen in Figure 5.13 match closely with the peaks that exist in 3C-SiC, namely the 796 cm⁻¹ TO and 976 cm⁻¹ LO peaks. The 942 cm⁻¹ peak is probably due to peak splitting – as silicon carbide crystals decrease in size they approach a crystalline detection limit [127] [131]. The SiC peaks begin to split and appear as amorphous SiC. The broadening of the 796 cm⁻¹ peak as well as the splitting and broadening of the 976 cm⁻¹ peak are evidence of this. For crystals between 5nm and 200nm, the Raman spectrum will show amorphous SiC, possibly increased stacking faults, and shifted peaks [132] [54].

6 Four-point bend apparatus for *in situ* micro-Raman stress measurements

The following paper was published in Measurement Science and Technology **29** (2018) 065903

Shawn H. Ward and Adrian B. Mann

Rutgers, the State University of New Jersey

E-mail: shawn.ward@rutgers.edu

Abstract

A device for in-situ use with a micro-Raman microscope to determine stress from the Raman peak position was designed and validated. The device is a four-point bend machine with a micro-stepping motor and load cell, allowing for fine movement and accurate readings of the applied force. The machine has a small footprint and easily fits on most optical microscope stages. The results obtained from silicon are in good agreement with published literature values for the linear relationship between stress and peak position for the 520.8 cm^{-1} Raman peak. The device was used to examine 4H-SiC and a good linear relationship was found between the 798 cm^{-1} Raman peak position and stress with the proportionality coefficient being close to the theoretical value of 0.0025. The 777 cm^{-1} Raman peak also showed a linear dependence on stress, but the dependence was not as strong. The device examines both the tensile and compressive sides of the beam in bending, granting the potential for many materials and crystal orientations to be examined.

Keywords

Raman, stress, silicon, silicon carbide, four-point bend, micro-Raman, in-situ

Introduction

Stresses can be imparted on semiconductor wafers through a variety of means, from polishing, etching, depositing, and cleaving or resizing the wafer, to thermal and mechanical stresses in a given application. Silicon and silicon carbide wafers in particular are ubiquitous for use in high stress, high temperature environments. Determining the stress in the wafer through non-destructive means pre- and post-processing is essential to maintaining wafer integrity and pushing the limits of wafer design.

Raman spectroscopy is a non-invasive method of fingerprinting vibrational modes within a crystalline material. The peaks that occur in single crystal semiconductors such as silicon and silicon carbide represent phonon modes in the materials. Under strain, the lattice within crystalline materials deforms slightly, changing the energy and, hence, wavelength of the phonons. The change in energy of the phonons affects the Raman peak position for a particular phonon mode. This effect of strain (stress) on the Raman peak position often follows a linear relationship. By purposefully straining a material by a known amount it is possible to determine the linearity of the relationship and the proportionality coefficient. This relates stress to change in Raman peak position, $\Delta\omega$, measured as a wavenumber equivalent to the number wavelengths per cm (cm^{-1}).

Raman micro-spectroscopy is commonly used to investigate the change in stress in a range of materials [1-3]. Knowing the exact change in Raman peak position with stress is

important as it enables quantitative values of stress to be found which can directly impact the performance and characteristics of the material. Previously static uniaxial stress tests combined with in-situ Raman spectroscopy have been performed [6]. These tests have demonstrated the possibility of using Raman measurements of uniaxially strained crystals to determine the spring constants of the lattice through phonon vibrations. Experiments utilizing three-point bending have examined the tensile face of electronic ceramics under stress [5]. A different three-point bend setup was used to examine Si wafers [6], and, similar to the other three-point bend study [5] the stress state on the tensile face was examined through a back-reflecting microscope. A four-point bend test has also been reported, but similarly to the other tests it solely examined the tensile side of the specimen [7]. Diamond anvil-cell tests with in-situ Raman have been used to investigate the relationship between hydrostatic pressure and Raman peak position, but suffer from probing only the effect of compressive stress [8].

There are two ways to present the expected linear relationship between stress (σ) in MPa and the change in Raman peak position ($\Delta\omega$) in cm^{-1} :

$$\Delta\omega = -C \cdot \sigma \quad (1)$$

or:

$$\sigma = -\Delta\omega / C \quad (2)$$

where C is the proportionality coefficient relating change in Raman peak position to stress. Other researchers have taken tensile stress to be negative, but in the current study

we use the standard convention where compressive stresses are negative and tensile stresses positive. Reporting of other group's work has been adjusted to reflect this.

Some groups have given their results in terms of equation (2), but in the current study the values of their coefficients have been converted to the form used in equation (1) for consistency and ease of comparison with the experimental results. The previously measured and theoretical values for the proportionality coefficient are given in Table 6.1 for single crystals of silicon (100) and silicon carbide with two different crystal structures (3C and 6H). Many groups [4, 9-11] use a combination of hydrostatic and uniaxial stress to determine the stress state in a silicon carbide sample, utilizing the equation:

$$\Delta\omega_T = 2\sigma\eta_H^T + \left(\frac{1}{3}\right)\sigma\eta_U^T \quad (3)$$

where $\Delta\omega_T$ is the change in wavenumber of the E1(TO) Raman peak, σ is stress, and η is the proportionality coefficient relating stress to peak position with the subscript H denoting the hydrostatic component and subscript U the uniaxial component. Few groups have experimentally determined the proportionality coefficient for uniaxial stress for both of the TO bands in 4H- and 6H-SiC. Calculations have been performed to determine the state of stress in 4H-SiC wafers utilizing the peak shift of 3C-SiC as an approximation for the peak shift in 4H-SiC [10], but a direct determination of this relation has not been performed. The device described here provides the means to easily determine this proportionality coefficient.

Table 6.1: The proportionality coefficient 'C' for silicon and silicon carbide.

	C (cm ⁻¹ /MPa)	Source	Crystallinity	Notes
Si-1	0.0020	[12]	Single crystal	Experiment & Theory
Si-1	0.0023	[13]	Single crystal	Experiment
Si-1	0.00222	[14]	Single crystal	Experiment
3C-SiC-E1(TO)	0.0025	[9]	Single crystal	Theory, no hydrostatic stress
6H-SiC-TO	0.0031	[15]	Single crystal	Experiment, hydrostatic stress, 789 cm ⁻¹ peak
6H-SiC-TO	0.27	[5]	Poly crystal	Experiment, 796 cm ⁻¹ peak
6H-SiC-LO	0.59	[5]	Poly crystal	Experiment, 777 cm ⁻¹ peak

In the current work 4H-SiC is examined which is expected to be most like the 3C-SiC TO peak in terms of the proportionality coefficient relating stress to Raman peak position [133], but unfortunately a direct determination of the proportionality coefficient for the TO peak in 4H-SiC in uniaxial stress is not available in the published literature.

Of the prior testing performed, not all values match, especially in the investigation of silicon carbide. The work by Fist et al. [5] is especially interesting as their values reflect the Raman shift in small crystals of 6H-SiC (10 wt%) in ZrB₂. Additionally, the maximum stress reached in their work peaked at 75 MPa.

When using micro-Raman knowing the volume that is being examined is important. An estimate of the depth of laser penetration can be calculated for both Si-1 and 4H-SiC from the optical penetration depth of incident light which depends on $1/\alpha$, where α is the absorption coefficient. For silicon (Si-1) using $\alpha = 3.27 \times 10^3 \text{ cm}^{-1}$ [16] at an incident laser wavelength of 630 nm the penetration depth is 3 μm . For silicon carbide (4H-SiC), $\alpha = 54325 \text{ cm}^{-1}$ at an incident laser wavelength of 630 nm [17], which gives a penetration depth of around 0.18 μm . The penetration depth combined with the microscope's spot size (approximately 2 μm) determines the volume sampled by the micro-Raman.

Design

The four-point bend apparatus was designed to examine the change in Raman peak wavenumber at locations on the test sample across the neutral axis of bending. The device was designed to simulate ASTM-C1161, and if desired may be used to determine fracture toughness as per ASTM-C1421 and crack growth parameters as per ASTM-C1576. Sample shape is allowed to vary more than the standards specify to increase the range of strains possible in a sample (typically a wafer) and to allow for a degree of reproducibility in the specimens. Figure 6.1 shows a beam in a general four-point bending configuration. The x-y face is perpendicular to the direction of bending and the neutral axis. This face is of significant interest as it presents a cross section where different regions are under loads that are compressive, tensile, and unstressed, respectively. The design of the four-point device enables it to be placed so the x-y face of the specimen is perpendicular to the incident laser of the Raman microscope, thus

allowing the effects of both tensile stress and compressive stress on the Raman spectrum to be studied. Figure 6.1 shows the x-axis and y-axis, with the z-axis out of the page.

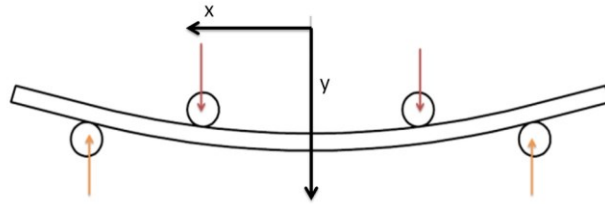


Figure 6.1: A beam in four-point bending is shown; the x- and y-axes shown are the ones used in this work. The z-axis is out of the page.

The machine utilizes a micro-stepping stepper motor capable of 25400 steps/rev. This, along with an 8-32 drive screw and one-to-one gearing, allows for precise control ($\pm 1 \mu\text{m}$) of the deflection imparted on the specimen. The machine was designed to be self-aligning with increasing force, through use of a ball joint type assembly connecting the driven jaw to the screw (inset of Figure 6.2). The jaws of the machine are described as being either on the tensile side of the specimen (convex surface) or the compressive side of the specimen (concave surface) in bending. A load cell (E on Figure 6.2) connects the tensile side of the bending rig to the base, allowing for measurement of the load independent of deflection. The simple beam geometry of the test specimen allows for easy calculation of stress, when using the observed load. The entire instrument is shown in top down view in Figure 6.2 while Figure 6.3 provides a view of the device under the Raman microscope.

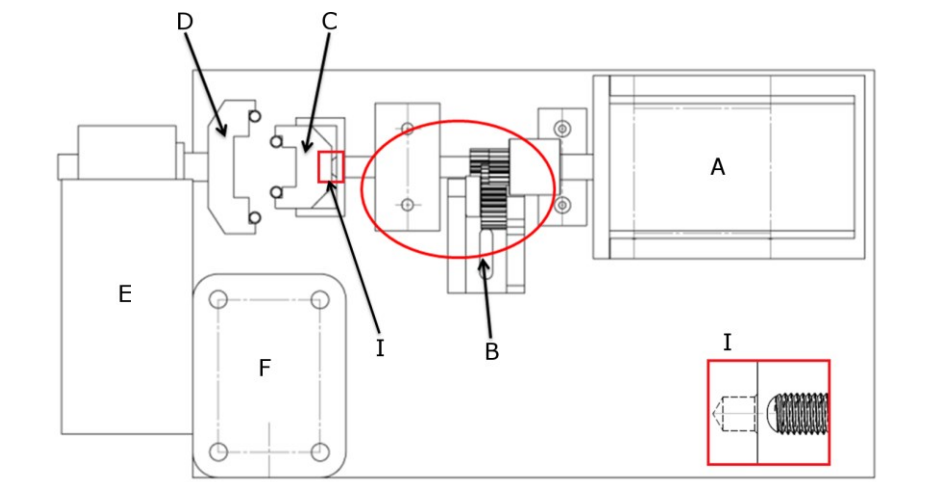


Figure 6.2: A top down view of the designed four-point bending mechanism. The labeled parts are: A) stepper motor; B) 1:1 gearing and 8-32 going through threaded block; C) compressive side jaw; D) tensile side jaw; E) load cell; and F) load cell connector. I is the inset of the open ball joint used to allow for free rotation of the jaw on the thrust axis. The compressive side of the jaw is driven by the stepper motor; both jaws have cylindrical pins as the contact points with the sample. The pins are glued to the jaws. The load cell is rigidly attached to the baseplate via a large block of aluminum (F).

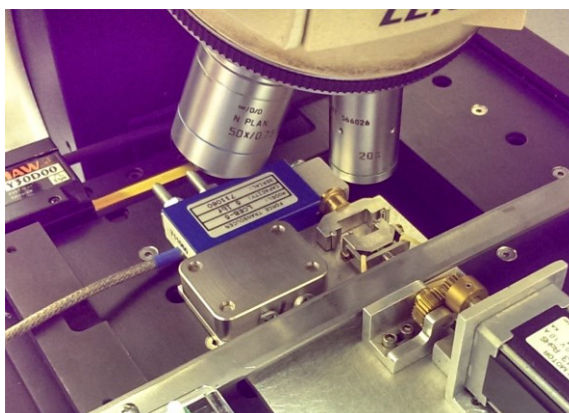


Figure 6.3: The device sitting in-situ on the Raman microscope stage. A 20x objective lens is shown. An elastic band (barely visible) produces enough force to maintain contact between the compressive jaw and the drive shaft to help eliminate positioning errors. The steel bar across the instrument is bolted to the stage, clamping the instrument down and preventing any motion due to weight and movement of the cables and wires.

The tensile side jaw spacing is 20 mm while the compressive side jaw spacing is 10 mm (measured at the point of contact with the specimen). The jaws height is 6 mm. The jaws and base plate are made from 304 stainless steel and the other metal parts are brass (gears and bushing) or aluminum (gear blocks and load cell connection block). The stepper motor used is an Omega HT11-013 micro-stepping motor. Software and microcontroller used are the Si Programmer by Applied Motion Products and a 1240i drive microcontroller. Machined parts were made in-house at the Rutgers Physics machine shop. The load cell and digital readout used are Omega LCEB-5 and Omega DP25-S.

The Raman system used was a Renishaw inVia™ micro-Raman Spectrometer controlled by Wire 3.4™ software. A HeNe laser of excitation wavelength 633 nm was used for all experiments. Laser powers used in the current work were 4.83 mW at the objective, with reduced powers possible through the software of 2.28 mW and 0.32 mW.

A Leica DM/LM microscope with Leica 50x, 20x, and 5x objectives fitted was used with the Renishaw Raman spectrometer. The microscope has a position stage based on the Prior ProScan II with controller. During the testing the 20x lens was the most used objective and it was found that there was no difference in results between 50x and 20x in terms of the determined proportionality coefficients.

Experimental

Before every test the Raman microscope and the objective lens to be used were calibrated with a piece of polished single crystal Si-I that has been cleaned in sequence with

acetone, ethanol, and methanol. The spectrometer is then calibrated to the Si-1 peak located at 520.8 cm^{-1} using the laser power that will be used during subsequent testing of the sample. The load cell is recalibrated every 25 to 35 uses. The calibration procedure for the load cell follows that outlined in the DP25-S manual with the calibration for loads ranging from 0.27 N to 9.80 N. The accuracy of the calibration is within 0.02 N.

The samples used in the four-point bend mechanism were made by cleaving double-side polished, undoped wafers of Si into rectangles approximately 25 mm long and 3 mm to 6 mm wide. The thickness of the sample remains the same as the thickness of the wafer. Precise cleaving is necessary to obtain a smooth, flaw-free edge on the sample. Often one side of the cleaned wafer will have a cleavage lip that is observable with the microscope. Samples of silicon carbide were made by cutting a wafer with a diamond saw and then polishing the cut edges flat and perpendicular to the wafer face. All samples were cleaned with acetone, ethanol, and methanol before being loaded into the device. The typical sample (wafer) thickness in this study was $280\text{ }\mu\text{m} \pm 5\text{ }\mu\text{m}$ for Si and around $360\text{ }\mu\text{m}$ (manufacturer specification) for 4H-SiC.

It is necessary to obtain a stress-free baseline of the Raman spectrum of the material in question before beginning to stress it. This was done by performing a scan of the surface prior to insertion into the jaws of the machine. At least five scans at two separate locations are performed to acquire the best baseline.

During the testing three different load ranges are used. In the lowest load range the machine is given a command to move 500 steps (equivalent to 15 μm), pause for one second, and repeat until a preload of 0.68 N to 1.00 N is reached. Once this load has been obtained, gentle tapping of the compressive side of the jaws is done to help align the sample in the jaws. Following this, the locations of the points of contact are recorded and used to determine the exact center of the specimen. The zero-point of the xyz stage is then reset to the center of the compressive side of the sample. This allows for greater repeatability in measurements. All measurements begin on the compressive side of the sample and scan to the tensile side, crossing the neutral axis in the process.

The Raman measurements were performed using the Renishaw WiRE™ software to set up an array of points that form a raster scan. Raman spectra were obtained at each point with the spacing between individual points being typically 5-10 μm in the x-direction and 10 μm in the y-direction. Overall, the array comprises 7-10 points in the x-direction. In the y-direction it is aligned across the center of the sample with the array going from the compressive side of the wafer to the tensile side. The spacing was chosen to allow for reasonably fast scans with the points far enough apart that local laser heating is reduced (approximately 10 μm). The laser power was set at 2.28 mW or 0.32 mW, depending on the strength of the Raman counts received. Using the laser at 100% power overwhelmed the CCD detector, so the highest power avoiding this issue was used with a 10s dwell time instituted as part of the “Extended Scan” procedure present with WiRE™ software.

For the intermediate loading range the wafers are loaded to between 3.90 N and 4.90 N (typically); this load for the given wafer thickness and width stresses the sample to approximately one half of its breaking stress. The micro-Raman spectra are obtained using the same process as previously outlined and the parameters are kept the same to give an array over the wafer's cross-section. For the highest loading range the sample is loaded close to its maximum strength (6.80 N to 8.80 N, depending on edge quality) and another array of micro-Raman spectra obtained. Samples with poor edge quality or of extremely high brittleness will not sustain these higher loads. If this is the case, arrays can be made after every 0.98 N increase in load starting from the lowest load range. At each load, the deflection is noted and used to determine the strain in the sample. The values obtained are then compared to the calculated strain from the known load and geometry to validate the results.

Results

Silicon

Single crystal, double-side polished, undoped silicon wafers of thickness 280 μm were tested. Silicon samples were produced by cleaving wafers into a range of sample dimensions which resulted in different moments of inertia, I .

The change in wavenumber was plotted against known stress in the sample to determine the relationship between σ and $\Delta\omega$. Figure 4 presents plots of data from two loading experiments on the same sample, but for the lower load plot the machine jaws had not yet self-aligned. This causes the slope to be very different to that expected and, hence, the

measured proportionality coefficient between wavenumber and stress is inaccurate until the sample is aligned correctly. When measuring the change in wavenumber it is relative to the value at zero stress (neutral axis of the curved wafer).

The stress is found from the y-axis position and calculated via the equation [18]:

$$\sigma = \frac{Mc}{I} \quad (4)$$

where M is moment due to the force being applied, c is the distance from the neutral axis to the outside edge (where the greatest stress is), and I is the moment of inertia of the sample. The moment at the center of the beam is constant over the length of the compressive side jaw opening and is simply calculated as:

$$M = \frac{P}{2} \cdot \frac{l}{4} \quad (5)$$

where P is the measured applied force and l is the span of the tensile side jaws. Equation 4 can be combined with equation 5 and re-written for this specific geometry as:

$$\frac{P \cdot 10^{-3}}{2} \cdot g \cdot \frac{l}{4} \cdot \frac{(dNA) \cdot 10^{-6}}{I} \cdot 10^{-6} = \sigma \quad (6)$$

where P is the applied load measured by the load cell in grams, g is the acceleration due to gravity in m/s^2 , l is the tensile jaw spacing in meters, dNA is the distance from the neutral axis in microns, I is the moment of inertia in m^4 , and σ is stress in MPa.

The average shift in wavenumber for each y-position was calculated (since there are nine points in the x-direction for each y-position). The standard deviation of these points is a statistical error in the measurement of the shift in wavenumber. Additionally, there is an error in the wavenumber due to the limits of the spectrometer which is a machine error of $\pm 0.01 \text{ cm}^{-1}$. From these two known errors, total error in the shift in wavenumber can be

calculated. The error in stress was determined by taking the maximum possible error from the load cell and combining it with the statistical error in measurement of the dimensions of the sample. The maximum error in stress calculations seen is less than 5.7%. These errors are presented in Figure 6.4 as error bars, but are barely visible since they are very small.

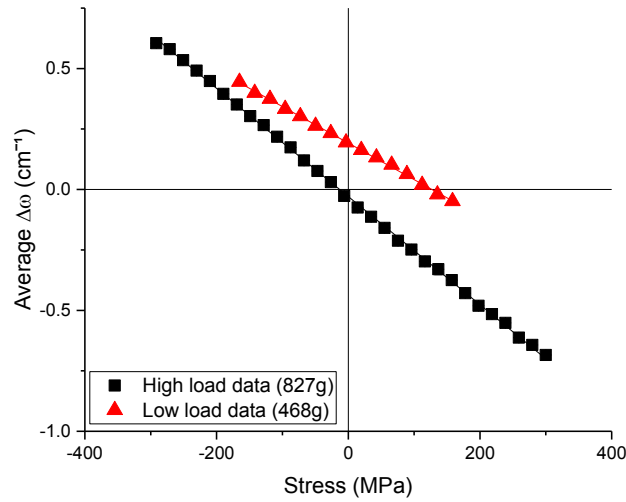


Figure 6.4: The high load data presented above shows an excellent linear relationship between $\Delta\omega$ and stress. The slope and intersection are as expected based on literature values review (Table 6.1) and are consistent across multiple samples. The error bars on each point are for stress ± 10.85 MPa and for wavenumber ± 0.017 cm^{-1} but do not show up as they are so small. The low load data shown is from the same piece of silicon. At this load, the sample has not aligned correctly in the jaws of the machine and as such, the stresses and wavenumbers are not as expected.

The linear regression shows a relation of $\Delta\omega = -0.00224(\pm 8\text{E-}6) \sigma$. Taking the coefficient of determination, R^2 , as a measure of the fit a value of 0.999 was found. This shows that the machine works as expected and the samples used were of good quality and had a level surface. Verification of the results against prior theoretical and experimental work

[12,13,14] shows an error less than 3% in the value of ‘C’. This result indicates that the device and method behave as anticipated.

Silicon carbide

In addition to single crystal silicon the functionality of the bend tester was verified by using the instrument on a different single crystal. A 4H-SiC wafer was tested to determine the relation between stress and shift in wavenumber experimentally. An example Raman spectrum showing the peak positions for 4H-SiC is shown in Figure 6.5.

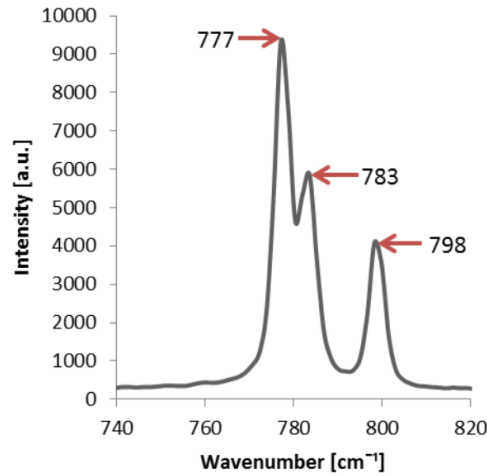


Figure 6.5: A sample spectrum of 4H-SiC in the wavenumber region of interest. The 798 cm⁻¹ E1 (TO) peak and 777 cm⁻¹ E2 (TO) peak are indicated. The third major peak present, the 783 cm⁻¹ peak is a second E2 (TO) peak. All these peaks are seen as the laser is not polarized and can excite multiple modes.

The 798 cm⁻¹ E1 (TO) peak of 4H-SiC was examined in this work due to its clarity in a spectrum. The 777 cm⁻¹ E2 (TO) peak was also examined as the strongest peak. The SiC wafer sample tested was an N-type 4H-SiC, 360 μm thick. The wafer surfaces are the (0001) and (000 $\bar{1}$) faces, respectively; these faces are in uniaxial tension or compression in the machine set-up. The width of the sample was measured to be 4.47 mm after the

polishing process removed diamond saw marks. The sample edges were polished to 7 μm grit size with an emphasis on polishing parallel to the long axis to decrease damage to the edges. As with the silicon, the sample was cleaned in sequence with acetone, ethanol, and methanol before the experiment began.

Micro-Raman spectra in arrays similar to those in silicon were obtained at loads of 2.80 N, 4.51 N, 6.13 N, 7.60 N, and 9.07 N. The change in wavenumber ($\Delta\omega$) due to the applied load was plotted against the known stress in the sample based on its geometry, and this was used to determine the relationship between stress and $\Delta\omega$. The error bars are significantly larger than those with the silicon which is partially due to the edges being polished rather than cleaved; in SiC polishing can introduce residual stresses and stacking faults which affect the Raman peak position [19]. Additionally, the overall quality of SiC wafers (crystallinity) is generally inferior to that of silicon which tends to broaden the Raman peaks. Figure 6.6 shows the linear relationship between stress and wavenumber as determined for the 798 cm^{-1} peak.

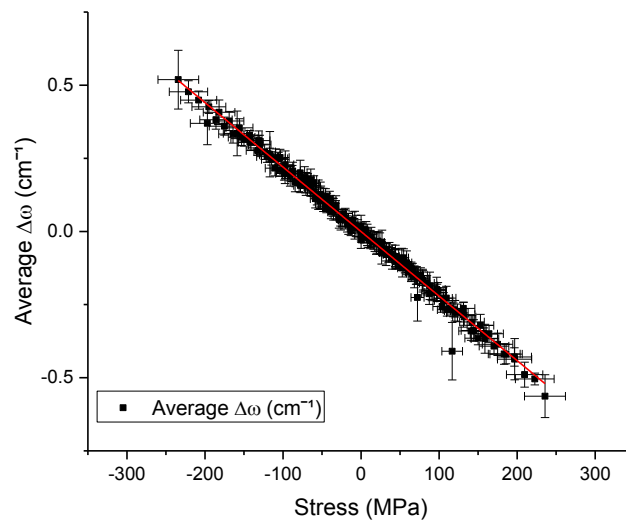


Figure 6.6: This graph shows the linear relation between the change in wavenumber for the 798 cm^{-1} peak with stress at five different loads. The curve fit is good with $R^2=0.99$.

The proportionality coefficient between wavenumber in cm^{-1} and stress in MPa is $\Delta\omega = -0.00221\sigma$ for the Raman peak at 798 cm^{-1} . Outliers at the highest stresses are due to the microscope being positioned on the edge of the sample giving more scatter in the wavenumber position. The errors in stress and wavenumber values were calculated in the same way as with silicon. The maximum error in stress was found to be less than 10% at a value of 26 MPa. The error in wavenumber was typically 0.025 cm^{-1} . Figure 6.7 shows the relation between change in wavenumber and stress for both the 798 cm^{-1} peak (black squares) and the 777 cm^{-1} peak (red triangles).

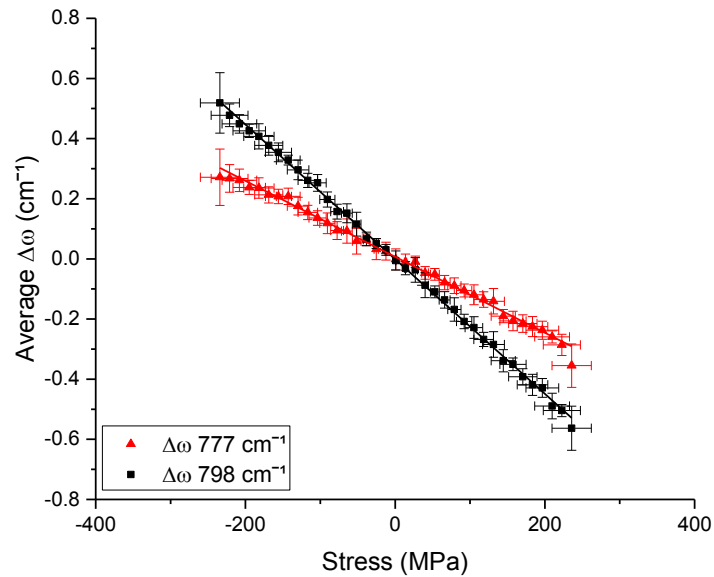


Figure 6.7: Data from the highest load applied to the SiC wafer using different Raman peaks. The red triangles represent data from the 777 cm^{-1} peak shift and the black squares represent data from the 798 cm^{-1} peak shift. This shows the clear difference in slope between the two peak shifts with respect to stress. The 777 cm^{-1} peak shifts with a proportionality coefficient of $0.00126(\pm 1.3\text{E-}5)$, whereas the 798 cm^{-1} peak shifts with a proportionality coefficient of $0.00221(\pm 1.4\text{E-}5)$.

A summary of the experimental results from the bend testing device are presented in Table 6.2 and compared with various literature values. It should be noted that Harima's value is theoretical, not experimental and is used in the calculation of combined uniaxial and hydrostatic stress state.

Table 6.2: A comparison of proportionality coefficients determined during this work for 4H-SiC and published values of these coefficients. Uniaxial stress is denoted U, hydrostatic stress is denoted H.

	C	error	Source [reference]	% diff. with exp.	U or H
4H-SiC-E1(TO)	0.00221	±8%	Experiment - this study	n/a	U
4H-SiC-E2(TO)	0.00126	±8%	Experiment - this study	n/a	U
3C-SiC-TO	0.0025		Harima [9]	+13%	U
3C-SiC-TO	0.0034		Yoshikawa [10]	+53%	U+H
3C-SiC-LO	0.0009		Yoshikawa [10]	-29%	U+H
6H-SiC-TO	0.0031		Liu [15]	+40%	U+H

Discussion

A small-scale four-point bending device was designed, built, and validated for use in-situ with a micro-Raman spectrometer. The device enables the assumed linear relationship between change in Raman peak position and stress to be investigated and the constant of proportionality, C , to be found. Of utmost importance to the operation of the device, aside from accurate calibration of the load cell, is creating a clean, flat edge. This cannot be sloped in any way to ensure that the microscope used with the Raman spectrometer can be focused accurately across the full width of the edge. A sloped side causes changes in the focal length which makes measurements problematic. This can be accounted for by

changing the Raman settings, but is best avoided. Cleaving of the sample is often superior to using a diamond saw and polishing; however, not all materials cleave well and even silicon may cleave in unwanted manners. If polishing is necessary then it is important that no scratches are optically visible in order to reduce the amount of scatter in the Raman signal. Multiple measurements across the full cross-section (tensile to compressive) should be taken over a range of loads. For brittle materials where the edges may be damaged during preparation the use of multiple scans is essential. It is also essential that the jaws of the machine be fully seated on the sample at low loads; gentle tapping of the compressive side of the sample helps the self-alignment process.

The device was validated by examining silicon and silicon carbide wafers. The change in Raman peak position in cm^{-1} for single crystal, undoped Si-1 was found to be $\Delta\omega = -0.00221\sigma$, where tensile stress is defined as positive and in units of MPa. This compares well to theoretical work examining the elastic deformation of silicon and was found to give a value within 10% of the expected value. Polished, N-type 4H-SiC was found to have a strong linear relationship between stress and peak position for the 777 cm^{-1} and 798 cm^{-1} peaks. These relationship were, respectively, $\Delta\omega = -0.00126\sigma$ for 777 cm^{-1} and $\Delta\omega = -0.00221\sigma$ for 798 cm^{-1} . Care must be taken when comparing these values to published work as 1) there is not currently a consensus regarding the peak shifts in 4H-SiC in the elastic regime and 2) the polishing (down to $7 \text{ }\mu\text{m}$ grit) may have introduced residual stress that may affect the magnitude of the change in wavenumber with stress. Future studies using this device can probe the response of other Raman-active materials, as well as potentially aid in investigation of the Raman shifts in the vicinity of crack tips.

Acknowledgements

The author would like to thank The Rutgers Physics machine shop for their excellent work, Sean Langan for his help with theory, Xiuyan Li for her help with the silicon carbide section, and the NSF support for the Ceramic, Composite, and Optical Materials Center (CCOMC). This material is based upon work supported by the National Science Foundation under Grant No. IIP 1540027.

References

- [1] N. Piluso, R. Anzalone, M. Camarda, A. Severino, G. D'Arrigo and F. La Via, "Stress fields analysis in 3C-SiC free-standing microstructures by micro-Raman spectroscopy," *Thin Solid Films*, vol. 522, pp. 20-22, 2012.
- [2] A. Canino, N. Piluso and F. La Via, "Large area optical characterization of 3 and 4 inches 4H-SiC wafers," *Thin Solid Films*, vol. 522, pp. 30-32, 2012.
- [3] C. H. Lee, T. Nishimura, K. Nagashio and A. Toriumi, "Origin of Self-limiting Oxidation of Ge in High-Pressure O₂ at Low Temperature," in *Extended Abstracts of the 2014 International Conference on Solid State Devices and Materials*, Tsukuba, 2014.
- [4] E. Anastassakis, A. Pinczuk and E. Burstein, "Effect of static uniaxial stress on the Raman spectrum of silicon," *Solid State Communications*, vol. 8, pp. 133-138, 1970.
- [5] N. Fist, J. Dinan, R. Stadelmann and N. Orlovskaya, "In situ three point bending device for measurements of vibrational response of ceramics under stress by microRaman spectroscopy," *Advances in Applied Ceramics*, vol. 111, no. 7, 2012.
- [6] S. J. Harris, A. E. O'Neill, W. Yang, P. Gustafson, J. Boileau, W. H. Weber, B. Majumdar and S. Ghosh, "Measurement of the state of stress in silicon with micro-Raman spectroscopy," *Journal of Applied Physics*, vol. 96, no. 7195, 2004.
- [7] C. Peng, C.-F. Huang, Y.-C. Fu, Y.-H. Hang, C.-Y. Lai, S.-T. Chang and C. W. Liu, "Comprehensive study of the Raman shifts of strained silicon and germanium," *Journal of Applied Physics*, vol. 105, 2009.
- [8] B. A. Weinsein and G. J. Piermarini, "Raman scattering and phonon dispersion in Si and GaP at very high pressure," *Physical Review B*, vol. 12, no. 4, pp. 1172-1186, 1975.
- [9] H. Harima, S. Nakashima, J. M. Carulli, C. P. Beetz and W. Yoo, "Characterization of 3C-SiC Epitaxial Layers on TiC(111) by Raman Scattering," *Jpn J. Appl. Phys*, vol. 1, no. 9A, pp. 5525-5531, 1997.
- [10] M. Yoshikawa, K. Kosaka, H. Seki and T. Kimoto, "Stress Characterization of 4H-SiC Metal-Oxide-Semiconductor Field-Effect Transistor (MOSFET) using Raman

Spectroscopy and Finite Element Method," *Applied Spectroscopy*, vol. 70, no. 7, pp. 1209-1213, 2016.

[11] J. DiGregorio, T. Furtak and J. Petrovic, "A technique for measuring residual stress in SiC whiskers within an alumina matrix through Raman spectroscopy," *Journal of Applied Physics*, vol. 71, no. 7, pp. 3524-31, 1992.

[12] I. De Wolf, "Micro-Raman spectroscopy to study local mechanical stress in silicon integrated circuits," *Semicon. Sci. Technol*, vol. 11, pp. 139-154, 1996.

[13] E. Anastassakis, A. Cantarero and M. Cardona, "Piezo-Raman measurements and anharmonic parameters in silicon and diamond," *Physical Review B*, vol. 41, no. 11, 1990.

[14] D. Kosemura, K. Usuda and A. Ogura, "Investigation of Phonon Deformation Potentials in Si_{1-x}Ge_x by Oil-Immersion Raman Spectroscopy," *Appl. Phys. Express*, vol. 5, 2012.

[15] J. Liu and Y. K. Vohra, "Raman Modes of 6H Polytype Silicon Carbide to Ultrahigh Pressures: A Comparison with Silicon and Diamond," *Phys. Rev. Lett.*, vol. 72, pp. 4105-4108, 1994.

[16] C. Honsberg and S. Bowden, "Optical Properties of Silicon," PV EDUCATION.ORG, [Online]. Available: PVEducation.org/pvcdrom/materials/optical-properties-of-silicon. [Accessed 16 1 2017].

[17] M. Polyanskiy, "RefractiveIndex.info," 2008-2016. [Online]. Available: refractiveindex.info/?shelf=main&book=SiC&page=Larruquert. [Accessed 16 1 2017].

[18] R. G. Budynas and J. K. Nisbett, 2011, *Shigley's Mechanical Engineering Design, 9th Edition* (New York, NY; McGraw-Hill) p 90

[19] B. Groth, R. Haber and A. B. Mann, "Raman Micro-Spectroscopy of Polytype and Structural Changes in 6H-Silicon Carbide due to Machining," *Applied Ceramic Technology*, vol. 12, no. 4, pp. 795-804, 2014.

7 Investigation of the uniaxial relation of stress and Raman peak shifts and the application thereof in single crystal YAG fibers

The following manuscript is being prepared for submission to the appropriate journal.

Shawn Ward¹, Subhabrata Bera^{1,2}, Adrian Mann¹, James Harrington¹

¹ Department of Materials Science and Engineering, Rutgers University, New Brunswick, New Jersey 08854

² National Energy Technology Laboratory, Pittsburgh, PA 15236-0940

Introduction and background

Raman spectroscopy has been used to determine the residual stress in various materials, notably silicon and silicon carbide [1-4]. Knowing the relation between the red or blue shifting of a specific peak in the Raman spectrum of that material with the amount of stress applied allows for this stress measurement technique. There are multiple methods available to obtain this relation, which comes in the form of Equation 1:

$$\Delta\omega = -C \cdot \sigma \quad (1)$$

where $\Delta\omega$ is the wavenumber shift of a given peak in cm^{-1} , C is the proportionality coefficient (determined experimentally or through first-principles analysis), and σ is the stress in MPa or GPa. The coordinate system used throughout this work is that compressive stress is negative and tensile stress positive; values of C from other sources have been adjusted to reflect this.

The in-situ four point bend device described in [5] was used to obtain a proportionality coefficient between stress and Raman peak shift in two different bars of undoped YAG – YAG HP (#04-0772-21) and YAG UP (#11-290-69). Each bar was polished with a 1 μ m grit diamond lapping pad on all four sides; the clearest side was chosen to be the top, as the micro-Raman used operates in a backscattering configuration. A piece of double-side polished single crystal silicon was used to calibrate the spectrometer before each map was made during testing. The machine was consistently calibrated to 520.60 cm^{-1} . Both the 514nm green laser and 633nm red laser were utilized, the 514nm laser being used in other studies [6] and giving the best signal in the 100-900 cm^{-1} region. Although there a large number of peaks visible, they are not all suitable as peaks to obtain a calibration curve. Small peaks can be overwhelmed by larger peaks and may disappear under certain orientations, whereas some large peaks do not shift significantly under stress due to the origin of the particular peak.

The peaks highlighted in Table 7.1 were the ones chosen to be more fully investigated in this work. One study performed a similar experiment to very high hydrostatic pressure (HiP) [6]. The proportionality coefficient is given from this paper when available. Of note is that the experimental and theoretical values of the peak locations can differ significantly from each other. An example spectrum of YAG is given in Figure 7.1.

Table 7.1: Position of various peaks along with symmetry of vibration, origin of vibration, and whether it was chosen for study. Symmetry and origin from Kostić et al and Aravanitidis [7,6]. The column ‘C hydro’ indicates the proportionality coefficient under hydrostatic stress determined experimentally.

Peak (cm ⁻¹) (Exp/HiP [90])	Symmetry	Origin	C hydro. (cm ⁻¹ /GPa) [90]
143/145	T _{2g}		1.9
162/163	E _g	Y translation	0.6
218/220	T _{2g}	Y translation	1.9
251			
263/263	T _{2g}	Translation, rotation, and v3 of AlO4	1.6
294/295	T _{2g}	Translation, rotation, and v3 of AlO4	2.4
339/340	E _g	Translation, rotation, and v3 of AlO4	2.7
370/370	A _{1g}	Translation, rotation, and v3 of AlO4	1.7
402/402	T _{2g}	Translation, rotation, and v3 of AlO4	2.4
543	T _{2g}	v2 of AlO4	
559/559	A _{1g}	v2 of AlO4	2.3
691/691	T _{2g}	v1 and v4 of AlO4	5.4
717/718	T _{2g}		5.1
755/754	E _g		5.3
782/783	A _{1g}	v1 and v4 of AlO4	4.0

856/857	T_{2g}	v1 and v4 of AlO_4	4.6
---------	----------	----------------------	-----

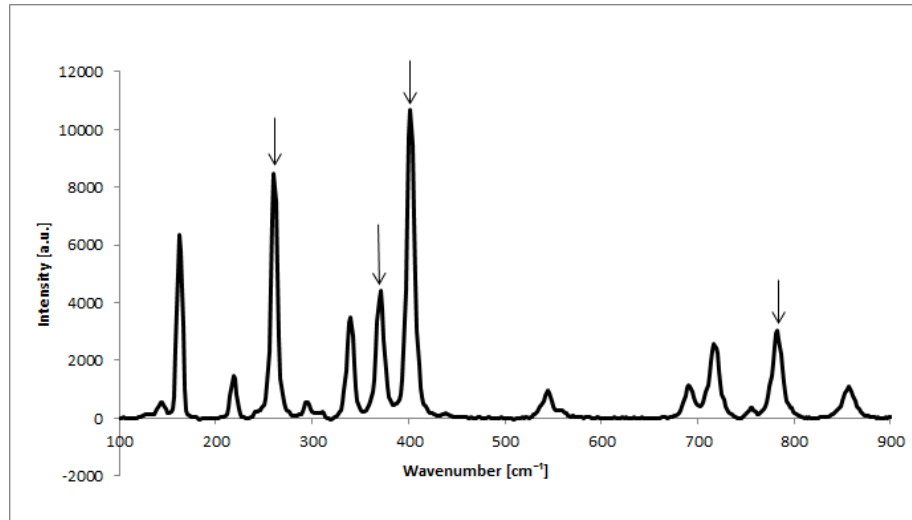


Figure 7.1: A sample spectrum of the Raman signal obtained from undoped single crystal YAG. Peaks examined in this work are indicated with an arrow.

Fibers grown from YAG bars can have residual stress in them, resulting in higher loss than stress-free fibers. As a method of determining the amount of residual stress in a fiber, Raman microscopy is an intriguing tool, as it is non-destructive and fast, requiring no special preparation of the sample other than cleaning. The four point bend method outlined above provides a way to calibrate Raman shift with directional stress. Residual stress can be a combination of both hydrostatic and deviatoric stress, so the proportionality constants need to be known for both to determine the complete state of residual stress in a Raman-active material [8].

Results

Four point bend measurements

Both HP:YAG and UP:YAG are undoped, so the peak coefficients between the two are very similar. The proportionality coefficient of the 782cm^{-1} peak is $C=1.53\pm0.05\text{ cm}^{-1}/\text{GPa}$ (Figure 7.2). The exact peak location at zero stress (location of the neutral axis) is 782.49 cm^{-1} with the machine calibrated to have single crystal Si-1's peak be at 520.60 cm^{-1} .

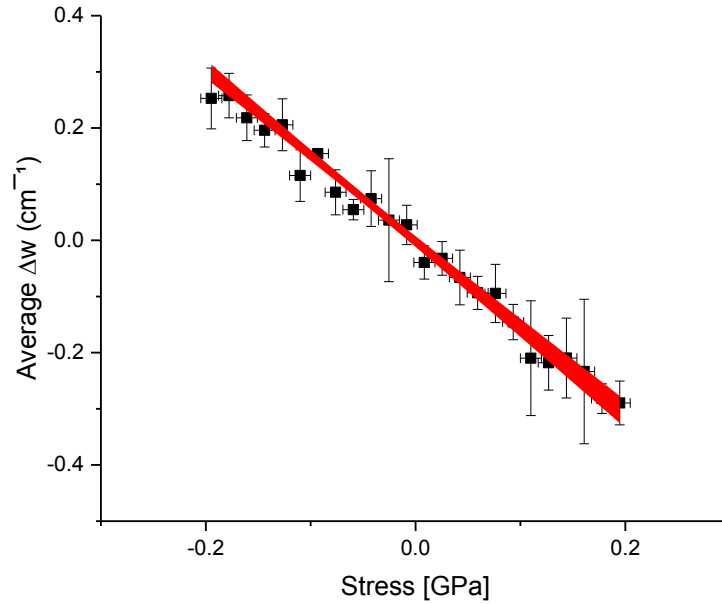


Figure 7.2: A sample plot of the data obtained for the 782 cm^{-1} peak of a $1\times1\text{mm}^2$ bar of YAG in four point bending under 11.07 N of force. The error bars vary due to how well polished the sample was at the exact location the Raman spectrum was taken.

The following table gives the coefficient of proportionality for the four peaks investigated, as well as the position of the peak at zero stress.

Table 7.2: The peak designation used throughout this work, the experimentally determined uniaxial proportionality coefficient, and the experimentally determined and used peak location at zero stress are shown.

Peak	C [$\text{cm}^{-1}/\text{GPa}$]	Zero stress

782	1.53 ± 0.05	782.49
402	0.82 ± 0.07	402.26
370	1.40 ± 0.16	370.57
260	0.63 ± 0.04	260.65

Application of results to grown fibers

Single crystal YAG fibers were grown via laser-heated pedestal growth (LHPG); following x-ray tomography the samples were examined under the Raman microscope in order to examine the potential residual stress in the fibers. Due to the complex crystal symmetry, an equation relating the total stress state to its hydrostatic and deviatoric components has not been developed. Because of this, the assumption is made that any residual stress in the fibers is deviatoric, rather than hydrostatic in order to simplify the analysis.

As the 782 cm^{-1} peak showed the greatest shift with stress, it was used to determine residual stress in several fibers. Additionally, as this peak is related only to the AlO_4 bonds, the proportionality coefficient will not be affected by the substitution of Y atoms for Nd atoms. The fibers were 5-29-14 undoped YAG, and 6-21-17 UP:YAG, and 1.5% Nd:YAG, referred to as 5-29-14, 6-21-17, and Nd:YAG hereon.

Fiber 5-29-14 had maps taken at different length scales to observe any changes in behavior with length. Over a large length scale, fiber 5-29-14 shows a small amount of

compressive residual stress with some variation on a local level (Figure 7.3). The overall residual stress is 52 ± 70 GPa.

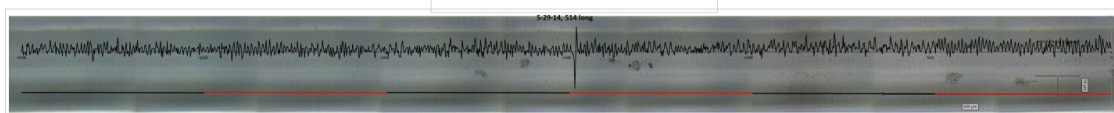


Figure 7.3: Full size figure available on request. A line map 3mm long was taken on fiber 5-29-14. The calculated residual stress is plotted on top of an optical image of the fiber taken in-situ with the built-in Renishaw camera.

On a local level, a map was made taking spectra every 1 micron in the x-direction and repeated at two more y- locations, 10 microns apart; the average peak position across the y-direction was taken to determine the residual stress (Figure 7.4).

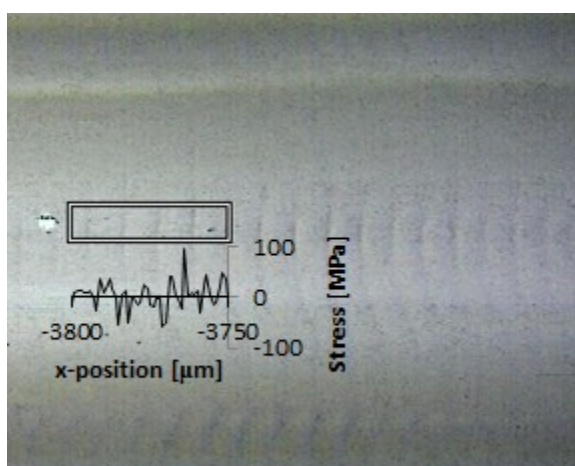


Figure 7.4: This micrograph of fiber 5-29-14 shows striations from the growth process; the white rectangle is the location the map was taken on this fiber. The calculated residual stress for every micron in the x-direction is given in the plot. The length of the map was 50μm.

The fiber 6-21-17 had similar maps performed on it. On a large length scale it shows an overall residual stress of 62 ± 21 MPa (Figure 7.5).

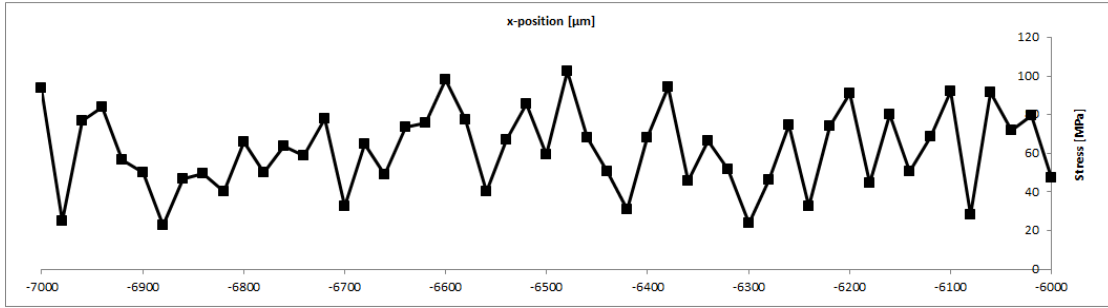


Figure 7.5: A map 1mm wide and 20 μm tall was made on an UP:YAG fiber. The spacing between spectra in the x-direction was 20 μm and the spacing in the y-direction was 10 μm . The average peak location in the y-direction was used when calculating the residual stress for this plot.

On the local scale, a similar map was performed (Figure 7.6).

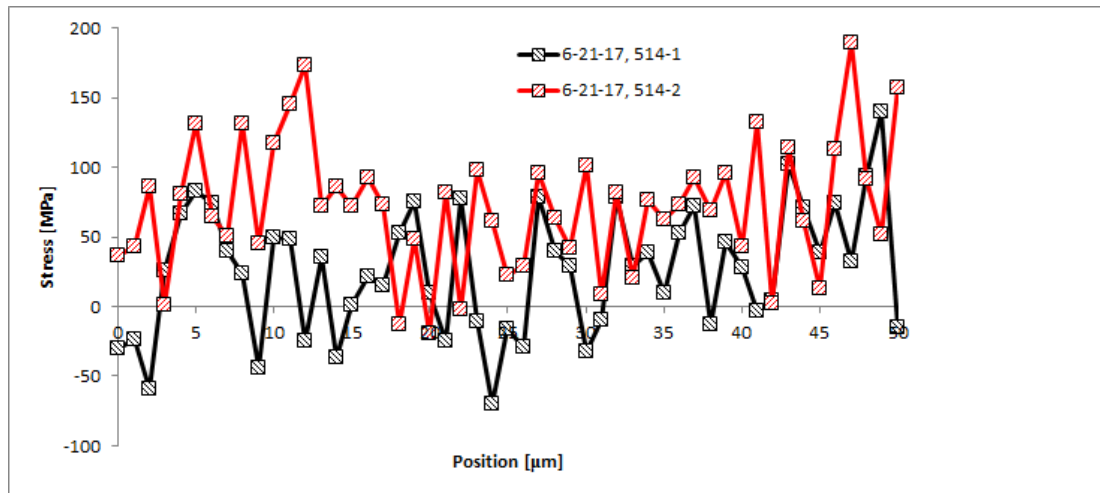


Figure 7.6: Two line scans were made in the x-direction, each taking a spectrum every micron. The line scans were separated in the y-direction by 10 μm . Some variation with position is visible, on roughly a 10 μm length scale.

Similarly, a fiber of 1.5% Nd:YAG was examined. A Nd:YAG single crystal source bar was also examined in order to obtain the correct zero-stress peak location for the 782 cm^{-1} peak, as the Nd atoms cause some shift in the exact location due to their size. The zero-stress location of this peak was found to be 781.58 cm^{-1} . Figure 7.7 and Figure 7.8 show the variation in stress different lengths on the fiber. The maps were not made in the same

location and this is reflected in the values seen as the position. The overall residual stress is low, 29 ± 113 MPa on the long map and 3 ± 116 MPa on the shorter map.

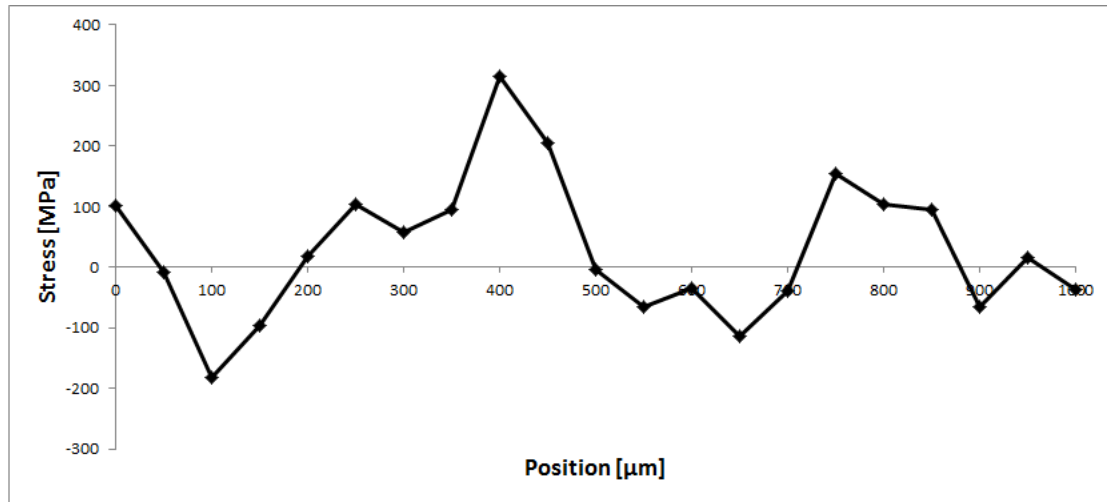


Figure 7.7: A line scan was made on the Nd:YAG fiber, one spectrum every 50 μm over 1 mm.

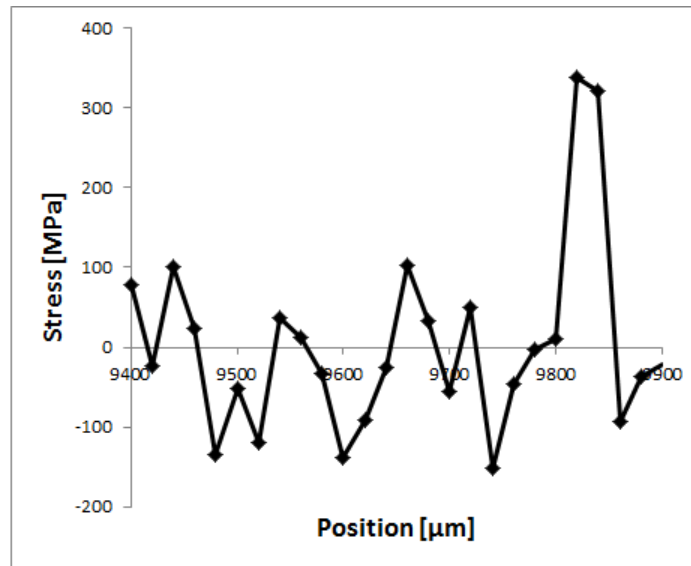


Figure 7.8: A similar line scan on a similar scale in a different location was performed. This scan took a measurement every 20 μm over 0.5 mm.

There are clear large-length scale variations with this fiber, with the length of variation on the order of 300 μm with an amplitude of ~ 100 MPa. On a more local level, the variation is not as intense, varying generally by 50 MPa on 40 μm length scales.

Conclusions

Relations between uniaxial stress and peak position for 4 tall (and thus easily fitted) peaks were successfully determined using a four-point bend device. These relations were then used to obtain an estimate of the residual stress in single crystal YAG fibers grown by LHPG. Due to the complicated crystal structure, a relation between the total stress state, hydrostatic stress, and deviatoric stress was not utilized; only the relation with respect to deviatoric stress determined above was used to obtain a value for the residual stress in the fibers. It was found that there is some variation in stress with position, but that the fibers overall are in a close to stress-free state, the average stress being 65 MPa or less. The undoped fibers tend to have slightly more overall residual stress than the Nd:YAG fiber, but the Nd:YAG fiber shows a larger variation with position and in amplitude than the undoped fibers.

References

- [1] E. Anastassakis, A. Cantarero and M. Cardona, "Piezo-Raman measurements and anharmonic parameters in silicon and diamond," *Physical Review B*, vol. 41, no. 11, 1990.
- [2] E. Anastassakis, A. Pinczuk and E. Burstein, "Effect of static uniaxial stress on the Raman spectrum of silicon," *Solid State Communications*, vol. 8, pp. 133-138, 1970.
- [3] I. De Wolf, "Micro-Raman spectroscopy to study local mechanical stress in silicon integrated circuits," *Semicon. Sci. Technol.*, vol. 11, pp. 139-154, 1996.
- [4] J. DiGregorio, T. Furtak and J. Petrovic, "A technique for measuring residual stress in SiC whiskers within an alumina matrix through Raman spectroscopy," *Journal of Applied Physics*, vol. 71, no. 7, pp. 3524-31, 1992.
- [5] S. H. Ward and A. B. Mann, "Four-point bend apparatus for in situ micro-Raman stress measurements," *Measurement Science and Technology*, vol. 29, 2018.
- [6] J. Aravanitidis, K. Papagelis, D. Christofilos, H. Kimura, G. A. Kourouklis and S. Ves, "High pressure Raman study of Y₃Al₅O₁₂," *physica status solidi (b)*, vol. 14, pp. 3146-3154, 2004.

- [7] S. Kostic, Z. Z. Lazarevic, V. Radojevic, A. Miltutinovic, M. Romcevic, N. Z. Romcevic and A. Valcic, "Study of structural and optical properties of YAG and Nd:YAG single crystals," *Materials Research Bulletin*, vol. 63, pp. 80-87, 2014.
- [8] M. Yoshikawa, K. Kosaka, H. Seki and T. Kimoto, "Stress Characterization of 4H-SiC Metal-Oxide-Semiconductor Field-Effect Transistor (MOSFET) using Raman Spectroscopy and Finite Element Method," *Applied Spectroscopy*, vol. 70, no. 7, pp. 1209-1213, 2016.

8 Feldspar and quartz

Feldspar and quartz were chosen to advance the work done with the four-point bend device described above for their incredibly broad range of uses where knowledge of residual stress could be of value. The relation between Raman peak movement and stress can be given as Equation 8.1:

$$\Delta\omega = -C \cdot \sigma \quad (8.1)$$

where $\Delta\omega$ is the wavenumber shift of a given peak in cm^{-1} , C is the proportionality coefficient (determined experimentally or through first-principles analysis), and σ is the stress in MPa or GPa. For most materials, the coefficient, C , is a positive number, indicating a redshift in the peak location with compressive stress and a blueshift with tensile stress.

8.1 Feldspar

Feldspar is not a singular material, but a group of materials with varying ions attached to a central group of atoms. The gross chemical formula may be given as $A(\text{AlSi}_3\text{O}_8)$, where A is Na, K, Ca, or some stoichiometrically correct blend of the three. Low albite, $\text{Na}(\text{AlSi}_3\text{O}_8)$, was chosen as it represents one end member of the group. Labradorite, $\text{Na}_{0.4}\text{Ca}_{0.6}(\text{AlSi}_3\text{O}_8)$, was chosen as a continuation of the Na-Ca spectrum. Anorthite, $\text{Ca}(\text{AlSi}_3\text{O}_8)$, was not investigated due to difficulty in procuring such a sample – it is a rare mineral that often is not found in large pieces.

Background

Building on the successful testing and use of the four-point bend device for in-situ Raman microscopy developed by Ward et al [134], two types of feldspar were investigated. One end member feldspar (low albite) and one mixed feldspar (labradorite, comprising of two end members) were chosen. The end member of albite is Na, whereas the end members of labradorite consist of Na 40% and Ca 60%, mixed randomly as the ion in Figure 2.20 [94] [96] [135]. These samples were cut from larger rock samples and polished to an acceptable size: 23 x 0.443 x 5.07 mm length x width x height for the albite sample and 23 x 1.362 x 5.23 mm for labradorite. Care was taken to align the crystal grain orientation with the direction of maximum stress as much as possible. Final polishing on the face investigated by Raman spectroscopy was done with a 1 μm grit size diamond lapping pad. Images of the samples are given in Figure 8.1.

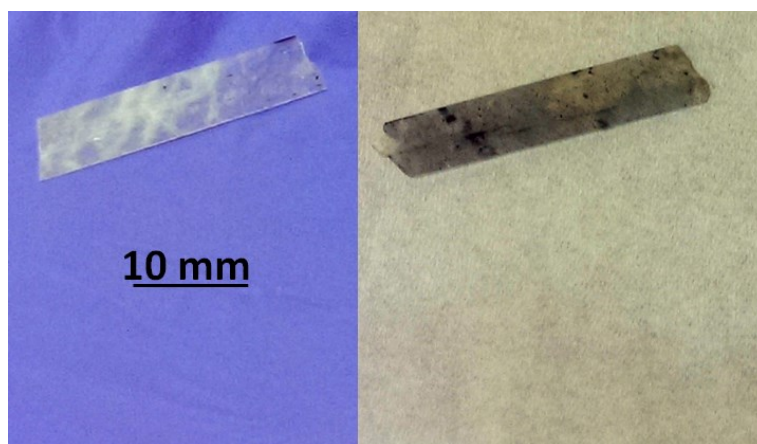


Figure 8.1: Albite is shown on the left and labradorite is shown on the right in this image. At this thickness, the albite is semi-transparent.

Several groups have reported on the origin of the different Raman peaks in various feldspars; the primary peaks investigated in this work were the 146 cm^{-1} , 290 cm^{-1} , and 480 cm^{-1} peaks. The 146 cm^{-1} peak arises from the overall compression-expansion of the

lattice parallel to the b axis, as shown in Figure 8.2. The 290 cm^{-1} peak arises from the rotation-translation of the 4-membered rings of tetrahedra. The 480 cm^{-1} peak arises from the ring breathing mode of the 4-membered rings of tetrahedra [101]. Very recently, another group investigated the peak shift with hydrostatic stress for selected samples of feldspar [135], building on prior experiments made with just albite [136]. Pertinent results from their study are given in Table 8.1.

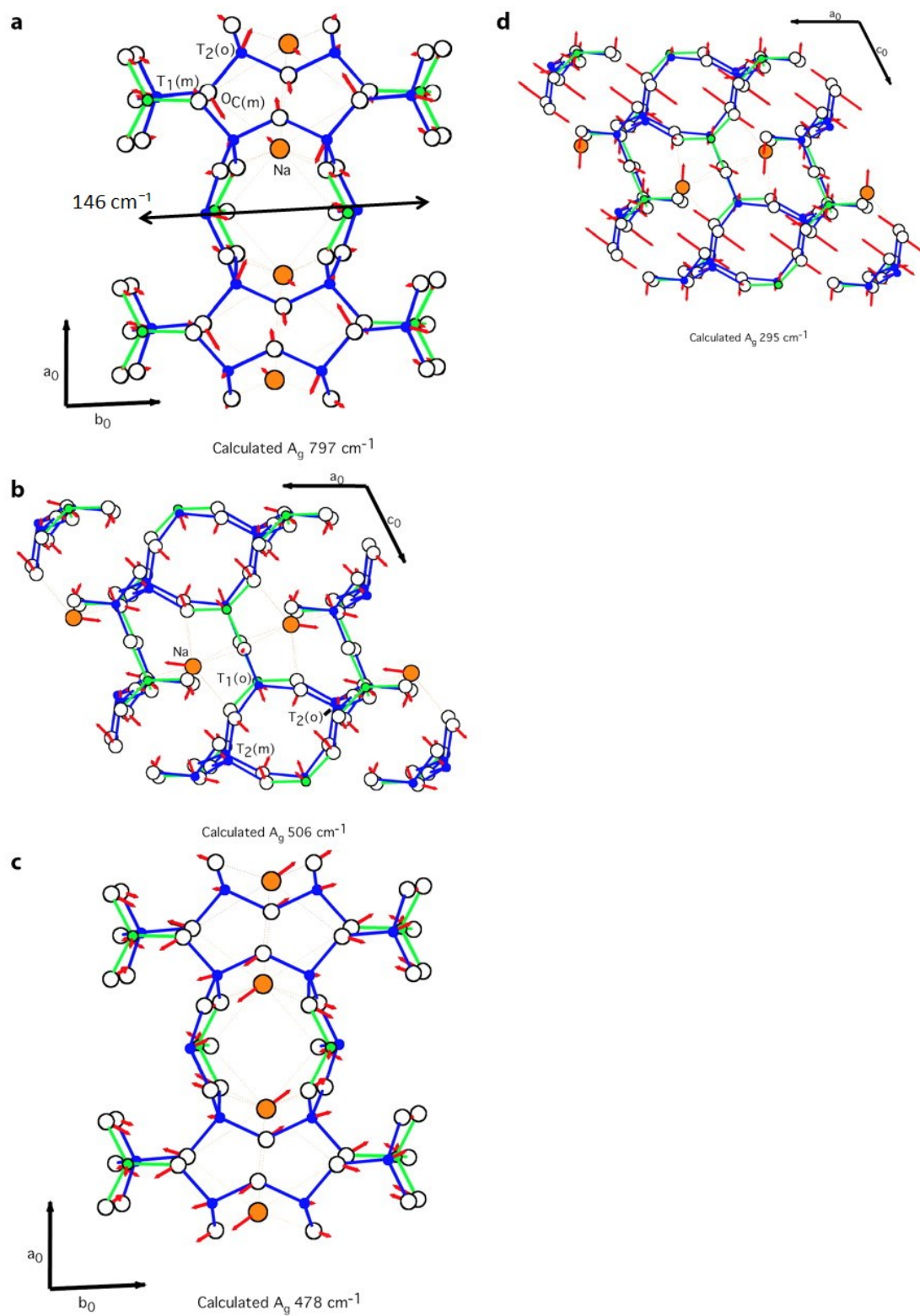


Figure 8.2: Raman mode assignment for selected vibrations of atoms in albite. Image from [137].

Table 8.1: Published results for the 480 cm⁻¹ and 290 cm⁻¹ peaks in albite and labradorite under high pressure are presented [135].

Sample	Peak	C [cm⁻¹/GPa]
Albite	480	4.2±1.2
Albite	290	2.4±0.4
Labradorite	480	3.9±1.2
Labradorite	290	2.6±1.9

These results are all for a pressure of 3.6 GPa or less. Above this pressure, the relation changes for albite – at varying pressures above 3 GPa, the relation between peak shift and pressure has discontinuities at various pressures [136]. This is likely due to rearrangement of the atoms as the pressure increases; the observed changes are fully reversed on decompression.

Results

This experiment examined the effects of uniaxial stress on the Raman spectra of albite and labradorite. Each sample tested was polished with a 14 micron particle size diamond lapping pad on the tensile and compressive faces and with a 1 micron particle size diamond lapping pad on the top and bottom faces. The labradorite sample exhibited poor edge quality, limiting the map range to a span of 700 μm out of a total width of 1362 μm . The majority of this useable surface was on the compressive side of the sample. The albite samples had flat, even surfaces perpendicular to the incident laser beam over the whole width.

The 510 cm^{-1} peak of labradorite was investigated in addition to the 480 cm^{-1} peak as it is another sharp, clear peak and the 290 cm^{-1} peak is broad and not easily fitted (Figure 2.22). Neither peak showed an appreciable and distinct shift with stress when the 633nm laser was used, but both showed a marked shift under the 514nm laser (Figure 8.3).

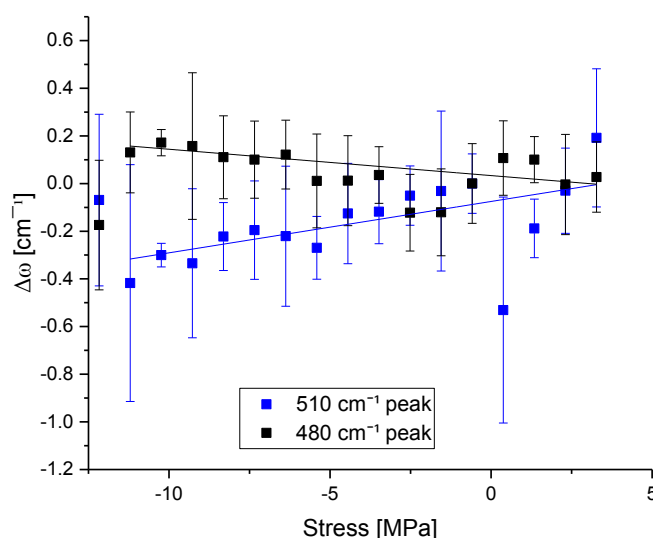


Figure 8.3: An example of the data taken from labradorite under a load of 12.15 N. Note that the 510 cm^{-1} peak shows a shift in the opposite direction of what is typically expected of materials. Data was taken with the 514 nm laser.

The relation between peak shift and stress in labradorite in this experiment, with a 514 nm incident laser, is $C_{(510)} = -22 \pm 4\text{ cm}^{-1}/\text{GPa}$ and $C_{(480)} = 11 \pm 4\text{ cm}^{-1}/\text{GPa}$. The R^2 values of these coefficients are poor, 0.64 and 0.37, respectively.

More intriguing are results obtained from observing the peak shift in albite with stress. In addition to the 290 cm^{-1} and 480 cm^{-1} peaks, the 146 cm^{-1} and 510 cm^{-1} peaks were observed to shift with stress; the latter being sharp and distinct and the former shifting by a significant amount. Table 8.2 provides a summary of the peak location, relation with stress, load, and laser used to interrogate the first albite sample.

Table 8.2: The relation between uniaxial stress and Raman peak shift for four different peaks at two different loads and two different lasers in albite.

Peak [cm ⁻¹]	C [cm ⁻¹ /GPa] 5.3 N	C [cm ⁻¹ /GPa] 7.5 N	Laser λ [nm]
146	6.3	3.1	514
146	-12.6	-9.9	633
290	1.7	-1.7	514
290	-1.9	-0.1	633
480	-3.2	-1.8	514
480	-3.7	-1.8	633
510	0.4	0.4	514
510	-0.1	-0.8	633

Of interest is that with the exception of the 510 cm⁻¹ peak, there is a reduction in the proportionality coefficient with increasing stress. It is hypothesized that this might be due to slow crack growth occurring throughout the second map (at higher load) of the sample. Examination of the 146 cm⁻¹ peak, although not conclusive, adds evidence to this theory as seen in Figure 8.4.

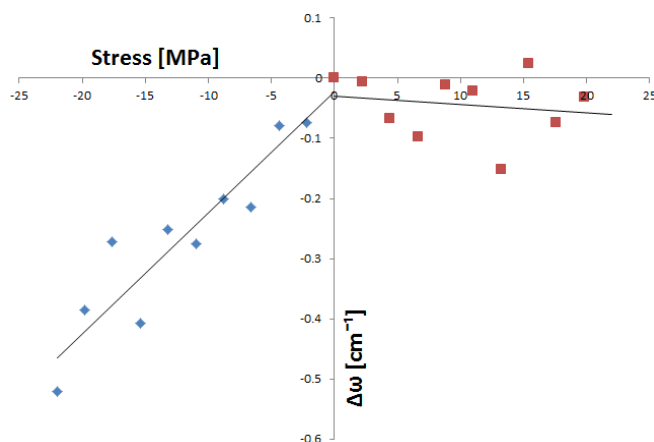


Figure 8.4: The 146 cm^{-1} peak exhibits a sudden transition from $C=-20\text{ cm}^{-1}/\text{GPa}$ to $C=1.3\text{ cm}^{-1}/\text{GPa}$ near the neutral axis. This behavior indicates that something changed, possibly slow crack growth occurred, and possibly there is a real difference in the relation between Raman peak shift and stress in tension.

The second sample of albite tested was thinner and thus able to strain further before cracking, despite not being able to go quite as high a stress. The sample broke on a cleavage plane located at a loading pin in the four-point bend set-up. A map at only one load was accomplished for both lasers, during the second load with the first laser, the sample failed. Table 8.3 gives the compiled data at the lower load.

Table 8.3: The relation between peak shift and stress is given for 4 peaks at two different laser wavelengths for a different sample of albite. A value of ‘null’ in the coefficient column indicates that the points were randomly distributed and no meaningful relation could be established.

Peak [cm^{-1}]	C [$\text{cm}^{-1}/\text{GPa}$] 0.83 N	Laser λ [nm]
146	null	514 and 633
290	null	514
290	-5.5 ± 1.1	633

480	-9.2	514
480	-8.2 ± 1.3	633
510	null	514
510	-6.5	633

Values of ‘null’ indicate randomly distributed data; an example of this is given in Figure 8.5.

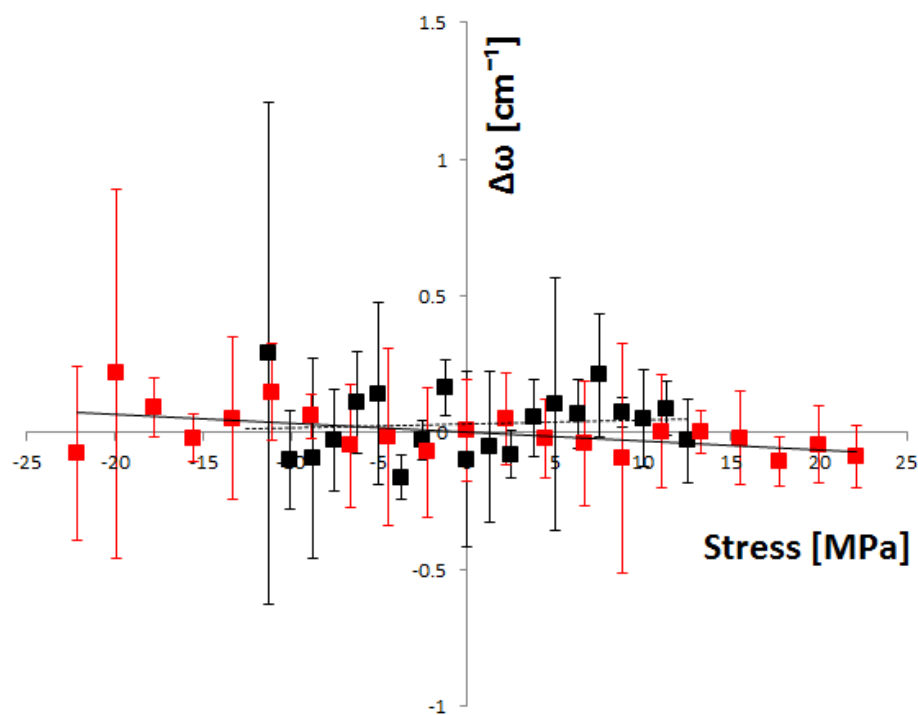


Figure 8.5: The 148 cm⁻¹ peak exhibits a very high distribution of peak shift, the black squares indicating the values taken at a load of 0.83 N and the red squares indicating values taken at a load of 1.47 N.

A fit to the above data is technically possible, however, the R^2 is extremely low, $R^2=0.01$ for the low load data and $R^2=0.30$ for the higher load data.

In the higher load map a change in the relation between peak shift and stress is seen again near the neutral axis, but unlike with the first sample, the peak exhibiting this behavior is the 480 cm^{-1} peak. This is shown in Figure 8.6.

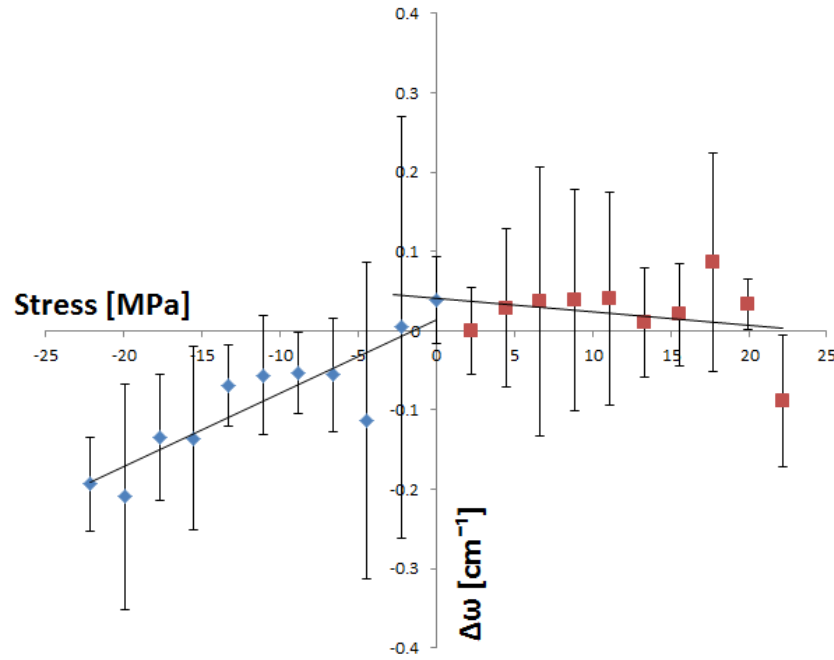


Figure 8.6: A marked change in the relation between the 480cm^{-1} peak location and stress is obvious in this figure. As before, it could be due to cracking in the sample, or it could be an actual change in the proportionality coefficient.

The proportionality coefficient of the 480 cm^{-1} peak on the compressive side is $C=-9.2\text{ cm}^{-1}/\text{GPa}$, whereas on the tensile side it is $C=1.6\text{ cm}^{-1}/\text{GPa}$.

Discussion and Conclusions

Negative values of C are unusual and initially do not make any sense, indicating the data is wrong; however, over multiple samples and peaks this trend is visible, indicating that the experiment was properly performed and the data is correct, so something else must be going on. Recall that feldspar is primarily made of Al- and Si- centered tetrahedra which

are connected by the oxygen atoms (Figure 2.20 and Figure 8.7). Under uniaxial loading, as performed here, these rings of tetrahedra have the ability to deform, rather than just compress as happens under hydrostatic loading. A directional pulling (tensile stress) could cause the rings to flatten out relative to each other, causing the groups of rings to become more planar in shape. This distortion would heavily influence the peaks which arise from the vibration of the rings, notably the 290 cm^{-1} peak (rotation-translation of the ring) and 480 cm^{-1} peak (ring-breathing mode) [135] [136]. Figure 8.7 shows the direction of maximum compressibility under hydrostatic loading; of note is that unlike in silicon, YAG, or silicon carbide, the structure is very non-planar, rendering much heavier distortion in one direction than the other directions [138] [139]. All this comes together to suggest that in bending, the peak shifts of feldspar may not behave as expected, and even at high pressure, some peaks have a similar behavior [139], as shown in Figure 8.8.

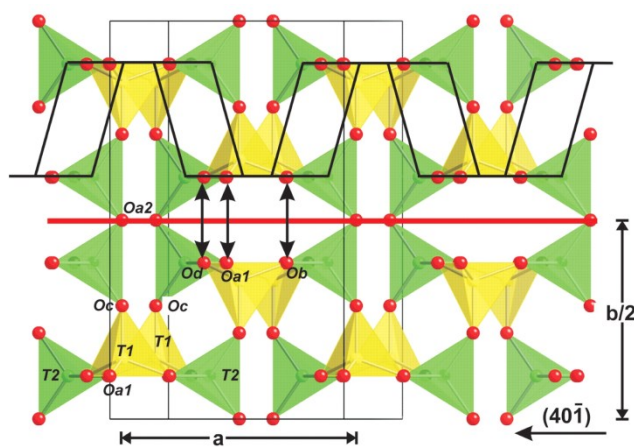


Figure 8.7: The so-called “crankshaft chain” is given as the black overlays; this chain, despite the generally isotropic nature of the crystal, behave highly anisotropically under stress, being far more compressible in the $(1\ 0\ 0)$ direction than other directions [139].

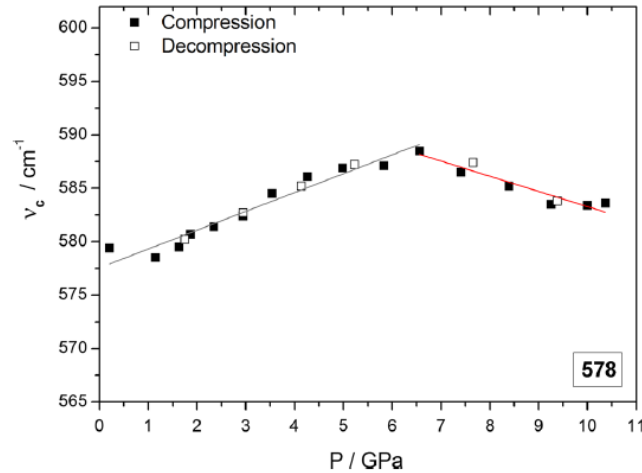


Figure 8.8: Under hydrostatic loading, the 578 cm⁻¹ peak (not examined in this work) shows a sharp change in peak shift relative to stress at 6.5 GPa; the proportionality coefficient in this case turns sharply from positive to negative. Image from [136].

Aside from being an interesting system with properties that are not yet fully understood, there are practical applications to determining the relation between Raman peak shifts and stress. The residual stress in a material can tell us about its history and in cases where a feldspar crystal is trapped inside another crystal, the measured stress of the trapped crystal is the same as stress it was under when it was first encased, giving a look into the exact pressures and processes going on in the earth [140] [141] [142]. Further, considering how important feldspars are in ceramics, knowing the stress state of feldspar after firing is important in determining how to better process the ceramic.

8.2 Quartz

This study utilized four-point bending to closely examine the relation between peak shift and stress uniaxially in quartz; because quartz is trigonal, multiple orientations were examined to study if there were any differences in behavior between orientations. Both

the 514nm and 633nm laser were used in this study; the 633 obtained a slightly greater penetration depth than the 514, but surface roughness affected the results from both lasers.

Background

Several groups have examined the relation between hydrostatic stress and Raman peak shift in quartz, with an particular focus on the 128cm^{-1} , 206 cm^{-1} , and 464 peaks cm^{-1} [143] [144] [145]. The high relative intensity of these peaks along with the fact that at zero stress they are quite far apart and distinguishable makes them ideal for examining stress in silica. The 206 peak varies non-linearly with stress, having a relation of $\sim 24\text{ cm}^{-1}/\text{GPa}$ below 0.5 GPa and $\sim 11\text{ cm}^{-1}/\text{GPa}$ between 1.5 and 2.15 GPa (Figure 8.9); the average coefficient of proportionality (hydrostatic) is given along with the coefficients for the other peak in Table 8.4.

Table 8.4: The proportionality coefficient for studied peaks is given. The relation for the 128 peak is an average value as it has a non-linear relation with hydrostatic stress. Data estimated from [144].

Peak [cm^{-1}]	C [$\text{cm}^{-1}/\text{GPa}$]
128	5.12
206	19
464	8.4

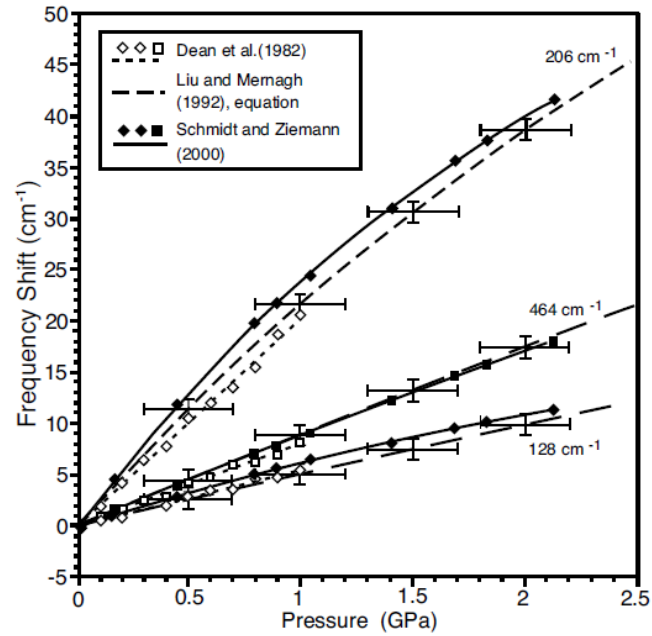


Figure 8.9: The graph from which the proportionality coefficients were determined is a composite of data from several researchers, compiled by Masuda et al [144]. Of note is the distinct non-linearity of the 206 cm⁻¹ peak.

A wafer of quartz single crystal grown from a seed was procured from University Wafer [146]. The wafer was ST cut at 42.75° from the y-axis with rotation about the x-axis [147] [148] [149] (Figure 8.10).

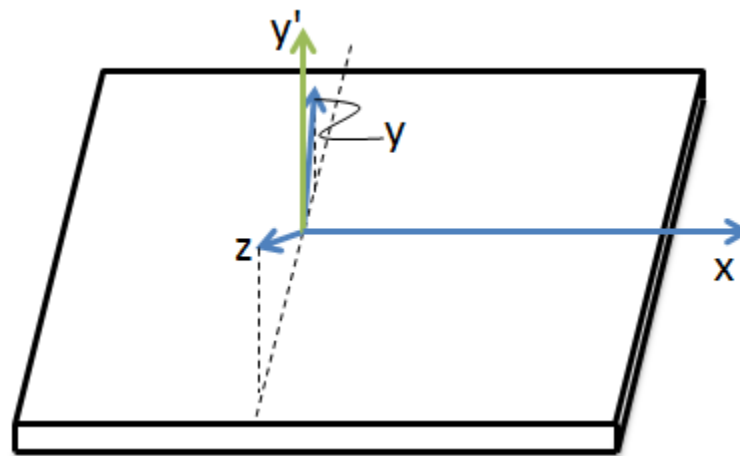


Figure 8.10: The cardinal directions on a cut wafer are as shown here. The direction y' indicates the direction normal to the wafer surface. The angle between the y' -axis and the y -axis is 42.75° for ST-cut wafers.

Results

Three sample orientations chosen: parallel to the wafer flat, perpendicular to the wafer flat, and 45° from the wafer flat (Figure 8.11).

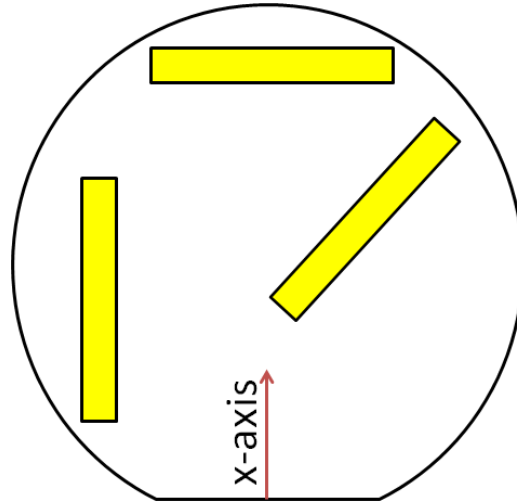


Figure 8.11: The wafer flat (bottom) is commonly used as a reference point for orientation. Three orientations were chosen, the long edge (the edge perpendicular to the incident laser beam) is used as the reference edge for the samples. The samples were designated as perpendicular to the flat (left rectangle), parallel to the flat (top rectangle), and 45° from the flat (angled rectangle).

Throughout this work, the orientations will be referenced as the perpendicular, parallel, and 45° samples. Using common 3-axis notation, the orientation of a crystal can be given as $(1\ 0\ 0)$. This work utilizes decimals to simplify directions that are not easily made into fractions. The direction of the tensile stress and orientation relative to the laser for each sample is given below (Table 8.5).

Table 8.5: The direction of tensile stress for each sample is given, as well as an orientation relative to the incident laser beam.

Sample	Direction of stress	Axis relative to laser beam
Perpendicular	x-axis $(1\ 0\ 0)$	y-axis is 42.75° from parallel to incident laser

Parallel	y- and z- axes (0 0.73 0.68)	x-axis is parallel to incident laser
45°	x-, y-, and z- (1 0.73 0.68)	rotate direction of stress 90°

Each orientation broke at a different load; this is most likely due to differences in edge quality (it increased with sample number) and not the orientation of the samples themselves. The proportionality coefficient for each orientation at each laser wavelength is given in Table 8.6; the 206 cm^{-1} peak had the same relation no matter the orientation, thus only the difference in laser is considered.

Table 8.6: The proportionality coefficient found by experiment for each peak at a given orientation and laser wavelength is given.

Peak/orientation	C [$\text{cm}^{-1}/\text{GPa}$], 514 nm	C [$\text{cm}^{-1}/\text{GPa}$], 633 nm
128		
<i>Parallel</i>	2.0±0.2	2.1±0.3
<i>Perpendicular</i>	4.6±0.1	3.1±0.8
45°	0.9±0.1	1.3±0.1
206		
<i>All</i>	8.7±0.7	8.2±0.3
464		
<i>Parallel</i>	3.2±0.2	2.6±0.2
<i>Perpendicular</i>	2.6±0.1	2.4±0.1
45°	2.2±0.1	2.4±0.1

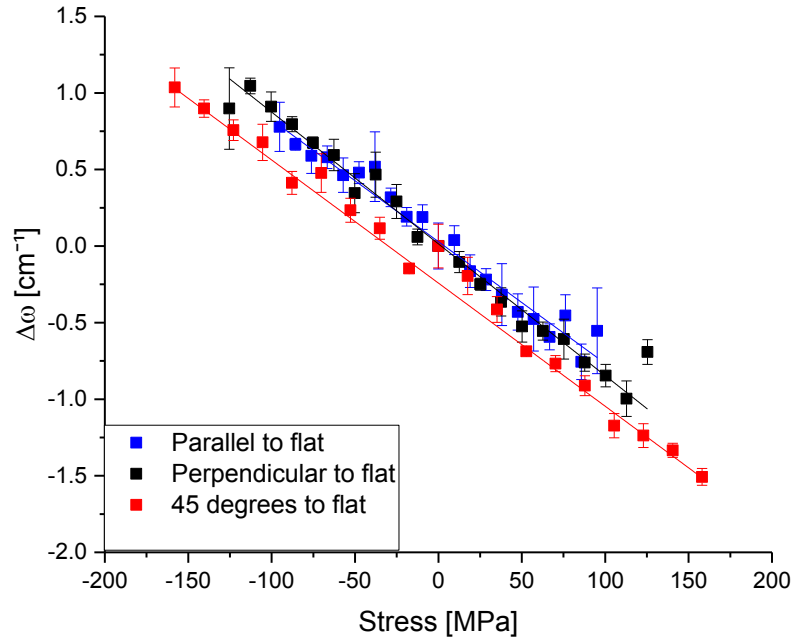


Figure 8.12: The linear relation between stress and Raman peak shift of the 206 cm^{-1} peak with the 633nm laser incident on the sample is demonstrated here. The offset between the lines in the y-axis is due to taking the average of the points near the neutral axis as zero stress even if they are not giving a Raman shift in agreement with that due to surface flaws altering the Raman spectra.

The 206 cm^{-1} peak has no dependence on orientation or laser wavelength (Figure 8.12); discrepancies between the two lasers can be attributed to flaws in the surface finish affecting the Raman signal. Examining the 464 cm^{-1} peak, there is no significant difference in the proportionality coefficient between orientations when using the 633nm laser; however, this does not seem to hold true for the 514nm laser. The error bars for this peak at each stress level were quite high (especially when compared with the error bars for the 206 cm^{-1} peak), despite the overall good fit. Further, during examination of the 128 cm^{-1} peak, there is a strong dependence on orientation, with the highest proportionality coefficient for the sample perpendicular to the wafer flat, near zero at 45° to the wafer flat, and $\sim 2\text{ cm}^{-1}/\text{GPa}$ when parallel to the wafer flat (Figure 8.13).

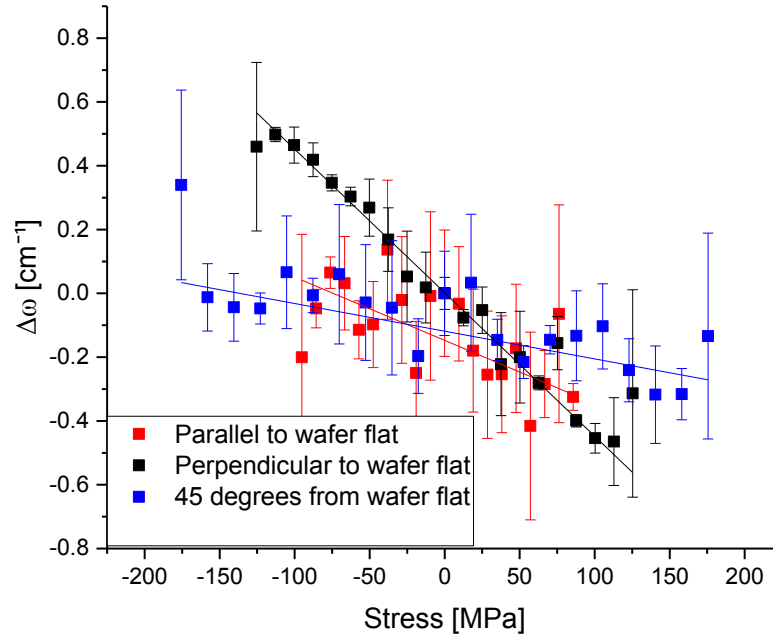


Figure 8.13: The linear relation for each orientation for the 128cm^{-1} peak with the 514nm laser incident on the sample.

Conclusions

This study sought to investigate the relation between uniaxial stress and Raman peak shifts in quartz with knowledge that orientation of the crystal may be important. This was successfully done using the four-point bend device developed by Ward et al [134]. This test gives new insight into the study of residual stresses and is especially pertinent to the semiconductor and ceramics communities as quartz is far more likely to fail in tension than in hydrostatic or uniaxial compression, which is what several prior groups have investigated for mineralogical and geological purposes. Orientation of the crystal matters greatly for the 128 cm^{-1} peak due to the fact that it is a degenerate peak made of both the transverse optical phonons and longitudinal optical phonons. At different orientations, these will be stronger or weaker. The 206 cm^{-1} peak is orientation-independent due to

being an acoustic mode, and has the strongest relation out of the peaks investigated, with $C=8.7\pm0.7\text{ cm}^{-1}/\text{GPa}$. The 464 cm^{-1} peak is also orientation independent with $C=2.5\pm0.2\text{ cm}^{-1}/\text{GPa}$, arising from the same acoustic mode as the 206 cm^{-1} peak. This peak is more sensitive to surface clarity, with improved error bars with better polished samples.

9 Conclusions

When this project was first begun, the goals were simply to develop one or more mechanical test methods that could give insight into the behavior of ceramics. The first of these developed was the four-point bend device for *in-situ* Raman spectroscopy; the lessons learned about the simplicity and power of bend testing here were applied when a second project – characterization of the mechanical properties of silicon carbide fibers – presented itself.

Characterization of silicon carbide fibers

Silicon carbide fibers grown by Free Form Fibers LLC via laser-induced chemical vapor deposition were probed by a variety of methods not otherwise available to Free Form Fibers (FFFibers). The first of these, instrumented indentation, produced interesting results about the outside surface of the fiber – the reduced elastic modulus and hardness were both much lower than expected for silicon carbide but significantly higher than for pure silicon. Prior work by FFFibers had shown that the outside layer of the fibers was composed of amorphous silicon; nanoindentation data showed that the mechanical properties of this layer were greater than could exist in pure a-Si. The hypothesis that this layer was carbon rich was validated under micro-Raman spectroscopy due to the presence of a signal from amorphous SiC. It was not possible to quantify the amount of SiC in the outside layer, but only show that it existed. A distinct phase change was found to exist between the inner core of the fiber and the outer layer; this was most apparent with micro-Raman spectroscopy and helium-ion microscopy (HIM) on the cross-section of the

fiber. There was no significant intermixing of the outer layer and inner core, even when viewed with the HIM.

Many attempts to quantify the reduced elastic modulus and hardness of the core of the fibers were made; most of these were unsuccessful due to the high stiffness of the fibers relative to any mounting medium used. This issue was finally addressed by adding several fibers to a pellet of glass powder and sintering the compacted mass. Cutting and mounting the resulting pellet revealed the cross-section of the fibers; this was remounted onto a solid steel substrate and polished with diamond lapping pads – diamond slurry was found to preferentially abrade any material that was not the silicon carbide fiber. Instrumented indentation of the cross section of a fiber was possible and showed that the core had a reduced elastic modulus of 300 ± 30 GPa and hardness of 30 ± 4 GPa.

While testing with various mounting methods for nanoindentation was being carried out, several test methods involving bending the fibers were investigated, the large-deflection cantilever beam method being the most robust method developed. This method was developed when it was noted that the fibers were extremely flexible, but too fragile without a coating to be tested with a two-point bend testing method [150]. Several iterations of mounting procedure were performed until the sandwich method with epoxy proved to be the best method. Following this, the test was quite simple to perform and analysis of non-linear elastic deformation was carried out. It was found that using a guessed modulus of elasticity and plotting a model curve with that modulus against the real deflections, then adjusting the guessed modulus to better fit the real data was the best

method for obtaining a value of the overall elastic modulus of the fibers. The fibers were shown to vary across batches, with high-quality fibers having an elastic modulus of 330 ± 5 GPa. The development and validation of a new testing protocol for high-elastic modulus fibers on this length scale was one of the primary achievements of this project.

At no point during electron microscopy of fiber cross-sections did the fibers ever show inclusions or voids, despite these being incredible stress concentrators and the most likely locations for failure to initiate. Although this is not complete proof that the fibers are fully dense and uniform, the lack of evidence of flaws indicates that the fibers are fully dense and uniform.

Fractographic analysis was performed on several fibers, the majority of which had been broken in bending. The majority of failure surfaces investigated either had no discernible origin or began on the outside of the fiber, which is expected in bending. Multiple fibers were broken while adhered to a piece of carbon tape in an attempt to capture both sides of the fracture surface; despite this, not all fracture surfaces matched up. Several fibers showed what could only be secondary fracture as the fiber vibrated from the shock of the first – a trait that strong and stiff materials share in common. Advanced analysis of the fracture mirrors was performed in order to obtain an estimate of the stress the fiber failed at. Constants obtained for similar materials (SiC fibers) were used in this estimation and it was discovered that the fibers tend to fail at 2.16 ± 0.13 GPa, a slightly lower stress than comparable fibers grown by commercial companies fail at. This value is tempered by the

fact that the mirror constants used were not for these exact fibers, but fibers grown by a completely different process.

Four point bend testing

Alternating with this research was the lasting part of the first project – use of the developed four-point bending device. Development and validation of the device, as well as documenting the science and theory behind it opened up several possible avenues of research, only a few of which were able to be performed due to time constraints. Originally tested with silicon (a well-studied baseline material), the device was used to examine the relation between stress and Raman peak shift of single-crystal 4H-SiC. Several materials were considered for further testing on the device, including gallium arsenide, germanium telluride, quartz, yttrium-stabilized zirconia, calcium carbonate (calcite), feldspar, and yttrium aluminum garnet. Only a few of these materials were able to be successfully tested, the others either being difficult to procure in large single crystals (GeTe, feldspar) or extremely difficult to prepare (GaAs, calcite, feldspar). Feldspar was not procurable in large single crystals; however, it is common and does have crystals large enough that the Raman microscope can examine only one crystal in the device; this polycrystallinity may have led to the early fracture of the feldspar samples during testing. Further, preparation of feldspar from rock samples proved to be quite difficult – uniformly thinning down a cut sample to wafer thickness and dimensioning it correctly resulted in many half-polished, broken samples.

Each material tested outside of Si and SiC demonstrated that such testing is needed on yet more materials: the acoustic peaks for quartz being orientation independent and the degenerate TO+LO peak showing a strong orientation dependence, YAG showed a dependence on the doping ion (Nd) and a distinct difference in the proportionality coefficient to the published values when tested against hydrostatic stress, and the feldspars tested showed strong discontinuities in the proportionality coefficient not just in this test but also under hydrostatic conditions.

10 Broader implications and Future work

Characterization methodology

Improved methods of characterizing the mechanical properties of silicon carbide fibers were developed in this work, focused primarily on the mounting procedures used for nanoindentation studies and cantilever beam methods for determining the elastic modulus of the entire fiber. Although these were improved and developed specifically for silicon carbide fibers, the methods can be broadly applied to most ceramic and glass fibers. Any non-oxide ceramic fiber with a melting point substantially above the sintering temperature of glass can be sintered into a stiff CMC with reduced concerns related to the flexure or movement of the fiber in the matrix. This process is especially good for examining single fibers, important when new fibers are being developed and cannot be produced in a large enough quantity to create tows. By polishing with a diamond lapping pad rather than a diamond paste, there is a reduced risk of damaging the edge of the fiber prior to indentation of the cross-section, as seen in the helium-ion micrographs. Although glass fibers cannot be sintered into conventional glass powders, there are ultra-low

temperature sintering materials in which they could be placed and sintered without modifying the properties of the glass [151]. This would allow the same procedure as developed in this work to be used to obtain the hardness and reduced elastic modulus across the cross section of glass fibers; this could be of great interest to the fiber optics community with regard to graded index fibers.

The large deflection cantilever bend method developed to determine the elastic modulus of the fibers is immediately applicable to any fiber of any material – so long as the fiber can be firmly clamped and a reasonably good image with known scale in the background can be taken, there are no special requirements to perform this test. Again, it is only applicable to individual fibers, but the range of fibers which can be tested is quite large, going from organic fibers such as hair to high-modulus fibers as demonstrated in this work. This method has the advantage of not relying on precise alignment of loading to work, unlike tensile testing. The reduction in cost of equipment, time, and concern about off-axis loading leading to early failure of the fiber are all advantages of this method that are applicable to many other fibers.

As new fibers of novel compositions or processes are developed, these methods will allow for a more thorough characterization of the mechanical properties of the fibers – these properties being among the most important reasons for the development of new fibers. The large deflection cantilever method could be readily modified to be performed in-situ at elevated and depressed temperatures, granting greater insight into the properties of the fibers outside of standard temperature and pressure.

Although several new test methods and sample preparation procedures were developed during the course of the partnership with Free Form Fibers, there are still questions. The fracture mirror constants used to calculate the stress at fracture were from fibers grown via a completely different method and only serve as good approximations for the mirror constants in the fibers made by FFFibers. Tensile and bend testing with constant load monitoring would determine the stress at failure of the fibers; by examining the broken fibers under an electron microscope the mirror constants for these fibers could be determined and applied to future fibers made by FFFibers [152]. The fracture toughness of these fibers may be higher than for comparable commercially available fibers, thus determination of the fracture toughness should be performed to quantify this value.

Free Form Fibers SiC fibers

The tests performed in this work show that the SiC fibers produced by FFFibers perform comparably to other commercially available SiC fibers produced by other methods. From nanoindentation on the outside of the fibers, it is known that the carbon-rich amorphous silicon outer layer exhibits ductility; it is likely that this adds to the fracture toughness of the fibers as the ductility on the outside of the fiber (where stresses are generally the highest) causes more energy to be expended during fracture of these fibers than for comparable commercially available fibers. Fractography backs this up to an extent, where it was observed that the tensile side of fibers broken in bending had multiple cracks in the outer layer near the region where fracture actually occurred. Tests to determine the actual fracture toughness of these fibers should be carried out. Another difference between these

fibers over many commercially available fibers is that there is no separate core – many fibers have a carbon core that the silicon carbide is deposited around, whereas the fibers produced by FFFiber are completely silicon carbide except for the outermost layer [153]. Since SiC is deposited onto the surface of the core, there is the possibility that voids or inclusions may be present, weakening the fiber overall. Other methods of fiber production, such as polymer impregnation and pyrolysis can result in unreacted precursor material, also weakening the fiber overall. The production process used by FFFibers avoids these issues.

Further development of cantilever bend testing should be done – it currently is most suitable for longer fibers due to the mounting process; alternative, more rigid mounting procedures need to be developed to allow for use of the instrumented indentation as the loading mechanism on a cantilever fiber. All of the literature that has been found regarding using instrumented indentation on cantilever beams has been for beams cut from a thin film that had been applied to a substrate or directly cut from the substrate, never from a beam attached to the substrate [154] [155]. An issue in attaching the fiber is that in order to prevent delamination, it must be sandwiched, but the height of the material sandwiching the beam will come into contact with the indenter tip at distances that are too close to the clamped end of the beam. This could be solved with a superior method of attaching the fiber to the substrate.

Four point bending

The four-point bend device developed for in-situ microRaman measurements was successfully validated and used. The use of this machine allows for a stress-peak shift calibration curve to be obtained for a wide variety of important materials, some of which were explored here. As seen in the compilation of different C values for SiC, there is contention regarding what the correct relation is. This device allows for a direct, experimental method to determine this relation. The application of this device to yet more materials provides insight into the behavior of the materials and more importantly, with the calibration curve, allows for the quantification of the residual stress in a processed material. Doing so, improved processes may be developed that reduce the residual stresses or impart more compressive stresses on the surfaces of the materials, increasing the longevity of the processed item.

The primary advantage of Raman spectroscopy over other methods is its speed – maps over a processed surface can be obtained within hours and processed rapidly to determine the residual stress in the material. Even the calibration curves can be obtained with rapidity, the typical time to find to find the relation between peak movement and stress being 3-5 days of work, with reliable results as the end product, assuming preparation of the sample was done properly. This rapidity of both mapping the surface of a processed material and of determining the coefficient of proportionality creates the opportunity for many materials and orientations to be tested for use in industry.

More orientations of the quartz crystal need to be examined under the microscope, as all orientations chosen were based on an ST-cut wafer. Other cuts of wafer exist that are

suited for higher stress applications or different RF devices [149], and starting with one of these orientations would allow for more information to be gathered. Additionally, it would be of great interest to the ceramics and mineralogical communities to examine natural quartz and determine if there is a significant difference between natural and artificial quartz crystal behavior with stress (as can be measured with Raman spectroscopy).

Feldspar, being a natural mineral does not necessarily behave the way it is expected to in the lab. Because of this, further testing of both albite and labradorite is warranted, as each showed an unexpected Raman peak shift, especially on the tensile side of the sample. The shift in position of a peak is not the only way to analyze the obtained data. Examination of the peak width, height, and area may reveal more than simple peak shift for a system as complex as feldspar. Additionally, these are not the only types of feldspar. Other end-member feldspars should be tested (microcline, anorthite) as well as several of the solid-solution mixes of the end-members – labradorite is one such example of several just on the Na-Ca end-member group. The exact mechanism behind the behavior has been deducted experimentally, but not validated theoretically here; this should also be done as part of the characterization of feldspars.

An important material that is known to have polyhedra structures similar to feldspar is boron carbide, a ceramic used for making armors. There has been difficulty in determining the residual stress in machined boron carbide ceramics due to this crystal structure. By examining this related system (feldspar), we have gained insight into the

possible relation between stress and peak shift in boron carbide. As determined with work on feldspar, peak position may not be the only measureable quantity that is related to stress – peak height and the peak width at the full width, half maximum (FWHM) may be related to stress as well. Directly obtaining the relation between stress and peak shift (and width and height) for boron carbide with this method could be of great benefit to the armor community.

Many more important materials can and should be examined for a relation between Raman peak positions and uniaxial stress – such experiments have been carried out on a number of materials under hydrostatic stress but those results cannot easily be extrapolated to tensile stress and cannot be extrapolated to deviatoric stresses.

Investigation of the peak shift with stress is not the only use of this device however. Creating a small scratch on the tensile surface of a specimen and carefully applying a load in the device would allow for the investigation of changes in Raman signal near a crack tip. Some materials, such as YSZ, undergo a phase transformation with stress; Raman spectrometers have the capability to determine what phase a material is (just as what polytype a material is) based on the changes in bonding. In-situ examination of crack tip phenomena in such materials and other materials would be of supreme interest to the world of materials science as in-situ testing with other instruments, such as x-ray sources, is much more complicated and time consuming than Raman spectroscopy is.

Appendix 1 – MATLAB code, Equation 8

MATLAB code used for the numerical solvation of q in Equation 8.

```
clc

%give y-values for an array of phi

%b=%angle at a chosen point

b=0.5

for phi=0:0.025:0.5;
fun2=@(phi) (sin(phi))./sqrt(sin(b)-sin(phi));
qq=integral (fun2,0,phi);
qq;
disp (qq)
end
```

References

- [1] Free Form Fibers, LLC, "Process," Free Form Fibers, LLC, 10 MAY 2018. [Online]. Available: <https://fffibers.com/process/>. [Accessed 10 MAY 2018].
- [2] B. Riccardi, L. Giancarli, A. Hasegawa, Y. Katoh, A. Kohyama, R. H. Jones and L. L. Snead, "Issues and advances in SiCf/SiC composites development for fusion reactors," *Journal of Nuclear Materials*, vol. 329, no. 33, pp. 56-65, 2004.
- [3] L. L. Snead, R. H. Jones, A. Kohyama and P. Fenici, "Status of silicon carbide composites for fusion," *Journal of Nuclear Materials*, vol. 233, pp. 26-36, 1996.
- [4] B. P. Groth, S. M. Langan, R. A. Haber and A. B. Mann, "Relating residual stresses to machining and finishing in silicon carbide," *Ceramics International*, vol. 42, pp. 799-807, 2016.
- [5] I. De Wolf, "Micro-Raman spectroscopy to study local mechanical stress in silicon integrated circuits," *Semicon. Sci. Technol*, vol. 11, pp. 139-154, 1996.
- [6] E. Anastassakis, A. Pinczuk and E. Burstein, "Effect of static uniaxial stress on the Raman spectrum of silicon," *Solid State Communications*, vol. 8, pp. 133-138, 1970.
- [7] Matweb, "Silicon Carbide, Alpha SiC," MatWeb Material Property Data, [Online]. Available: <http://www.matweb.com/search/DataSheet.aspx?MatGUID=dd2598e783ba4457845586b58c8ea9fb&ckck=1>. [Accessed 2018].
- [8] Matweb, "Overview of materials for AISI 5000 Series Steel," MatWeb Material Property Data, [Online]. Available: <http://www.matweb.com/search/DataSheet.aspx?MatGUID=89d4b891eece40fbbe6b71f028b64e9e>. [Accessed 2018].
- [9] L. L. Snead and D. F. Williams, "Assessment of Silicon Carbide Composites for Advanced Salt-Cooled Reactors," Oak Ridge National Laboratory, Oak Ridge, TN, 2007.
- [10] C. R. Jones, C. H. J. Henajer and R. H. Jones, "Crack bridging by SiC fibers during slow crack growth and the resultant fracture toughness of SiC/SiCf composites," *Scripta Metallurgica et Materialia*, vol. 33, no. 12, pp. 2067-2072, 1995.
- [11] L. Longbiao, "Modeling first matrix cracking stress of fiber-reinforced ceramic-matrix composites considering fiber fracture," *Theoretical and Applied Fracture Mechanics*, vol. 92, pp. 24-32, 2017.
- [12] R. Naslain, "Design, preparation and properties of non-oxide CMCs for application in engines and nuclear reactors: an overview," *Composites Science and Technology*, vol. 64, pp. 155-170, 2004.
- [13] C. Richter, K. Mees and M. Willert-Porada, *Si3N4-CMC reinforced with compositionally graded fibers*, International Symposium of Functionally Graded Materials : Multiscale & Multifunctional Structures, 2016.
- [14] Precision Ceramics, "Boron Nitride," Precision Ceramics, 2018. [Online]. Available: <https://precision-ceramics.com/materials/boron-nitride/>. [Accessed

- 2018].
- [15] Precision Ceramics, "Boron Carbide," Precision Ceramics, 2018. [Online]. Available: <https://precision-ceramics.com/materials/boron-carbide/>. [Accessed 2018].
 - [16] Saint-Gobain, "Transparent Armor Sapphire Material Properties," 06 2016. [Online]. Available: <https://www.crystals.saint-gobain.com/products/sapphire-transparent-armor>. [Accessed 2018].
 - [17] Reade, "Titanium Carbide Powder," Reade International Corp., 2018. [Online]. Available: <https://www.reade.com/products/titanium-carbide-powder-tic>. [Accessed 2018].
 - [18] T. Hinoki, E. Lara-Curzio and L. L. Snead, "Mechanical Properties of high purity SiC fiber-reinforced CVI-SiC matrix composites," Metals and Ceramics Division, Oak Ridge National Laboratory, Oak Ridge, TN.
 - [19] L. H. Hovner and G. R. Hopkins, "Ceramic Materials for Fusion," *Nuclear Technology*, vol. 29, no. 3, pp. 274-302, 1976.
 - [20] R. H. Jones, D. Steiner, H. L. Heinisch, G. A. Newsome and H. M. Kerch, "Radiation resistant ceramic matrix composites," *Journal of Nuclear Materials*, vol. 245, no. 2-3, pp. 87-107, 1997.
 - [21] T. M. Besmann, J. C. McLaughlin and H.-T. Lin, "Fabrication of ceramic composites: forced CVI," *Journal of Nuclear Materials*, vol. 219, pp. 31-35, 1995.
 - [22] S. Suyama, T. Kameda and Y. Itoh, "Development of high-strength reaction-sintered silicon carbide," *Diamond and Related Materials*, vol. 12, no. 3-7, pp. 1201-1204, 2003.
 - [23] Y. Katoh, M. Kotani, H. Kishimoto, W. Yang and A. Kohyama, "Properties and radiation effects in high-temperature pyrolyzed PIP-SiC/SiC," *Journal of Nuclear Materials*, vol. 289, no. 1-2, pp. 42-47, 2001.
 - [24] Y. Katoh, K. Ozawa, C. Shih, T. Nozawa, R. J. Shnavski, A. Hasegawa and L. L. Snead, "Continuous SiC fiber, CVI SiC matrix composites for nuclear applications: Properties and irradiation effects," *Journal of Nuclear Materials*, vol. 448, no. 1-3, pp. 448-476, 2014.
 - [25] Y. Katoh, D. F. Wilson and C. W. Forsberg, "Assessment of Silicon Carbide Composites for Advanced Salt-Cooled Reactors," Oak Ridge National Laboratory, Oak Ridge, TN, 2007.
 - [26] World Nuclear Association, "Molten Salt Reactors," JUL 2018. [Online]. Available: <http://www.world-nuclear.org/information-library/current-and-future-generation/molten-salt-reactors.aspx>. [Accessed 2018].
 - [27] M. K. M. Ho, Y. G. H. and G. Braoudakis, "Molten salt reactors," in *Materials and processes for energy: communicating current research and technological developments*, Badajoz, Spain, Formatex, 2013, pp. 761-768.
 - [28] Q. Huang, G. Lei, R. Liu, K. Li, L. C. L. Yan, W. Liu and M. Wang, "Microstructure, hardness, and modulus of carbon-ion-irradiated new SiC fiber (601-4)," *Journal of Nuclear Materials*, vol. 503, pp. 91-97, 2018.
 - [29] A. R. Bunsell and A. Piant, "A review of the development of three generations of

- small diameter silicon carbide fibres," *Journal of Materials Science*, vol. 41, pp. 823-839, 2006.
- [30] A. Hasegawa, S. Nogami, L. L. Snead, R. H. Jones and K. Abe, "Effect of He Pre-implantation and Neutron Irradiation on Mechanical Properties of SiC/SiC Composite," Cyclotron and Radioisotope Center, Tohoku University, Sendai, Japan, 2002.
 - [31] A. B. Mann, M. Balooch, J. H. Kinney and T. P. Weihs, "Radial variations in modulus and hardness in SCS-6 silicon carbide fibers," *Journal of the American Ceramic Society*, vol. 82, no. 1, pp. 111-116, 1999.
 - [32] X. Tang, L. Zhang, H. Tu, H. Gu and L. Chen, "Decarbonization mechanisms of polycarbosilane during pyrolysis in hydrogen for preparation of silicon carbide fibers," *Journal of Materials Science*, vol. 45, pp. 5749-5755, 2010.
 - [33] M. Sato, T. Nakayusa, Y. Inoue, N. Miyamoto and T. Yamamura, "Preparation and properties of ceramic matrix composites with Tyranno fibers(TM) as the reinforcement," Research Institute of Advanced Material Gas-Generator, Tokyo, Japan, 2013.
 - [34] Specialty Materials, Inc, "SCS SiC Fibers - Process, Properties, and Production," 2010. [Online]. Available: specmaterials.com/pdfs/SCSFibersTechnicalPresentation.pdf. [Accessed 2018].
 - [35] J. Pegna, J. L. Scheiter, K. L. Williams and R. Goduguchinta, "HIGH STRENGTH CERAMIC FIBERS AND METHODS OF FABRICATION". United States Patent 20150004393, January 2015.
 - [36] A. Fais, "Why is ductility important in some metals?," 7 1 2016. [Online]. Available: <https://www.quora.com/Why-is-ductility-important-in-some-metals>. [Accessed 12 7 2018].
 - [37] SubSTech Substances and Technologies, "3-point_flexure," 01 06 2012. [Online]. Available: http://www.substech.com/dokuwiki/lib/exe/detail.php?id=flexural_strength_tests_of_ceramics&cache=cache&media=3-point_flexure.png. [Accessed 12 07 2018].
 - [38] SubSTech Substances and Technologies, "4-point_flexure," 01 06 2012. [Online]. Available: http://www.substech.com/dokuwiki/lib/exe/detail.php?id=flexural_strength_tests_of_ceramics&cache=cache&media=4-point_flexure.png. [Accessed 12 07 2018].
 - [39] H. Flugge, Handbook of Engineering Mechanics, McGraw-Hill, 1962.
 - [40] G. R. Clements and L. T. Wilson, "Properties of Materials," in *Manual of Mathematics and Mechanics*, New York and London, McGraw-Hill Book Company, Inc, 1937, p. 257.
 - [41] T. Belendez, C. Neipp and A. Belendez, "Large and small deflections of a cantilever beam," *European Journal of Physics*, vol. 23, no. 3, pp. 371-379, 2002.
 - [42] K. E. Bisshopp and D. C. Drucker, "Large deflection of cantilever beams," *Quarterly of Applied Mathematics*, vol. III, no. 3, pp. 272-275, 1945.
 - [43] A. C. Fischer-Cripps, Nanoindentation, New York: Springer, 2004.
 - [44] N. Barbakadze, S. Enders, S. Gorb and E. Arzt, "Local mechanical properties of

- the head articulation cuticle in the beetle *Pachnoda marginata* (Coleoptera, Scarabaeidae)," *Journal of Experimental Biology*, vol. 209, pp. 722-730, 2006.
- [45] W. C. Oliver and G. M. Pharr, "An improved technique for determining the hardness and elastic modulus using load and displacement sensing indentation experiments," *J. Mater. Res.*, vol. 7, no. 6, 1992.
 - [46] Hysitron Inc., *Hysitron TriboIndenter Users Manual*, Minneapolis, MN: Hysitron, 2001.
 - [47] H. Inc, *TriboIndenter Users Manual*, Minneapolis, MN: Hysitron Inc., 2001.
 - [48] Micro Star Technologies, "Nano Indenter Specifications," Micro Star Technologies, 2016. [Online]. Available: <http://www.microstartech.com/>. [Accessed 15 07 2018].
 - [49] Gamry Instruments, "Raman Spectroscopy," Gamry Instruments, 2018. [Online]. Available: <https://www.gamry.com/application-notes/EIS/raman-spectroscopy/>. [Accessed 15 07 2018].
 - [50] C. Hess, "Raman Spectroscopy: Basic principles and applications," 2006. [Online]. Available: http://www.fhi-berlin.mpg.de/acnew/departement/pages/teaching/pages/teaching__wintersemester__2006_2007/hess_raman_spectroscopy_101106.pdf. [Accessed 15 07 2018].
 - [51] J. Ferraro, K. Nakamoto and C. Brown, *Introductory Raman Spectroscopy: Second Edition*, Elsevier Inc, 2003.
 - [52] E. Waterstreet, Interviewee, *Renishaw maintenance visit*. [Interview]. 16 05 2018.
 - [53] M. S. Brown and C. B. Arnold, "Fundamentals of Laser-Material Interaction and Application to Multiscale Surface Modification," in *Laser Precision Microfabrication*, Berlin, Springer-Verlag, 2010, pp. 91-120.
 - [54] G. Gouadec and P. Colomban, "Raman Spectroscopy of nanomaterials: How spectra relate to the disorder, particle size and mechanical properties," *Progress in Crystal Growth and Characterization of Materials*, vol. 53, pp. 1-56, 2007.
 - [55] P. Colomban, "Analysis of Strain and Stress in Ceramic, Polymer, and Metal Matrix Composites by Raman Spectroscopy," *Advanced Engineering Materials*, vol. 4, no. 8, pp. 535-542, 2002.
 - [56] R. Drago, *Physical Methods in Chemistry*, Saunders, 1977.
 - [57] B. McGinty, "Hydrostatic and Deviatoric Stresses," *Continuum Mechanics*, 2012. [Online]. [Accessed JUL 2018].
 - [58] J. R. Barber, *Intermediate Mechanics of Materials*, New York, NY: McGraw-Hill, 2001.
 - [59] T. Wermelinger and R. Spolenak, "Stress Analysis by Means of Raman Spectroscopy," in *Confocal Raman Microscopy*, Springer, 2018, pp. 259-278.
 - [60] D. Liu, O. Lord and P. E. J. Flewitt, "Calibration of Raman Spectroscopy in the Stress Measurement of Air-Plasma-Sprayed Yttria-Stabilized Zirconia," *Applied Spectroscopy*, vol. 66, no. 10, pp. 1204-1209, 2012.
 - [61] W. Zulehner, "Historical overview of silicon crystal pulling development," *Materials Science and Engineering: B*, vol. 73, no. 1-3, pp. 7-15, 2000.

- [62] C. C. Hu, *Modern Semiconductor Devices for Integrated Circuits*, Pearson, 2010.
- [63] J. J. Wortman and R. A. Evans, "Young's Modulus, Shear Modulus, and Poisson's Ratio in Silicon and Germanium," *Journal of Applied Physics*, vol. 36, no. 153, pp. 153-156, 1965.
- [64] B. Bhushan and X. Li, "Micromechanical and tribological characterization of doped single-crystal silicon and polysilicon films for microelectromechanical systems devices," *Journal of Materials Research*, vol. 12, no. 1, pp. 54-63, 1997.
- [65] AZO Materials, "Silicon," AZO Materials, 2018. [Online]. Available: <https://www.azom.com/properties.aspx?ArticleID=599>. [Accessed 2018].
- [66] S. M. Sze, *Physics of Semiconductor Devices*, John Wiley and Sons, 1969.
- [67] C. Honsberg and S. Bowden, "Optical Properties of Silicon," PV EDUCATION.ORG, [Online]. Available: PVEDUCATION.ORG/pvcdrom/materials/optical-properties-of-silicon. [Accessed 16 1 2017].
- [68] J. P. Russel, "Raman scattering in silicon," *Applied Physics Letters*, vol. 6, no. 11, pp. 223-224, 1965.
- [69] K. Mizoguchi and S. Nakashima, "Determination of crystallographic orientations in silicon films by Raman-microprobe polarization measurements," *Journal of Applied Physics*, vol. 65, no. 7, pp. 2583-2590, 1989.
- [70] Guichelaar, "Acheson Process," in *Carbide, Nitride and Boride Materials Synthesis and Processing*, Chapman and Hall, 1997, pp. 115-129.
- [71] AZO Materials, "CVD SiC Chemical Vapor Deposited Silicon Carbide for Semiconductor Applications," AZO Materials, JUN 2008. [Online]. Available: <https://www.azom.com/article.aspx?ArticleID=4248>. [Accessed 2018].
- [72] Y. M. Tairov and V. F. Tsvetkov, "Investigation of growth processes of ingots of silicon carbide crystals," *Journal of Crystal Growth*, vol. 43, no. 2, pp. 209-212, 1978.
- [73] A. A. Lebedeva, A. S. Tregubova, V. E. Chelnokova, M. P. Scheglov and A. A. Glagovskii, "Growth and investigation of the big area Lely-grown substrates," *Materials Science and Engineering : B*, vol. 46, no. 1-3, pp. 291-295, 1997.
- [74] L. S. Ramsdell, "Studies on silicon carbide," *American Mineralogist*, vol. 32, no. 1-2, 1947.
- [75] O. Kordina, A. Henry and E. Janzen, "Growth and Characterisation of SiC Power Device Material," *Materials Science Forum*, Vols. 264-268, pp. 97-102, 1998.
- [76] J. A. Freitas and W. J. Moore, "Optical Studies of Undoped and Doped Wide Bandgap Carbide and Nitride Semiconductors," *Brazilian Journal of Physics*, vol. 28, no. 1, 1998.
- [77] H. Nienhaus, T. Kampen and W. Monch, "Phonons in 3C-, 4H-, and 6H-SiC," *Surface Science Letters*, vol. 234, pp. 328-332, 1994.
- [78] L. Patrick and W. J. Choyke, "Optical absorption in n-type cubic SiC," *Physical Review*, vol. 186, no. 3, pp. 775-777, 1969.
- [79] M. Polyanskiy, "RefractiveIndex.info," 2008-2016. [Online]. Available: refractiveindex.info/?shelf=main&book=SiC&page=Larruquert. [Accessed 16 1

- 2017].
- [80] L. Gmelin, "Silicium, Part B," in *Gmelins Handbuch der Anorganischen Chemie*, 8th edition, Weinheim, Verlag Chemie, GmbH, 1959.
 - [81] K. Kamitani, M. Grimsditch, J. C. Nipkko and C.-K. Loong, "The elastic constants of silicon carbide: A Brillouin-scattering study of 4H and 6H single crystals," *Journal of Applied Physics*, vol. 82, 1997.
 - [82] G. L. Harris, "Young's Modulus of SiC," in *Properties of Silicon Carbide*, EMIS datareviews series, 1995.
 - [83] Y. C. Cha, G. Kim, H. J. Doerr and R. F. Bunshah, "Effects of activated reactive evaporation process parameters on the microhardness of polycrystalline silicon carbide thin films," *Thin Solid Films*, vol. 253, pp. 212-217, 1994.
 - [84] J. F. Shackelford, Y.-H. Han, S. Kim and S.-H. Kwon, "CRC Materials Science and Engineering Handbook," Taylor and Francis, p. 537.
 - [85] C. D. Nie, S. Bera and J. A. Harrington, "Growth of single crystal YAG fiber optics," *Optical Society of America*, vol. 24, no. 14, pp. 15522-15527, 2016.
 - [86] L. D. Iskhakova, V. V. Kashin, S. V. Lavrishchev, S. Y. Rusanov, V. F. Seregin and V. B. Tsvetkov, "Facet Appearance on the Lateral Face of Sapphire Single-Crystal Fibers during LHPG Growth," *Crystals*, vol. 6, no. 9, 2016.
 - [87] S. Bera, C. D. Nie, M. G. Soskind, Y. Li, J. A. Harrington and E. G. Johnson, "Growth and lasing of single crystal Yag fibers with different Ho³⁺ concentrations," *Optical Materials*, vol. 75, pp. 44-48, 2018.
 - [88] T. A. Parthasarathy, R. S. Hay, G. E. Fair and F. K. Hopkins, "Predicted performance limits of yttrium aluminum garnet fiber lasers," *Optical Engineering*, vol. 49, no. 9, 2010.
 - [89] S. Kostic, Z. Z. Lazarevic, V. Radojevic, A. Miltutinovic, M. Romcevic, N. Z. Romcevic and A. Valcic, "Study of structural and optical properties of YAG and Nd:YAG single crystals," *Materials Research Bulletin*, vol. 63, pp. 80-87, 2014.
 - [90] J. Arvanitidis, K. Papagelix, D. Christofilos, H. Kimura, G. A. Kourouklis and S. Ves, "High pressure Raman study of Y₃Al₅O₁₂," *physica status solidi (b)*, vol. 14, pp. 3146-3154, 2004.
 - [91] P. R. Stoddart, P. E. Ngoepe, P. M. Mjwara, J. D. Comins and G. A. Saunders, "High Temperature Elastic Constants of Yttrium Aluminum Garnet," *Journal of Applied Physics*, vol. 73, no. 11, pp. 7298-7301, 1993.
 - [92] L. Mezeix and D. J. Green, "Comparison of the Mechanical Properties of Single Crystal and Polycrystalline Yttrium Aluminum Garnet," *International Journal of Applied Ceramic Technology*, vol. 3, no. 2, 2006.
 - [93] G. J. Quarles, "State of the Art of Polycrystalline Oxide Laser Gain Materials," in *46th Army Sagamore Materials Research Conference*, St. Michaels, MD, 2005.
 - [94] MatWeb, "Albite (Plagioclase Feldspar NaAlSi₃O₈)," MatWeb Material Property Data, 2018. [Online]. Available: <http://www.matweb.com/search/DataSheet.aspx?MatGUID=282fe5a96f34468ba930f95697947128>. [Accessed 2018].
 - [95] MatWeb, "Anorthite (Plagioclase Feldspar CaAl₂Si₂O₈)," MatWeb Material

- Property Data, 2018. [Online]. Available: <http://www.matweb.com/search/DataSheet.aspx?MatGUID=8cf83a63ffb049adae34b940945bc8e1>. [Accessed 2018].
- [96] MatWeb, "Labradorite (Feldspar; 60% CaAl₂Si₂O₈ + 40% NaAlSi₃O₈)," MatWeb Material Property Data, 2018. [Online]. Available: <http://www.matweb.com/search/DataSheet.aspx?MatGUID=329ce8d5b6e74a0183202a65e81a5fb8>. [Accessed 2018].
- [97] MatWeb, "Orthoclase (Feldspar KAlSi₃O₈)," MatWeb Material Property Data, 2018. [Online]. Available: <http://www.matweb.com/search/DataSheet.aspx?MatGUID=6bf2776a3f37476eb6c848271321185f>. [Accessed 2018].
- [98] E. Winkler, "Appendix A: Evaluation of the Soundness of Stone," in *Stone in Architecture*, Springer-Verlag Berlin Heidelberg, 1997, pp. 283-313.
- [99] Adhikari Granites, "What is Granite?," Adhikari Granites, 2017. [Online]. Available: <http://www.adhikarigranites.com/granites.html>. [Accessed 2018].
- [100] J. M. Brown, R. J. Angel and N. L. Ross, "Elasticity of plagioclase feldspars," *Journal of Geophysical Research: Solid Earth*, vol. 121, pp. 663-675, 2016.
- [101] J. J. Freeman, A. Wang, K. E. Kuebler, B. L. Jolliff and L. A. Haskin, "Characterization of natural feldspars by Raman spectroscopy for future planetary exploration," *The Canadian Mineralogist*, vol. 46, pp. 1477-1500, 2008.
- [102] P. Heyliger, H. Ledbetter and S. Kim, "Elastic constants of natural quartz," *Journal of the Acoustic Society of America*, vol. 114, no. 2, pp. 644-650, 2003.
- [103] Momentive Performance Materials Quartz, Inc., "Fused Quartz Properties and Usage Guide," wa3key, 18 MAY 2007. [Online]. Available: <http://www.quartz.com/gedata.html>. [Accessed 2018].
- [104] Crystran, "Quartz Crystal (SiO₂)," Crystran Ltd., 2012. [Online]. Available: <https://www.crystran.co.uk/optical-materials/quartz-crystal-sio2>. [Accessed 2018].
- [105] K. J. Kingma and R. J. Hemley, "Raman spectroscopic study of microcrystalline silica," *American Mineralogist*, vol. 79, pp. 269-273, 1994.
- [106] D. Henry, "Electron-Sample Interactions," Louisiana State University, 10 NOV 2016. [Online]. [Accessed 2018].
- [107] L. Scipioni, "Principles and applications of helium ion microscopy," 2018. [Online]. Available: <https://microscopy-analysis.com/editorials/editorial-listings/principles-and-applications-helium-ion-microscopy>. [Accessed JUL 2018].
- [108] J. Morgan, J. Notte, R. Hill and B. Ward, "An Introduction to the Helium Ion Microscope," *Microscopy Today*, vol. 14, no. 4, pp. 24-31, 2006.
- [109] V. Sidorkin, "Patterning shrink down to 6nm," Compute Scotland, 10 JUL 2010. [Online]. Available: <https://www.computescotland.com/patterning-shrink-down-to-6nm-3476.php>. [Accessed 2017].
- [110] M. A. Maleque and M. S. Salit, "Mechanical Failure of Materials," in *Materials Selection and Design*, Springer, 2013, pp. 17-38.
- [111] J. B. Wachtman, W. R. Cannon and M. J. Matthewson, *Mechanical Properties of Ceramics*, John Wiley and Sons, Inc., 2009.

- [112] T. Juliano, Y. Gogotsi and V. Domnich, "Effect of indentation conditions on phase transformation induced events in silicon," *Journal of Materials Research*, vol. 18, no. 5, pp. 1192-1201, 2003.
- [113] A. A. Griffith, "The phenomena of rupture and flow in solids," *Philosophical Transactions of the Royal Society*, vol. A221, pp. 163-198, 1920.
- [114] G. D. Quinn, *Fractography of Ceramics and Glasses*, Washington, D.C.: National Institute of Standards and Technology, 2007.
- [115] R. G. Budynas and J. K. Nisbett, *Shigley's Mechanical Engineering Design*, McGraw-Hill, 2010.
- [116] W. Weibull, "A statistical distribution function of wide applicability," *Journal of Applied Mechanics*, vol. 18, pp. 293-297, 1951.
- [117] C. A. Klein, "Characteristic strength, Weibull modulus, and failure probability of fused silica glass," *Optical Engineering*, vol. 48, no. 11, 2009.
- [118] R. Hertzberg, *Deformation and Fracture Mechanics of Engineering Materials*, Wiley, 1995.
- [119] X. Guo, Q. Guo, Z. Li, G. Fan, D.-B. Xiong, Y. Su, J. Zhang, Z. Tan, C. Guo and D. Zhang, "Size and crystallographic orientation effects on the mechanical behavior of 4H-SiC micro-/nano-pillars," *Metallurgical and Materials Transactions A*, vol. 49, no. 2, pp. 439-445, 2018.
- [120] A. Rohatji, "WebPlotDigitizer - Web Based Plot Digitizer," 2010-2017. [Online]. Available: <https://automeris.io/WebPlotDigitizer>.
- [121] H. P. Kirchner, R. M. Gruver and W. A. Sotter, "Fracture Stress-Mirror Size Relations for Polycrystalline Ceramics," *Phil. Mag.*, vol. 33, no. 5, pp. 775-780, 1976.
- [122] H. P. Kirchner, R. M. Gruver and W. A. Sotter, "Use of Fracture Mirrors to Interpret Impact Fracture in Brittle Materials," *Journal of the American Ceramic Society*, vol. 58, no. 5-6, pp. 188-191, 1975.
- [123] J. J. Mecholsky Jr, S. W. Freiman and R. W. Rice, "Fracture Surface Analysis of Ceramics," *Journal of Materials Science*, vol. 11, pp. 1310-1319, 1976.
- [124] I. J. Davies and T. Ishikawa, "Mirror constant for Tyranno Silicon-Titanium-Carbon-Oxygen Fibers Measured in Situ a Three-Dimensional Woven Silicon Carbide/ Silicon Carbide Composite," *Journal of the American Ceramic Society*, vol. 85, no. 3, pp. 691-693, 2002.
- [125] L. C. Sawyer, M. Jamieson, D. Brikowski, M. I. Haider and R. T. Chen, "Strength, Structure, and Fracture Properties of Ceramic fibers produced from Polymeric Precursors: I. Base-Line Studies," *Journal of the American Ceramic Society*, vol. 70, no. 11, pp. 798-810, 1987.
- [126] A. J. Eckel and R. C. Bradt, "Strength Distribution of Reinforcing Fibers in a Nicalon Fiber/ Chemically Vapor Infiltrated Silicon Carbide Matrix Composite," *Journal of the American Ceramic Society*, vol. 72, no. 3, pp. 455-458, 1989.
- [127] G. Gouadec and P. Colomban, "Non-destructive mechanical characterization of SiC fibers by Raman spectroscopy," *Journal of the European Ceramic Society*, vol. 21, pp. 1249-1259, 2000.

- [128] Y. Gou, K. Jian, H. Wang and J. Wang, "Fabrication of nearly stoichiometric polycrystalline SiC fibers with excellent high-temperature stability up to 1900C," *Journal of the American Ceramic Society*, vol. 101, pp. 2050-2059, 2017.
- [129] G. He, B. Zhang, B. Wang, D. Xu, S. Li, Z. Yu and J. Chen, "Amorphous fine-diameter SiC-based fiber from a boron-modified polytitanocarbosilane precursor," *Journal of the European Ceramic Society*, vol. 38, pp. 1079-1086, 2018.
- [130] Y. Inoue, S. Nakashima and A. Mitsuishi, "Raman spectra of amorphous SiC," *Solid State Communications*, vol. 48, no. 12, pp. 1071-1075, 1983.
- [131] A. Kailer, K. G. Nickel and Y. G. Gogotsi, "Raman Microspectroscopy of Nanocrystalline and Amorphous Phases in Hardness Indentations," *Journal of Raman Spectroscopy*, vol. 30, pp. 939-946, 1999.
- [132] M. Havel, D. Baron, L. Mazerolles and P. Colomban, "Phonon confinement in SiC nanocrystals: Comparison of the size determination using transmission electron microscopy and Raman spectroscopy," *Applied Spectroscopy*, vol. 61, no. 8, pp. 855-859, 2007.
- [133] M. Yoshikawa, K. Kosaka, H. Seki and T. Kimoto, "Stress Characterization of 4H-SiC Metal-Oxide-Semiconductor Field-Effect Transistor (MOSFET) using Raman Spectroscopy and Finite Element Method," *Applied Spectroscopy*, vol. 70, no. 7, pp. 1209-1213, 2016.
- [134] S. H. Ward and A. B. Mann, "Four-point bend apparatus for in situ micro-Raman stress measurements," *Measurement Science and Technology*, vol. 29, 2018.
- [135] K. S. Befus, J.-F. Lin, M. Cisneros and S. Fu, "Feldspar Raman shift and application as a magmatic thermobarometer," *American Mineralogist*, vol. 103, pp. 600-609, 2018.
- [136] I. Aliatis, E. Lambruschi, L. Mantovani, D. Bersani, G. D. Gatta, M. Tribaudino and P. P. Lottici, "High-pressure Raman spectroscopy on low albite," *Physics and Chemistry of Minerals*, vol. 44, no. 3, pp. 216-220, 2017.
- [137] D. A. McKeown, "Raman spectroscopy and vibrational analyses of albite: From 25 C through the melting temperature," *American Mineralogist*, vol. 90, no. 10, pp. 1506-1517, 2005.
- [138] R. J. Angel, R. M. Hazen, T. C. McCormick, C. T. Prewitt and J. R. Smyth, "Comparative Compressibility of End-Member Feldspars," *Physics and Chemistry of Minerals*, vol. 15, pp. 313-318, 1988.
- [139] R. J. Angel, L. M. Sochalski-Kolbus and M. Tribaudino, "Tilts and tetrahedra: The origin of anisotropy of feldspars," *American Mineralogist*, vol. 97, no. 5-6., pp. 765-778, 2012.
- [140] R. J. M. M. L. Angel, M. Alvaro and F. Nestola, "A simple GUI for host-inclusion elastic thermobarometry," *American Mineralogist*, vol. 102, pp. 1957-1960, 2017.
- [141] M. J. Kohn, ""Thermoba-Raman-try": Calibration of spectroscopic barometers and thermometers for mineral inclusions," *Earth and Planetary Science Letters*, vol. 388, pp. 187-196, 2014.
- [142] G. M. and R. Powell, "P-V-T relationships and minearl equilibria in inclusions in minerals," *Earth and Planetary Sciences Letters*, vol. 244, no. 3, pp. 683-694,

2006.

- [143] J. F. Asell and M. Nicol, "Raman spectrum of alpha quartz at high pressures," *The Journal of Chemical Physics*, vol. 49, 1968.
- [144] T. Masuda, T. Miyake and M. Enami, "Ultra-high residual compressive stress (>2GPa) in a very small volume (<1mm³) indented quartz," *American Mineralogist*, vol. 96, pp. 283-287, 2011.
- [145] C. Schmidt and M. A. Ziemann, "In-situ Raman spectroscopy of quartz: A pressure sensor for hydrothermal diamond-anvil cell experiments at elevated temperatures," *American Mineralogist*, vol. 85, pp. 1725-1234, 2000.
- [146] University Wafer, "100mm Single Crystal Quartz Wafer," University Wafer, 2018. [Online]. Available: <https://order.universitywafer.com/default.aspx?cat=Single%20Crystal%20Quartz&diam=100mm>. [Accessed 2018].
- [147] Boston Piezo-Optics Inc, "Surface Acoustic Wave Substrates," Boston Piezo Optics Inc., 2018. [Online]. Available: <https://www.bostonpiezooptics.com/saw-substrates>. [Accessed 2018].
- [148] MTI Corporation, "SiO₂ (single crystal quartz)," MTI Corporation, 2013. [Online]. Available: <https://www.mtixtl.com/sio2singlecrystalquartz.aspx>. [Accessed 2018].
- [149] Radio-Electronics, "Quartz Crystal Cuts," Adrio Communications Ltd, 2018. [Online]. Available: <https://radio-electronics.com/info/data/crystals/quartz-crystal-cuts-at-sc-ct.php>. [Accessed 2018].
- [150] J. M. Matthewson and C. R. Kurkjian, "Static Fatigue of Optical Fibers in Bending," *J. Am. Ceram. Soc.*, vol. 70, no. 9, pp. 662-668, 1987.
- [151] M. T. Sebastian, H. Want and H. Jantunen, "Low temperature co-fired ceramics with ultra-low sintering temperature: A review," *Current Opinion in Solid State and Materials Science*, vol. 20, no. 3, pp. 151-170, 2016.
- [152] G. E. Youngblood, C. Lewinsohn, R. H. Jones and A. Kohyama, "Tensile strength and fracture surface characterization of Hi-Nicalon SiC fibers," *Journal of Nuclear Materials*, vol. 289, pp. 1-9, 2001.
- [153] Specialty Materials, Inc, "SCS Silicon Carbide Fiber Technical Presentation," MAY 2018. [Online]. Available: <https://www.specmaterials.com/pdfs/SCSFibersTechnicalPresentation.pdf>. [Accessed 18 MAY 2018].
- [154] C. Hsu, T. C. and W. Fang, "Measuring thin film elastic modulus using a micromachined cantilever bending test by nanoindenter," *Journal of Micro/Nanolithography MEMS MOEMS*, vol. 6, no. 3, pp. 03301-1-7, 2007.
- [155] T. P. Weihs, S. Hong, J. C. Bravman and W. D. Nix, "Mechanical deflection of cantilever microbeams: A new technique for testing the mechanical properties of thin films," *Journal of Materials Research*, vol. 3, no. 5, pp. 931-942, 1988.
- [156] F. Cerdeira, C. J. Buchenauer, F. H. Pollack and M. Cardona, "Stress-Induced Shifts of First-Order Raman Frequencies of Diamond- and Zinc-Blend-Type Semiconductors," *Phys Rev B*, vol. 5, no. 2, 1972.

